



This is to certify that the

dissertation entitled

Photophysics and Photochemistry of Singly Bonded Dirhodium Complexes

presented by

Janice Kadis

has been accepted towards fulfillment of the requirements for

Ph.D. degree in __Chemistry

Date 8 August 1993

MSU is an Affirmative Action/Equal Opportunity Institution

0-12771

LIBRARY Michigan State University

PLACE IN RETURN BOX to remove this checkout from your record. TO AVOID FINES return on or before date due.

DATE DUE	DATE DUE	DATE DUE

MSU is An Affirmative Action/Equal Opportunity Institution

PHOTOPHYSICS AND PHOTOCHEMISTRY OF SINGLY BONDED DIRHODIUM COMPLEXES

By

Janice Kadis

A DISSERTATION

Submitted to
Michigan State University
in partial fulfillment of the requirements
for the degree of

DOCTOR OF PHILOSOPHY

Department of Chemistry

1993

ABSTRACT

PHOTOPHYSICS AND PHOTOCHEMISTRY OF SINGLY BONDED DIRHODIUM COMPLEXES

 $\mathbf{B}\mathbf{v}$

Janice Kadis

The photophysical properties of a structurally characterized homologous series of dirhodium fluorophosphine complexes based on a stable two-electron mixed-valence species have been investigated. The series consists of Rh₂(0,0), Rh₂(0,II)X₂ and Rh₂(II,II)X₄ (X=Cl, Br, I) singly bonded dirhodium cores coordinated bv three bis(difluorophosphino)methylamine ligands. The electronic absorptions of the complexes are identified as arising from $d\sigma \to \sigma^*$, $(X)\sigma \to \sigma^*$ and $\pi^* \to \sigma^*$ σ^* transitions. The excited state properties of the chloride and bromide congeners are discussed with a focus toward the possibility of the two electron photochemical reductive - elimination of halogen from the complexes. Crystalline solids of all of the complexes exhibit long lived luminescence at 77 K. The lifetimes range from 74 to 300 µs and excitation profiles and temperature dependences of the emission bandwidths and lifetimes of each member of the series are characteristic of luminescence

originating from a do* excited state. Temperature dependence studies of the luminescence lifetimes reveal a temperature independent region below ~ 100 K followed by a monotonic increase in the radiative decay rate as the temperature is increased. This temperature dependent behavior is consistent with efficient nonradiative decay observed upon thermal population of an excited state proximate to the lowest energy emissive excited state as seen with LPt^{III}Pt^{III}L tetraphosphates.

The discovery of photochemical reductive elimination of bromine from the Rh₂(0,II)Br₂ complex marks an important step toward the design of a catalytic H—X splitting system for energy storage. Few systems have been developed in which the photoreagent can be regenerated from the thermodynamically stable photoproduct because of the stability of metal – halide bonds. Another system in which this reductive elimination photochemistry is accomplished is [Pt₂(pop)₄X₂]⁴—; comparison of our system with this one begins to elucidate the elements necessary for the systematic reductive - elimination photochemistry. These include a long-lived excited state that contains ligand - to - metal charge transfer character and a solvent dependence which is not yet well understood but could be a factor in stabilizing the radicals formed photochemically.

To my dad, Anthony Kadis

ACKNOWLEDGEMENTS

So many people have played important and essential parts in helping me to realize this goal and each has my deepest gratitude.

First, I'd like to thank Dr. Daniel Nocera for his guidence and encouragement. Through his teaching I learned determination, problem solving, and independence.

Other faculty who have been an integral part of my graduate years include Dr. Donald Ward who solved my crystal structures, Drs. George Leroi and Harry Eick who supervised me in my teaching assignments and helped me to obtain my position at Mississippi University for Women, Drs. Evelyn and James Jackson who provided helpful discussion of my project, NMR training, and great times at the lake. Dr. Kim Dunbar (the Rhodium Goddess) is especially recognized for her support and friendship.

Past and present members of the Nocera group have made our lab a fun and stimulating environment. Included are Joel Dulebohn, Randy King, Yeung Shin Jeonga Yu, I-Jy Chang, Julie Jackson, Claudia Turro, and Jeff Zaleski. I can't forget J.P. Kirby and Mark Torgerson who were always there to help me move. Doug Motry and I shared many wonderful times together. Zoe Pikramenou has become and will always be a special friend. Last, but by no means least, my fellow cockroach Colleen Partigianoni; her special talents are well renowned by all who know her. It wouldn't have been the same without any one of you.

Others who were instrumental in helping me to get here include Mr. Gary VanGenderen, Mr. George Griswold, Dr. Gargi French and Dr. Teresa Birdwhistell. Thanks for the support and encouragement.

Many friends have been there for me through the years and I thank all of them especially though my adopted families Spencer, Alia, and Heather Schubbe, and Euny and Dale Bish.

Also much gratitude goes to my parents Tony and Lucille Kadis.

TABLE OF CONTENTS

			Page
LIST C	FTA	ABLES	ix
LIST C	F FI	GURES	x
CHAP	ΓER	ONE INTRODUCTION	1
A.	Pho	otosystems I and II	1
B.	Sin	gle Electron Transfer	2
C.	Mu	ltielectron Transfer	17
CHAP	ΓER	TWO EXPERIMENTAL	36
A.	Sol	vent Purification	36
	1.	Synthesis	36
	2.	Photochemistry and Spectroscopy	36
В.	Syn	nthesis	37
	1.	General Procedures	37
	2.	Synthesis of Starting Compounds	38
	3.	Synthesis of Dirhodium Fluorophosphine Bromide Complexes	38
		a. $Rh_2[\mu-CH_3N(PF_2)_2]_3[(PF_2)NCH_3(F_2P)]Br_2$ (1)	38
		b. Rh ₂ [CH ₃ N(PF ₂) ₂] ₃ Br ₄ (2)	39
	4.	Synthesis of Dirhodium Fluorophosphine Iodide Complexes	40

			Page
		a. $Rh_2[\mu\text{-}CH_3N(PF_2)_2]_3[(PF_2)NCH_3(F_2P)]I_2$ (3)	40
		b. Rh ₂ [CH ₃ N(PF ₂) ₂] ₃ I ₄ (4)	40
	5.	Synthesis of Rh ₂ [μ -CH ₃ N(PF ₂) ₂] ₃ [(PF ₂)CH ₃ NH) ₂ (5) .	41
C.	Spe	ectroscopic Instrumentation and Methods	41
	1.	Electronic Absorption Spectroscopy	41
	2.	Steady-State Luminescence Spectroscopy	42
	3.	Excitation Spectroscopy	42
	4.	Time Resolved Luminescence Spectroscopy	43
	5.	Nuclear Magnetic Resonance Spectroscopy	43
	6.	Mass Spectrometry	43
	7.	Infrared Spectroscopy	44
D.	Cry	estal Structure Determinations	44
	1.	General Procedures	44
	2.	Methods	45
		a. $Rh_2[\mu\text{-CH}_3N(PF_2)_2]_3[(PF_2)NCH_3(F_2P)]Br_2$ (1)	45
		b. Rh ₂ [CH ₃ N(PF ₂) ₂] ₃ Br ₄ (2)	45
		c. $Rh_2[\mu\text{-}CH_3N(PF_2)_2]_3[(PF_2)NCH_3(F_2P)]I_2$ (3)	46
E.	Pho	tochemistry	47
	ES:	THREE DIRHODIUM FLUOROPHOSPHINE MOLECULAR STRUCTURES AND PHOTOPHYSICAL ES	51
Α.	Intr	oduction	51

			Page
B.	Res	ults and Discussion	58
	1.	Synthesis	58
	2.	Characterization and Structural Interpretation	58
		a. Fast Atom Bombardment Mass Spectrometry	58
		b. X-ray Crystallography	70
	3.	Photophysical Studies	90
		FOUR DIRHODIUM FLUOROPHOSPHINE HALIDES EMISTRY	
A.	Intr	oduction	126
B.	Res	ults and Discussion	128
	1.	Attempted Reduction In the Presence of Excess Phosphine	128
	2.	Attempted Photoreduction In a Coordinating Solvent	130
	3.	Photochemistry in Tetrahydorfuran	131
CHAP	TER I	FIVE CONCLUDING REMARKS	155
REFER	ENC	CES	159

LIST OF TABLES

		Page
1.	Crystallographic Data for Rh ₂ [CH ₃ N(PF ₂) ₂] ₃ [(PF ₂)CH ₃ N(F ₂ P)]Br ₂ (1), Rh ₂ [CH ₃ N(PF ₂) ₂] ₃ Br ₄ (2) and Rh ₂ [CH ₃ N(PF ₂) ₂] ₃ [(PF ₂)CH ₃ N(F ₂ P)]I ₂ (3)	78
2.	Atomic Positional and Isotropic Displacement Parameters (Å ²) for (1)	79
3.	Atomic Positional and Isotropic Displacement Parameters (Å ²) for (2)	81
4.	Atomic Positional and Isotropic Displacement Parameters (Å ²) for (3)	82
5.	Selected Bond Distances (Å) and Bond Angles (deg) for (1)	84
6.	Selected Bond Distances (Å) and Bond Angles (deg) for (2)	86
7.	Selected Bond Distances (Å) and Bond Angles (deg) for (3)	88
8.	Spectral Information of Bimetallic Rhodium Fluorphosphine Compounds	101
9.	Calculated Decay Rate Constants and Energy Gaps of Dirhodium Fluorophosphine Complexes	107
10.	Reaction Conditions and Observed Results for Photolysis of Rh ₂ (0,II)Cl ₂ in the Presence of Excess Phosphine or Phosphite.	129

LIST OF FIGURES

		Page
1.	Schematic diagram of the photosynthetic assembly	4
2.	The sequence of electron transfer steps in the bacterial photosynthetic reaction center, taken from Reference 1. After excitation the electron to BPheo in 4 ps. From there it is transferred to Q_A within 200 ps and on to Q_B in 100 μs	6
3.	Molecular structure of the pentad that mimics the photosynthetic system, taken from Reference 2b	8
4.	Energetics and selected electron transfer pathways of the molecular pentad, taken from Reference 2b	10
5.	Schematic diagram of vectoral disposition of donor / acceptor / secondary acceptor / catalyst within a zeolite channel	13
6.	Diagrammatic representation of energy and electron flow within a modified semiconductor, from Reference 3m	16
7.	Absorption of a photon leading to the formation of either a dissociative or associative biradical excited state	19
8.	Relative energy diagram for Mn ₂ (CO) ₁₀	22
9.	Photoinduced bimolecular reaction of $[Ir(COD)(\mu-pz)]_2$ with 1,2-dichloroethane and with methylene chloride. Pyrazolyl groups are indicated by the bowed lines strapping the metals	24

		Page
10.	Potential energy diagram for a series of photoreagents and photoproducts each having an excited state allowing for the regeneration of the photoreagent from the thermodynamically stable photoproduct	28
11.	Redox chemistry of Co ₂ [CH ₃ N(PF ₂) ₂] ₃ (CO) ₂	30
12.	View of the inner coordination sphere of Rh ₂ (0,0) (a), Rh ₂ (0,II)Cl ₂ (b), and Rh ₂ (II,II)Cl ₄ (c). Phosphorous atoms are from the ligand [CH ₃ N(PF ₂) ₂] which bridges the two	22
	metal centers	33
13.	Experimental apparatus for photolysis	50
14.	Qualitative energy level diagrams for Rh ₂ [CH ₃ N(PF ₂) ₂] ₃ (PF ₃) ₂ , Rh ₂ [CH ₃ N(PF ₂) ₂] ₃ (PF ₃)Cl ₂ , and Rh ₂ [CH ₃ N(PF ₂) ₂] ₃ Cl ₄ generated by mixing of the appropriate C _{3v} and C _{4v} fragments	53
15.	Molecular orbital diagram showing the interaction of Rh ₂ with one halide ligand in the axial coordination sight. The allowed electronic transitions are indicated by the arrows	56 .
16.	Isotope peak intensity pattern for ions containing the indicated number of bromine atoms, taken from Reference 28	60
17.	FAB mass spectrum of Rh ₂ [μ-CH ₃ N(PF ₂) ₂] ₃ [(PF ₂)NCH ₃ (F ₂ P)]Br ₂ in the mass / charge range 600 – 1000 amu.	63
18.	FAB mass spectrum of Rh ₂ [CH ₃ N(PF ₂) ₂] ₃ Br ₄ in the mass / charge range 600 – 1100 amu	65
19.	FAB mass spectrum of Rh ₂ [µ-CH ₃ N(PF ₂) ₂] ₃ [(PF ₂)NCH ₃ (F ₂ P)]I ₂ in the mass / charge range 600 – 1100 amu	67
		~ ·

		Page
20.	FAB mass spectrum of Rh ₂ [CH ₃ N(PF ₂) ₂] ₃ I ₄ in the mass / charge range 700 – 1100 amu. Molecular ion peak is shown in the inset	69
21.	ORTEP drawing and numbering scheme of Rh ₂ [µ–CH ₃ N(PF ₂) ₂] ₃ [(PF ₂)NCH ₃ (F ₂ P)]Br ₂ with 50% probability ellipsoids	73
22.	Ortep view of Rh ₂ [CH ₃ N(PF ₂) ₂] ₃ Br ₄ showing the numbering scheme. Thermal parameters are shown at the 50 % level	75
23.	ORTEP drawing and numbering scheme for Rh ₂ [µ–CH ₃ N(PF ₂) ₂] ₃ [(PF ₂)NCH ₃ (F ₂ P)]I ₂ showing 50% probability ellipsoids	77
24.	Electronic absorption spectrum of Rh ₂ [CH ₃ N(PF ₂) ₂] ₃ (PF ₃) ₂ taken in CH ₂ Cl ₂ at room temperature	92
25.	Electronic absorption spectra of Rh ₂ [CH ₃ N(PF ₂) ₂] ₃ Cl ₄ (—) and Rh ₂ [CH ₃ N(PF ₂) ₂] ₃ Br ₄ () dissolved in CH ₂ Cl ₂ at room temperature	94
26.	Electronic absorption spectra of Rh ₂ [CH ₃ N(PF ₂) ₂] ₃ (PF ₃)Cl ₂ (—) and Rh ₂ [μ-CH ₃ N(PF ₂) ₂] ₃ [(PF ₂)NCH ₃ (F ₂ P)]Br ₂ () dissolved in CH ₂ Cl ₂ at room temperature.	96
27.	Electronic absorption spectrum of Rh ₂ [CH ₃ N(PF ₂) ₂] ₃ I ₄ dissolved in CH ₂ Cl ₂ at room temperature.	99
28.	Emission spectra of Rh ₂ [CH ₃ N(PF ₂) ₂] ₃ (PF ₃) ₂ (a), Rh ₂ [CH ₃ N(PF ₂) ₂] ₃ Cl ₂ () and Rh ₂ [μ -CH ₃ N(PF ₂) ₂] ₃ Cl ₄ () and Rh ₂ [CH ₃ N(PF ₂) ₂] ₃ Cl ₄ () and Rh ₂ [CH ₃ N(PF ₂) ₂] ₃ Br ₄ () (c). All obtained at 77 K as the solids	104

		Page
29.	Unpolarized excitation spectrum of crystalline Rh ₂ [CH ₃ N(PF ₂) ₂] ₃ (PF ₃)Cl ₂ at 77 K	106
30.	Plot of the temperature dependence of the observed emission decay constant for a solid sample of Rh ₂ [CH ₃ N(PF ₂) ₂] ₃ (PF ₃) ₂ The solid line is the fit of the data to Equation 1	110
31.	Plot of the temperature dependence of the observed emission decay constant from solid samples of Rh ₂ [CH ₃ N(PF ₂) ₂] ₃ (PF ₃)Cl ₂ (a) and Rh ₂ [\mu-CH ₃ N(PF ₂) ₂] ₃ [(PF ₂)NCH ₃ (F ₂ P)]Br ₂ (b). The solid line is the fit of the data to Equation 1	112
32.	Plot of the temperature dependence of the observed emission decay constant from solid samples of Rh ₂ [CH ₃ N(PF ₂) ₂] ₃ Cl ₄ (a) and Rh ₂ [CH ₃ N(PF ₂) ₂] ₃ Br ₄ (b). The solid line is the fit of the data to Equation 1	114
33.	Potential energy diagram showing a singlet excited state in close proximity to a triplet excited state. ΔE is the energy gap between the two states. Radiative decay is represented by zigzag arrow; non-radiative decay by dotted line	116
34.	Proposed energy diagrams of the lowest energy excited states of Pt ₂ (III,III) tetraphosphates and dirhodium fluorophosphine compounds. State manifolds are derived from the spin-orbit coupling perturbations of the $^{1,3}E_u$ states arising from one electron ($d\pi^* \rightarrow d\sigma^*$) promotions. The point groups D ₃ , C _s , and C ₂ correspond to the complexes Rh ₂ (0,0), Rh ₂ (0,II)X ₂ and Rh ₂ (II,II)X ₄ respectively	119
35.	Potential surface illustrating coupling between vibrational levels of the excited state and ground state. Radiative decay is shown by zig-zag line; non-radiative by dotted line	122
36.	Potential surface showing radiative and nonradiative deactivation pathways from an excited state which is strongly coupled to a second twisted excited state. Radiative transitions are depicted by zig-zag lines; non-radiative by dotted lines	124

		Page
37.	Electronic absorption spectral changes during photolysis ($\lambda > 375$ nm) of a THF solution of Rh ₂ (0,II)Cl ₂ containing 2,3-dimethyl-1,3-butadiene at -10 °C. Total irradiation time was 195 min	133
38.	Electronic absorption spectral changes during photolysis ($\lambda > 305$ nm) of a THF solution of Rh ₂ (0,II)Br ₂ containing 2,3-dimethyl-1,3-butadiene at -10 °C. Total irradiation time was 115 min	136
39.	FAB mass spectrum of the photoproducts isolated from photolysis ($\lambda > 305$ nm) of Rh ₂ (0,II)Br ₂ in a THF solution containing 2,3-dimethyl-1,3-butadiene at -10 °C. Assignments of the peaks in the spectrum correspond to: (a) Rh ₂ [CH ₃ N(PF ₂) ₂] ₃ [(F ₂ P)CH ₃ NH] ₂ , (b) Rh ₂ [CH ₃ N(PF ₂) ₂] ₃ [(F ₂ P)CH ₃ NH](PF ₂ H), (c) unknown	139
40.	FAB mass spectrum of the compound Rh ₂ [CH ₃ N(PF ₂) ₂] ₃ [(F ₂ P)CH ₃ NH] ₂ in the [M/Z] range 650 – 950 amu	141
41.	Electronic absorption spectral changes during irradiation (λ > 305 nm) of a THF solution of Rh ₂ (0,II)Br ₂ containing 2,3-dimethyl-1,3-butadiene and CH ₃ N(PF ₂) ₂ in excess at -10 °C. Total irradiation time was 60 min	143
42.	Electronic absorption spectrum of Rh ₂ [CH ₃ N(PF ₂) ₂] ₃ [(F ₂ P)CH ₃ NH] ₂ , dissolved in CH ₂ Cl ₂ at room temperature	146
43.	FAB mass spectrum of the photoproducts isolated from photolysis ($\lambda > 305$ nm) of Rh ₂ (0,II)Br ₂ in a THF solution containing 2,3-dimethyl-1,3-butadiene and CH ₃ N(PF ₂) ₂ in excess at -10 °C. Peak at [M / Z] 976 amu corresponds to Rh ₂ [CH ₃ N(PF ₂) ₂] ₄ [(F ₂ P)CH ₃ NH)]. Other observable masses correspond to fragmentation peaks from (a) Rh ₂ [CH ₃ N(PF ₂) ₂] ₃ [(PF ₂)CH ₃ NH] ₂ , (b) Rh ₂ (0,II)Br ₂ , and (c) unknown	148

			Page
4	44.	Summary of the photoproducts formed by the photolysis of Rh ₂ (0,II)Br ₂ which have been identified by FAB mass spectroscopy and absorption spectroscopy	150
2	45.	Possible reaction pathway followed by Rh ₂ (0,II)Br ₂ upon excitation. Heterolytic cleavage of two Br· radicals followed by stabilization of the open coordination site by a difluorophosphine axially coordinated to another molecule. Cleavage of the coordinating ligand into fragments which are stabilized by H· from the solvent THF	153
4	46.	Possible four electron chemistry which could be accomplished with a series of multi-electron photoreagents	158

Chapter One

Introduction

A. Photosystems I and II

Most designs of efficient systems for charge separation and energy storage and conversion usually attempt to mimic the elegant function of the photosynthetic system. In this natural process, shown schematically in Figure 1, the light harvesting complex transfers energy to Photosystem (PS) II exciting the special pair. An electron from the excited special pair is shuttled away from PS II through a series of energetically downhill steps. The system consists of two types of quinones, cytochrome f, iron-sulfur proteins, and a plastocyanine interacting in a manner to separate the electron from the hole in distance and energy. Upon reaching PS I, the electron from PS II fills the incipient hole created by excitation of PS I. The excited electron from PS I is transferred through a series of acceptors, iron-sulfur proteins, ferridoxin, and ferridoxin NADP+ reductase, where NADP+ is reduced to NADPH. The strongly oxidizing equivalents created at PS II can oxidize water to O₂ through the cooperativity of the Oxygen Evolving Complex, a cluster of four manganese atoms which can accumulate and store four charge units before actual water oxidation occurs.

The efficiency of Photosystems I and II is due to the fast electron transfer and separation of the electrons and holes minimizing back electron transfer. Figure 2 pictorially represents the time frame in which this electron transfer occurs. In step (a), absorption of a photon yields the excited special pair; step (b) shows electron transfer to the BPheo a occurring within 4 ps; in (c), the electron is transferred to Q_A in 200 ps; and step (d) transfers the electron to Q_B within 100 µs. The intricacies of the system make design of structures that can carry out multielectron transfers difficult. However, attempts are being made to synthesize and study systems capable of fast electron transfer,² directionalization of redox equivalents³ and storage of multiple charges.⁴

B. Single Electron Transfer

Systems capable of fast electron transfer include macrocycles of Wasieliewski, $^{2(a)}$ McLendon $^{2(a)}$ and the triads, tetrads, and pentad of Gust and Moore, $^{2(b)}$ shown in Figure 3. The pentad is structurally the most sophisticated, featuring a cartenoid electron donor covalently linked to zinc metallated porphyrin, which in turn is linked to a free base porphyrin bearing a diquinone (napthoquinone and benzoquinone) species. This system mimics several aspects of photosynthesis. In addition to yielding a long lived charge separated state ($\tau = 55 \mu s$) with a quantum yield of approximately 0.83, it does so using the multistep series of electron transfers shown in Figure 4. Initial excitation of the free-base porphyrin leads to a charge separated state C— P_{Zn} — P^+ — Q_A — Q_B . Two secondary electron transfer reactions (steps 1 and 2), one involving electron transfer from the napthoquinone to the benzoquinone to yield C— P_{Zn} — P^+ — Q_A — Q_B^- ; the other forming

Figure 1. Schematic diagram of the photosynthetic assembly.

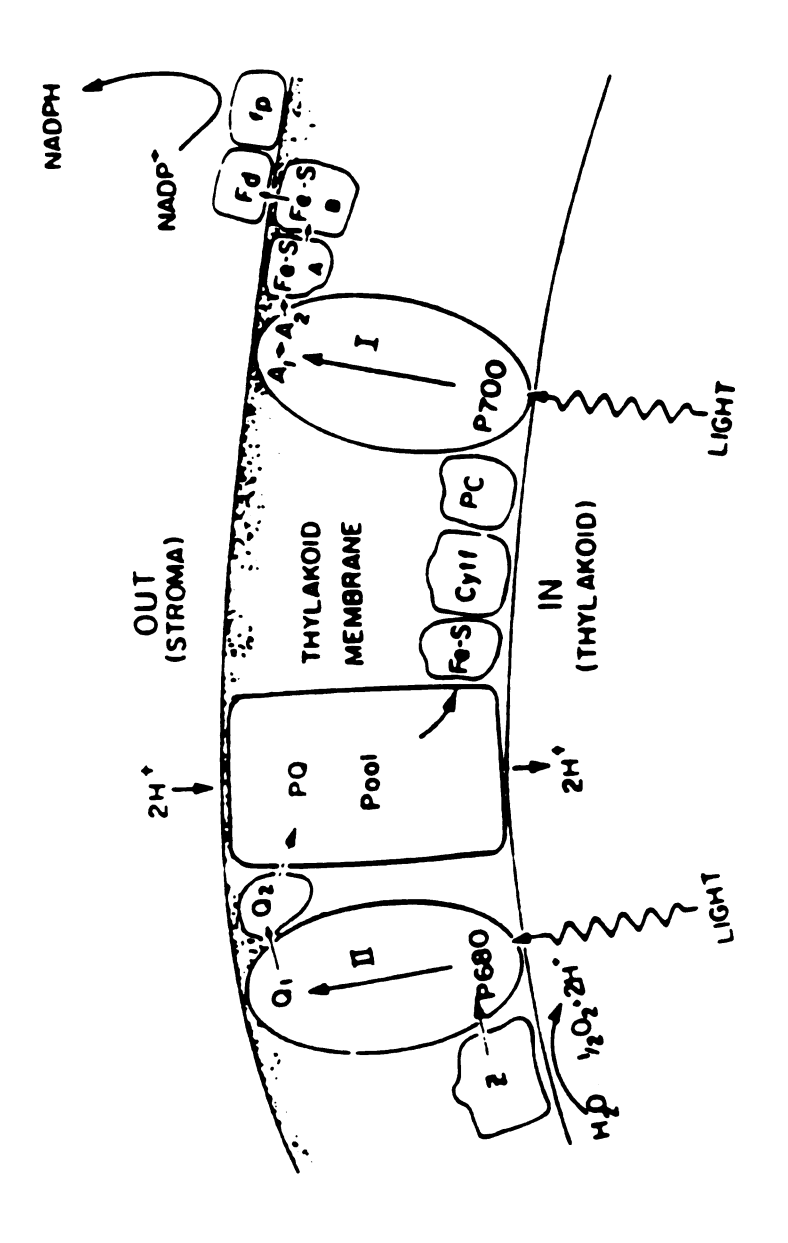


Figure 1

Figure 2. The sequence of electron transfer steps in the bacterial photosynthetic reaction center, taken from Reference 1. After excitation the electron is transferred to BPheo in 4 ps. From there it is transferred to Q_A within 200 ps and on to Q_B in 100 μs .

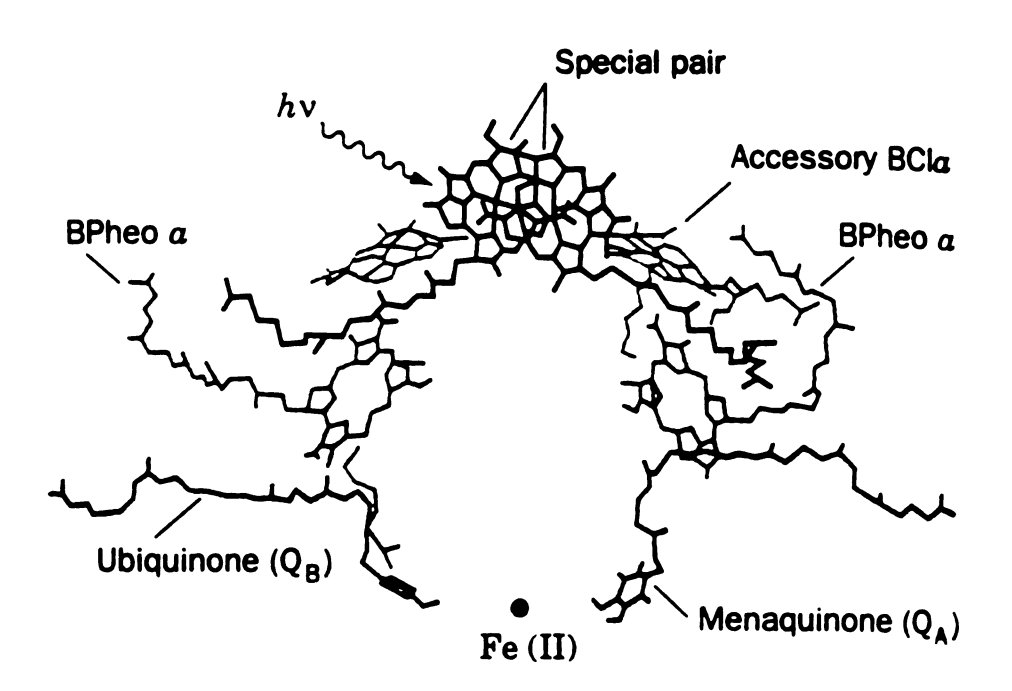
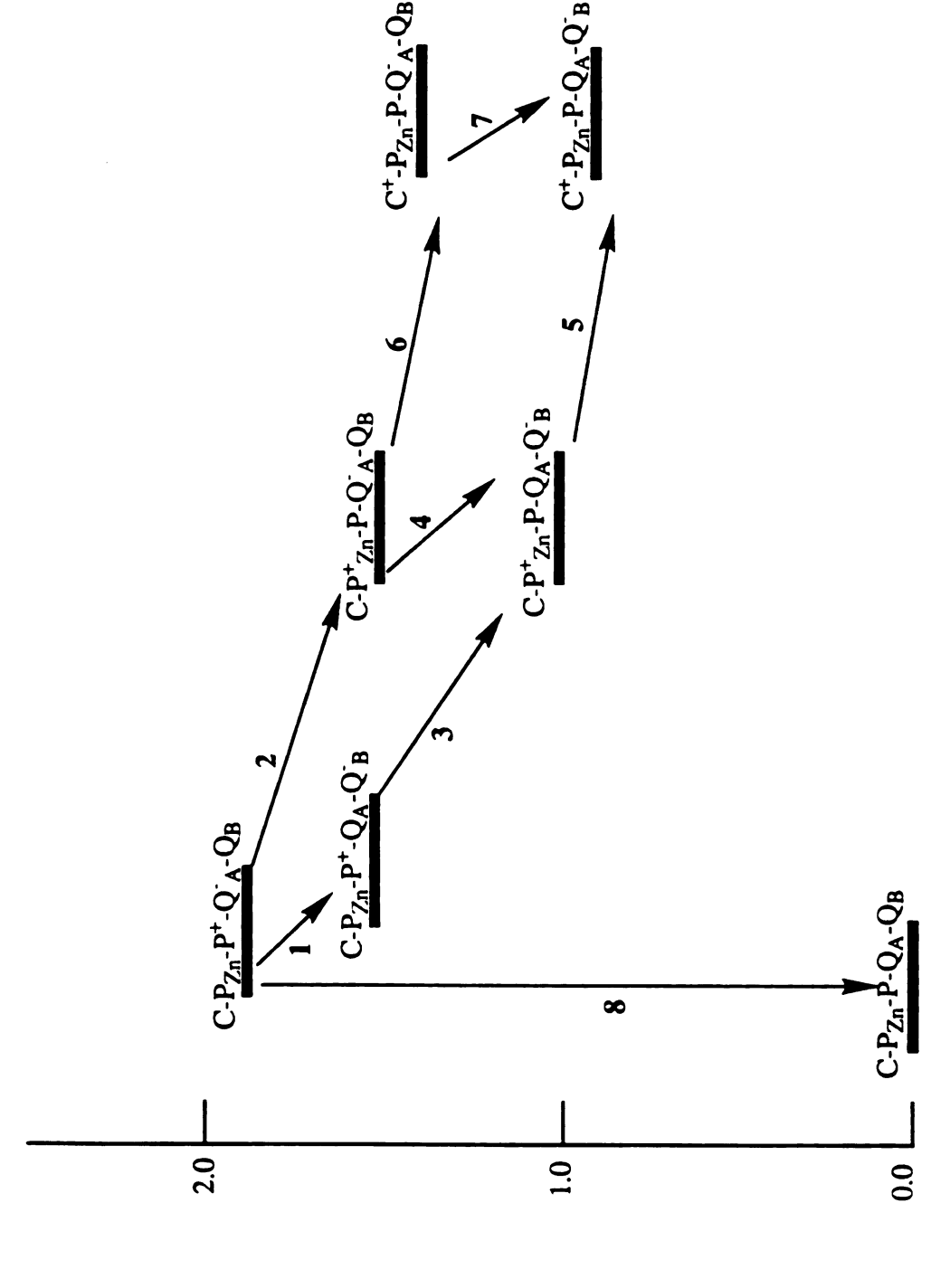


Figure 2

Figure 3. Molecular structure of the pentad that mimics the photosynthetic system, taken from Reference 2b.

Figure 3

Figure 4. Energetics and selected electron transfer pathways of the molecular pentad, taken from Reference 2b.



Energy (eV)

C— P_{Zn}^+ — Q_A^- — Q_B , compete with charge recombination to the ground state. Electron transfer steps 3 and 4 followed by step 5 or 7 yield C— P_{Zn}^+ — P_{QA}^- — Q_B^- which will directly decay to C+— P_{Zn}^- — P_{QA}^- — Q_B^- Alternatively, the complex C— P_{Zn}^+ — P_{QA}^- — Q_B^- can decay to yield C+— P_{Zn}^- — P_{QA}^- — Q_B^- ultimately yielding the charge separated C+— P_{Zn}^- — P_{QA}^- — Q_B^- .

Other efforts to achieve directional charge separation rely on the construction of organized assemblies. Mallouk et al. have developed a vectoral disposition of donor/acceptor/secondary acceptor/catalyst within the cavity of a zeolite L or Y as depicted in Figure 5.3(a,b,i) The stepwise construction of the triad is performed by implantation of platinum aggregates into the zeolite. The secondary acceptor, benzylviologen (BV2+) is then intercalated into the cavity, and the covalently linked sensitizer-acceptor, tris(bipyridine)ruthenium(II)-N,N'-dialkyl-2,2'-bipyridinium (RuL₃²⁺nDQ²⁺) is ion exchanged onto the surface of the zeolite. The RuL₃²⁺-nDQ²⁺ is oriented on the zeolite surface in such a way that the nDQ2+ end enters the open end of the structure. Evidence for this is given by the lifetime of the charge separated complex (Ru³⁺-nDQ⁺) which is significantly longer for the immobilized complex versus the complex in solution (0.44 µs vs. < 5 ns). This is explained by the the inhibited motion about the flexible ethylene bridge which should slow both forward and back electron transfer. The operation of this system begins with the harvesting of photons at the sensitizer. Upon irradiation, the charge separated state (Ru³⁺-BV⁺) is formed in less than 100 ns and persists for 37 µs. Electrons donated by the sensitizer are transferred through the primary and secondary acceptor to the platinum catalyst where reduction of protons from water or acid can be

Figure 5. Schematic diagram of vectorial disposition of donor / acceptor / secondary acceptor / catalyst within a zeolite channel.

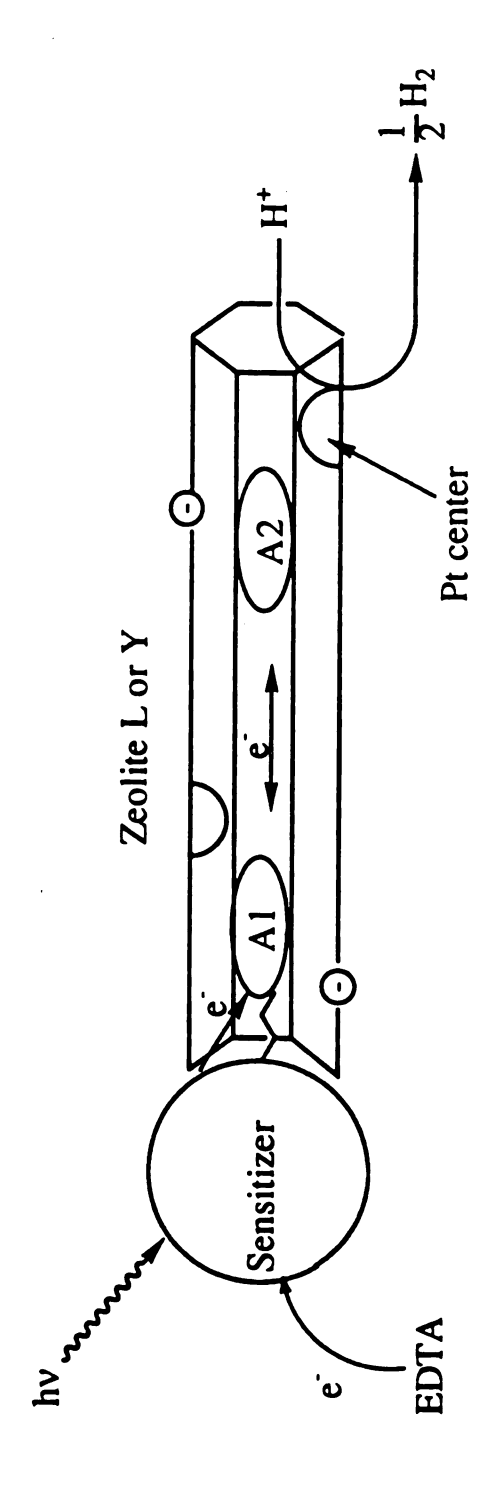


Figure 5

accomplished. The photooxidized sensitizer is regenerated by a sacrificial electron donor such as EDTA, to complete the oxidation / reduction cycle. In systems similar to this, the reported efficiency for hydrogen production is $< 3\times10^{-5}$, attesting to the fact that the efficiency of this system is still far removed from the successful function of natural photosynthetic systems.

A more efficient system is that of Grätzel ³⁽ⁱ⁾ shown in Figure 6. The function is derived from the photovoltaic response of a high surface area TiO₂ semiconductor film deposited on a conducting glass sheet and coated with a monolayer of a charge transfer dye of two ruthenium bis(bipyridyl) units which serve as light gathering antennae funneling excitation to a ruthenium bis(dicarboxybipyridyl) sensitizer from which electrons are transferred to the semiconductor. Electrons and holes can separately migrate to the semiconductor surface where water reduction and oxidation can occur in the presence of a suitable catalyst. The higher efficiency of this system over earlier semiconductor based photocells is derived from the higher proportion of incident solar energy gathered (46% vs 1% for the earlier semiconductor systems).

The systems described thus far are based on directional electron transfer to prevent charge recombination and to make use of the photogenerated redox equivalents. Another common approach is to use a photoreductant or photoxidant in the presence of a sacrificial electron donor or acceptor, respectively. ⁵ One of the most recent of this type of system is by Frank et. al.⁶ who describe the use of the double salt complex [Pt(bpy)₂|₂[Pt(pop)₄] nH₂O ("PBPop"; bpy = 2,2' bipyridine and pop = [H₂P₂O₅]²-) as a photosensitizer for generating H₂ from aqueous solutions containing EDTA as an electron donor and a colloidal platinum catalyst. The complex exhibits two forms. An orange form has approximately four waters

Figure 6. Diagrammatic representation of energy and electron flow within a modified semiconductor, from Reference 3m.

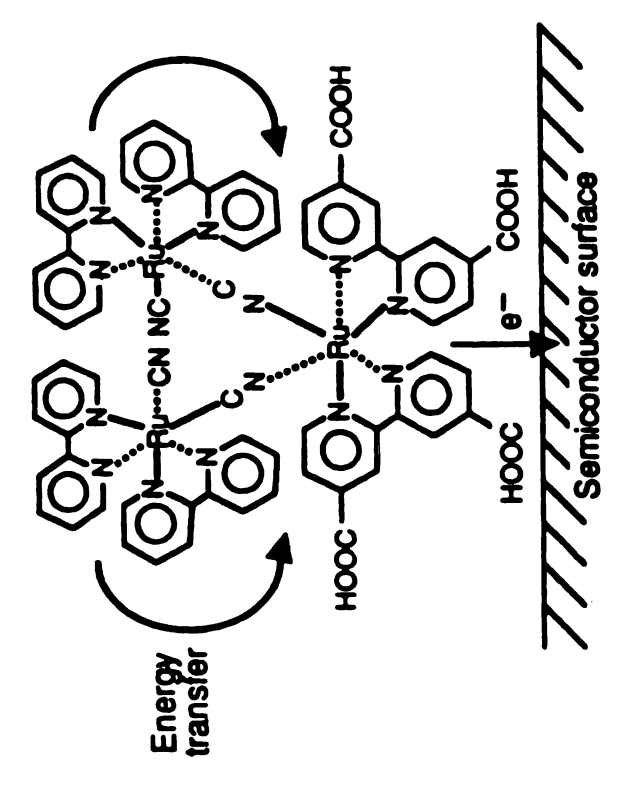


Figure 6

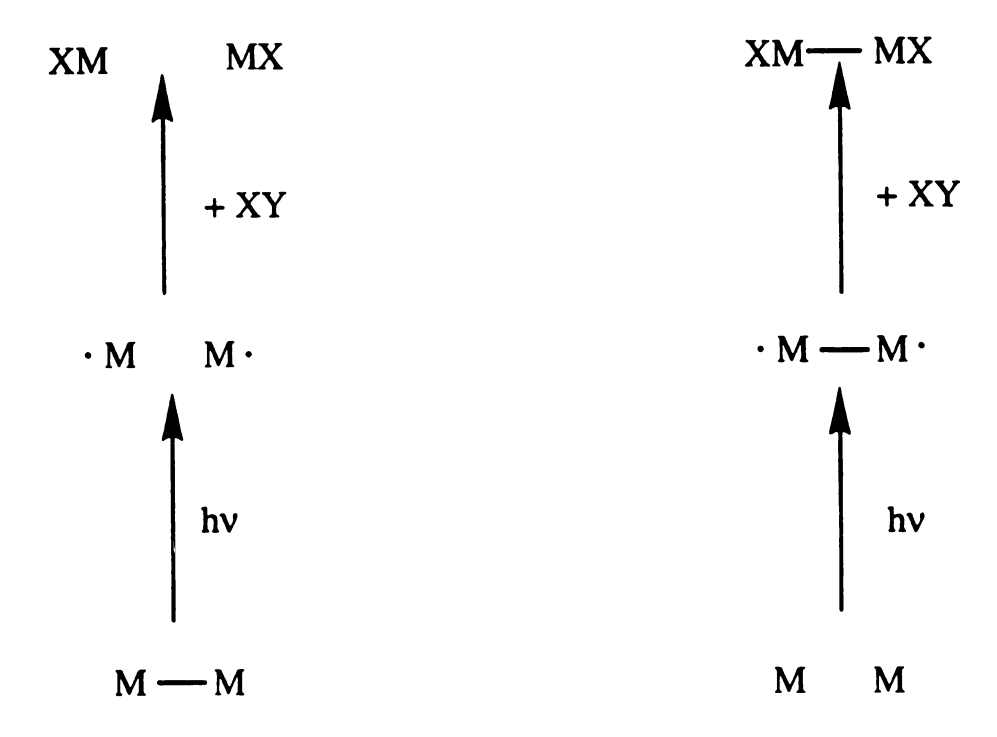
of hydration and a yellow form is hydrated by approximately two waters. Powder suspensions of both forms of PBPop are active photosensitizers, with the yellow form being considerably more active. The maximum rate of hydrogen production with the yellow PBPop photosystem is 77.6 μ L/h at an excitation wavelength of 488 nm yielding a 215 μ L of H₂ after 175 minutes of irradiation. Photocatalytic activity of PBPop can be sustained for a period of at least 51 hours during which time 4.72 mL of H₂ is produced. An eventual attenuation in the rate of H₂ production is attributed to consumption of EDTA, the sacrificial electron donor and a buildup of it's decomposition products. While this system is superior to the inorganic semiconductor or zeolite systems in terms of simplicity and ease of synthesis, it requires the use of a sacrificial electron donor to effect charge transfer.

C. Multielectron Transfer

The problems of charge separation and the need for a catalyst might be circumvented by a molecular system with a long-lived excited state capable of affecting multielectron transformations. Most research to date has been in the direction of coupling the redox activity of metal centers in a bimetallic core. The photochemistry of bimetallic complexes can be generally grouped into reactions proceeding from either a dissociative or an associative excited state depending upon whether the primary photoprocess leads to fragmentation of the complex. The processes are shown in Figure 7.

Dissociative excited states can arise from the photolysis of either d^7 — d^7 or d^9 — d^9 singly bonded metal complexes as exemplified by $Mn_2(CO)_{10}$ and $Cr_2(CO)_8$, respectively. Irradiation of the lowest energy transition

Figure 7. Absorption of a photon leading to the formation of either a dissociative or associative biradical excited state.



Dissociative Mechanism

Associative Mechanism

Figure 7

promotes an electron from a d σ bonding level into a σ^* antibonding orbital, leaving a net bond order of zero between the metals, and consequently cleavage of the metal-metal bond is observed. Figure 8 shows the molecular orbital diagram of $Mn_2(CO)_{10}$ and the electronic transition leading to photofragmentation of the complex into 2 [·Mn(CO)₅] radical fragments. Wrighton showed that the radical could be trapped in degassed CCl₄ to give $Mn(CO)_5Cl.^7$ He followed the reactions by UV-Vis or IR spectroscopy, and determined the stoichiometries and quantum efficiencies to be consistent with metal-metal bond cleavage. The noteworthy result of these experiments is that electronic excitation produces a [·Mn(CO)₅] radical species from which sequential one electron chemistry is observed to effect an overall two electron process.

Photofragmentation can be circumvented by strapping the two metal atoms together with the coordination of bidentate ligands across the metalmetal bond. This is dramatically illustrated by the comparison of the photochemistry of $Re_2(CO)_8L_2$ (L=CO, $P(C_6H_5)_3$) and $Re_2(CO)_8(PP)$ (PP = bis(diphenylphosphino)methane, bis(dimethylphosphino)methane).8 The $Re(CO)_8L_2$ dimers undergo rapid and efficient metal-metal bond cleavage to form [·Re(CO)_4L] radicals. Coordinating a PP bidentate ligand across the metal-metal bond prevents photodegradation of the dimer as evidenced by the observation of emission from the σ^* excited state at low temperatures. Another example showing the effect of bidentate ligands is found in $[Ir(COD)(\mu-pz)]_2$ (COD = 1,5-cyclooctadiene and pz = pyrazolyl).9 The electronically excited [Ir(COD)(μ -pz)]_2 reacts with alkyl halides as shown in Figure 9. The first step is halide abstraction by the electronically excited compound to yield the mixed-valence intermediate species and the alkyl radical. When the alkyl halide is dichloromethane, the alkyl radical

Figure 8. Relative energy diagram for $Mn_2(CO)_{10}$.

$$Mn_2(CO)_{10} \xrightarrow{h\nu} 2(CO)_5Mn$$

$$x^2-y^2 \xrightarrow{} x^2-y^2$$

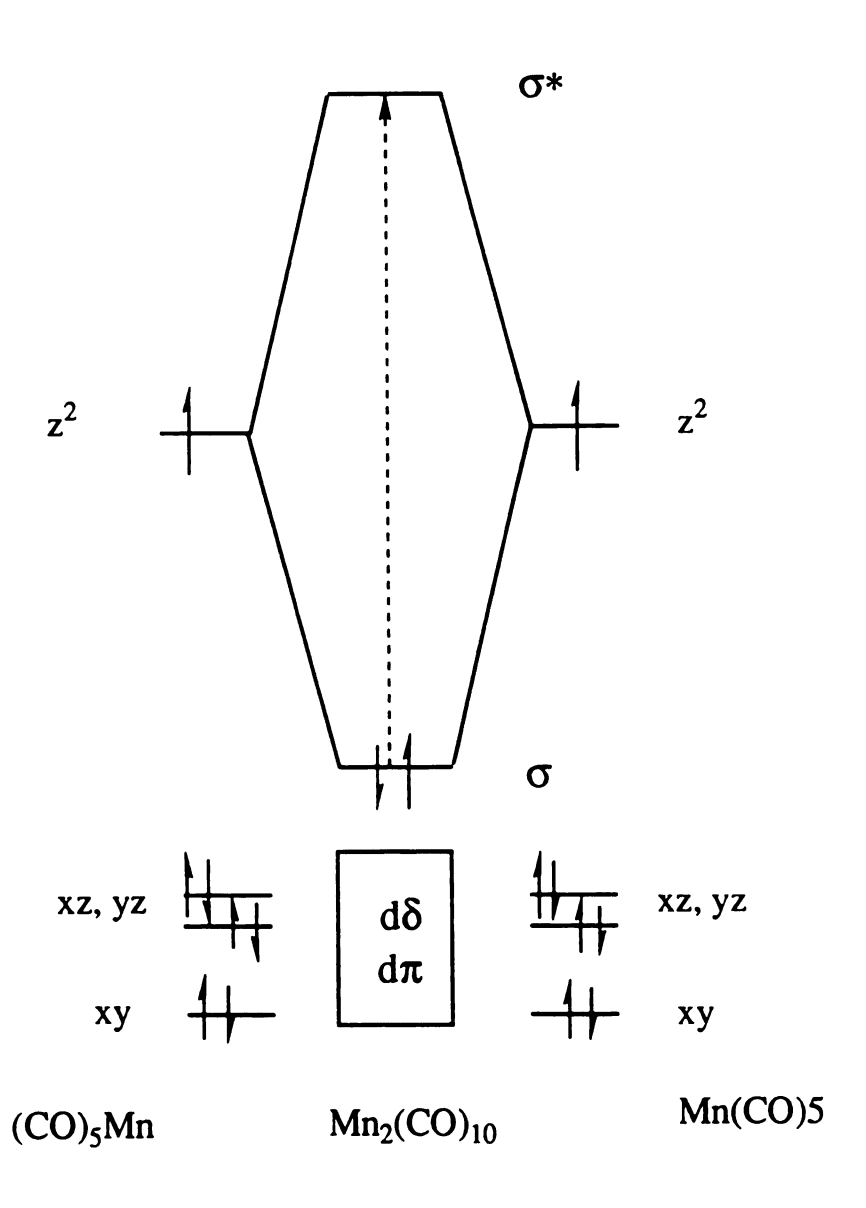


Figure 8

Figure 9. Photoinduced bimolecular reaction of $[Ir(COD)(\mu-pz)]_2$ with 1,2-dichloroethane and with methylene chloride. Pyrazolyl groups are indicated by the bowed lines strapping the metals.

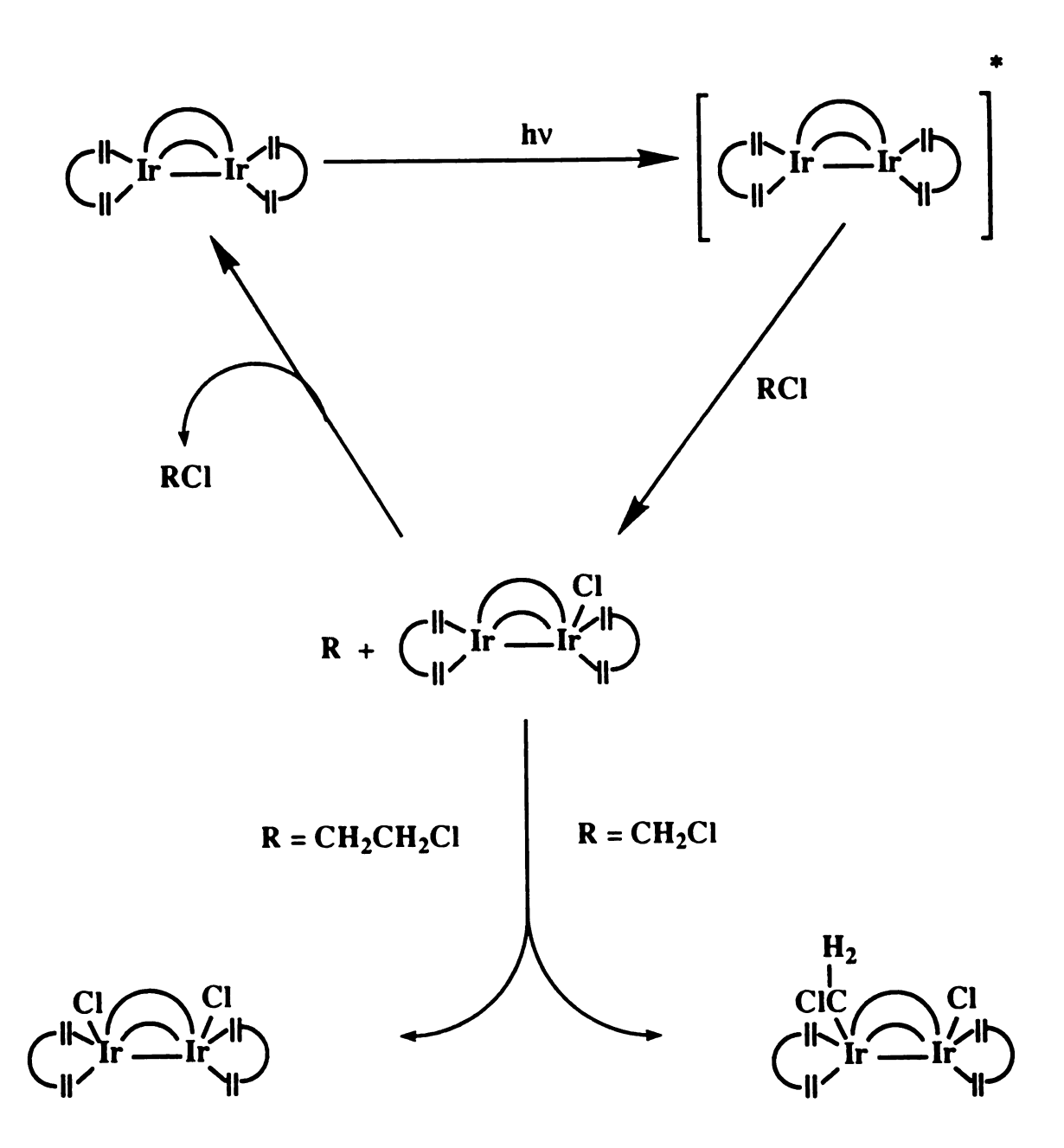


Figure 9

oxidatively adds to the mixed valence compound yielding the two electron oxidative addition product $[Ir(COD)(\mu-pz)]_2(ClCH_2)(Cl)$. When the alkyl halide is 1,2 dichloroethane, the mixed valence intermediate abstracts a second halide from the alkyl radical producing ethene and $[Ir(COD)(\mu-pz)Cl]_2$. In this manner the coupling of the one electron steps to effect an overall two-electron process can occur at one metal center.

Another method used to accomplish two-electron transformations at a single metal center is through the use of complexes which form associative excited state.

Associative excited states are exemplified by the $d^8 ext{...} d^8$ metal complexes $[Pt_2(pop)_4]^{4-}$ and $[Rh_2(bridge)_4]^{2+}$ $[pop = (P_2O_5H_2)$ bridge = 1,3-diisocyanopropane]. Molecular orbital calculations have determined the ground state configuration as $(\sigma)^2(\sigma^*)^2$ with the excited state configuration being $(\sigma)^2(\sigma^*)^1(p\sigma)^1$. For these compounds the lowest energy transition promotes an electron from an antibonding orbital to one that is metal-metal bonding resulting in an increased metal-metal interaction in the excited state, hence the designation associative. The rich photooxidation chemistry of these complexes is well documented. Reactions include the 550 nm irradiation of $[Rh_2(bridge)_4]^{4+}$ in 12 M HCl to produce H₂ and $[Rh_2(bridge)_4Cl_2]^{2+10}$. In the first step, $[Rh_2(bridge)_4]^{4+}$ reacts thermally with HCl to produce H₂ and the mixed - valence tetranuclear complex $[Rh_4(bridge)_8Cl_2]^{6+}$, which reacts photochemically with HCl to produce the final photoproduct $[Rh_2(bridge)_4Cl_2]^{4+}$ and another half mole of H₂.

This chemistry, even though successful, results in the formation of metal-halide bonds. The problem lies in the thermodynamic stability of such bonds. Comparison of metal-halide bond dissociation energies with that of metal carbonyls shows impressively ΔH Mn—Cl = 54 kcal / mol while ΔH

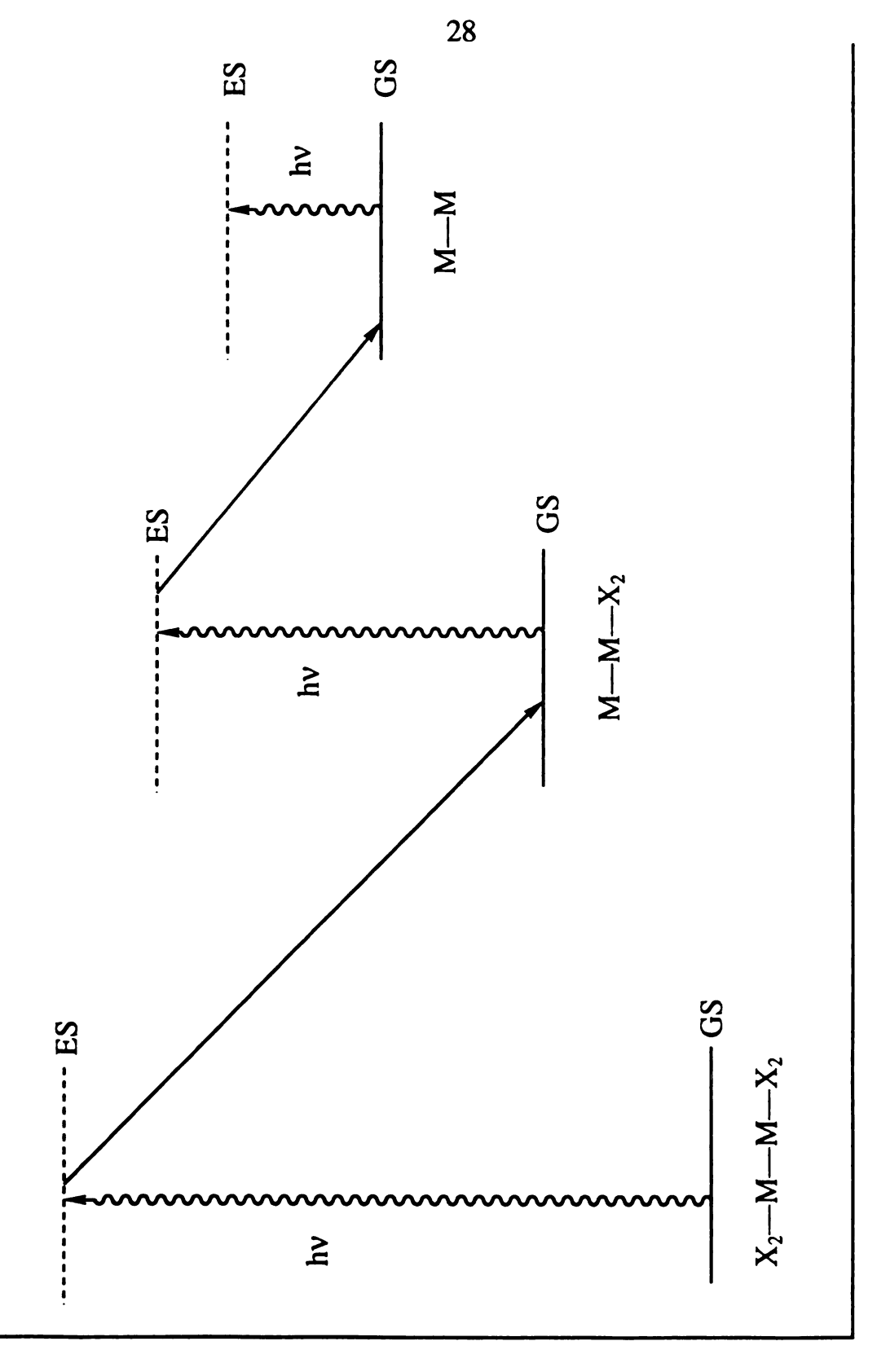
Mn—CO = $< 7 \text{ kcal / mol.}^{11}$ Because of this few systems have been developed in which the photoreagent can be regenerated from the photoproduct. One system in which photoregeneration of the reagent from photoproduct is realized is $[Pt_2(pop)_4]^{4-}$. This complex reacts photooxidatively with halides to yield $[Pt_2(pop)_4X_2]^{4-}$. The oxidized photoproduct can then undergo photoreduction to regenerate the initial reagent $[Pt_2(pop)_4]^{4-}$ via a long lived excited state.

This provided the motivation for our group to focus on the design of a series of bimetallic complexes, with each member of the series differing in oxidation state by two and each possessing a long lived excited state. A series of multi-electron photoreagents designed in such a way as depicted in Figure 10, would possibly allow for photoconversion of the thermodynamically stable tetrachloride complex back to the initial photoreagent.

Our synthetic strategy for developing mixed-valence complexes to engender multielectron reactivity relied on employing a ligand capable of stabilizing metal centers through a wide range of oxidation states and geometry changes (because multi-electron transformations are usually accompanied by significant changes in structure). An obvious choice on this basis was the bis(difluorophosphino)methylamine ligand. Studies by King ¹³ showed this ligand's capacity to stabilize a metal core to an overall six electron change in formal oxidation state. The chemistry is summarized in Figure 11. The dicobalt complex, Co₂[CH₃N(PF₂)₂]₃(CO)₂ with three bridging fluorophosphine ligands and two axially coordinated carbonyl groups features D₃ symmetry. The coordination about each cobalt atom is trigonal bipyramidal with the equatorial plane composed of three phosphorous atoms from the bridging ligands and the axial carbonyl group

Figure 10. Potential energy diagram for a series of photoreagents and photoproducts each having an excited state allowing for the regeneration of the photoreagent from the thermodynamically stable photoproduct.





Potential Energy

Figure 11. Redox chemistry of $Co_2[CH_3N(PF_2)_2]_3(CO)_2$.

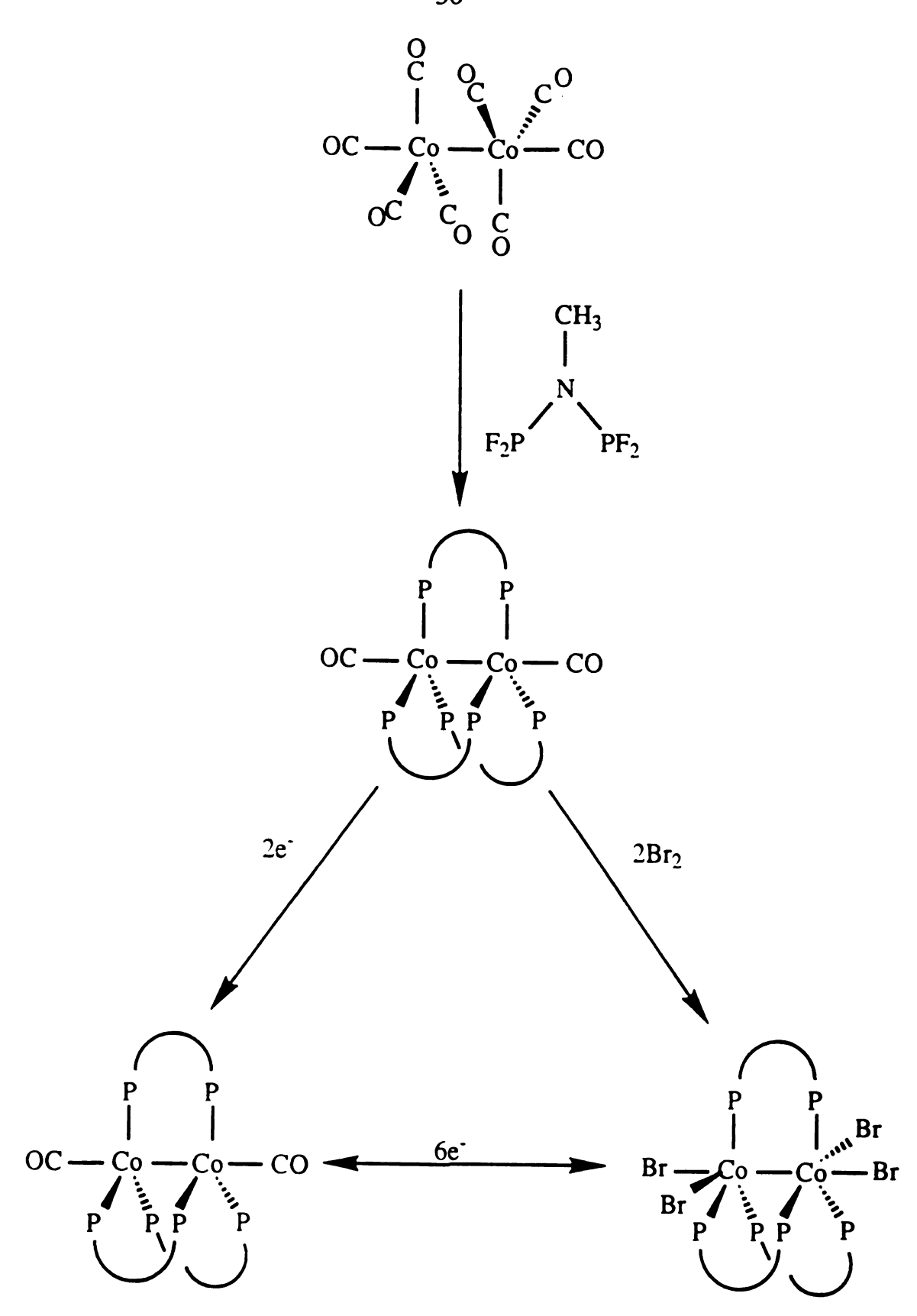


Figure 11

and the neighboring cobalt atom forming the apices of the pyramid. Two electron reduction of Co₂[CH₃N(PF₂)₂]₃(CO)₂ affords a Co₂(-1, -1) anion with the same geometry. Reaction of the parent complex with Br₂ gives Co₂[CH₃N(PF₂)₂]₃Br₄, a Co₂(II,II) complex with C₂ symmetry. The coordination geometry around each cobalt atom is pseudo-octahedral, the equatorial plane occupied by three phosphorous atoms from the fluorophosphine ligands along with a bromine atom. The apices are capped by the neighboring cobalt atom and the axial bromine. Attesting to the fact that the ligand can accommodate significant structural changes, the coordination sphere around each cobalt atom changes from trigonal bipyramidal for Co₂[CH₃N(PF₂)₂]₃(CO)₂ to slightly distorted octahdral structure of the Co₂[CH₃N(PF₂)₂]₃Br₄

The diverse oxidation chemistry engendered by the fluorophosphine ligand has been exploited by our group to prepare a "four electron" series of "two electron" photoreagents.¹⁴ Figure 12 shows the inner coordination sphere of each of the three complexes. The complexes, $[Rh_2(CH_3N(PF_2)_2)_3PF_3], [Rh_2(CH_3N(PF_2)_2)_3(PF_3)Cl_2]$ [Rh₂(CH₃N(PF₂)₂)₃(PF₃)Cl₄] referred to as Rh₂(0,0), Rh₂(0,II)Cl₂ and Rh₂(II,II)Cl₄, each consist of a dirhodium core bridged by three bis(difluorophosphino)methylamine ligands with a terminal PF₃ occupying the axial site on the Rh(0) center. The chlorines on the Rh(II) center are arranged in the axial and equitorial positions. Analogous to the cobalt series of King and coworkers, the coordination about the zero valent rhodium is nearly ideally trigonal bipyramidal with the equatorial plane consisting of three phosphorous atoms from the bridging fluorophosphine ligands and the apical positions occupied by a phosphorous of the terminal PF3 and the other rhodium atom. The coordination sphere of the divalent rhodium is

Figure 12. View of the inner coordination sphere of $Rh_2(0,0)$ (a), $Rh_2(0,II)Cl_2$ (b), and $Rh_2(II,II)Cl_4$ (c). Phosphorous atoms are from the ligand $[CH_3N(PF_2)_2]$ which bridges the two metal centers.

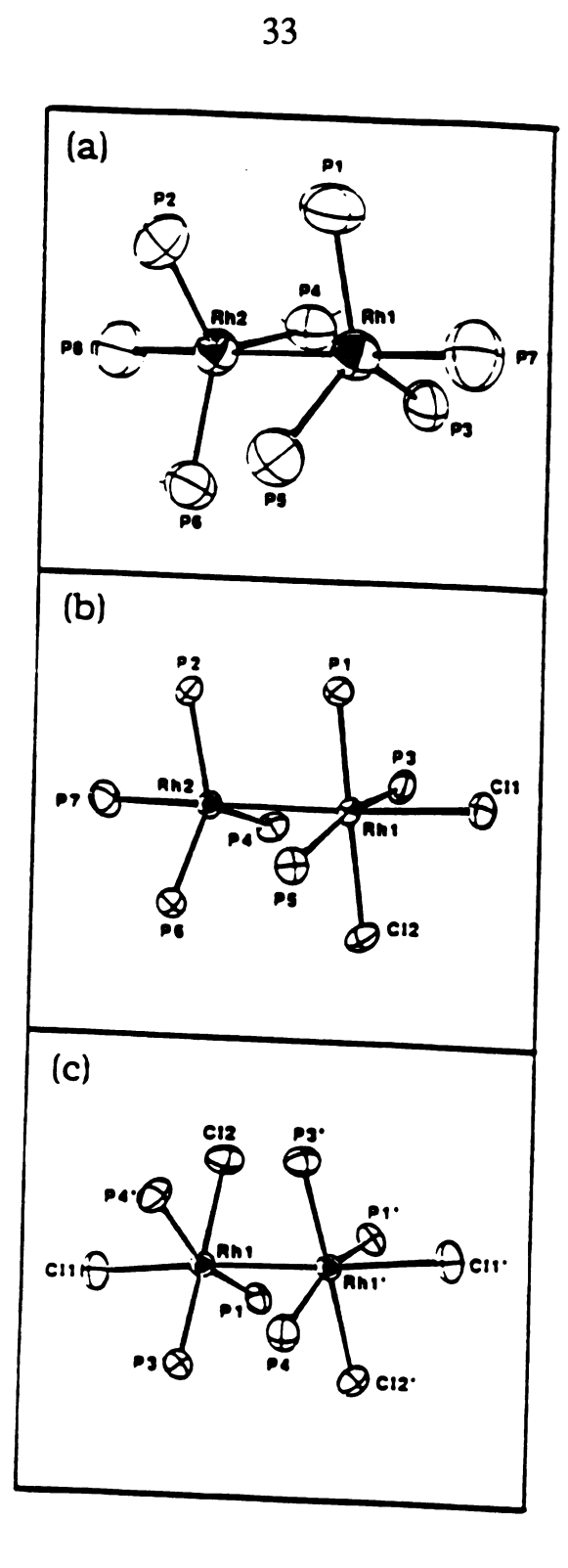


Figure 12

pseudo-octahedral with the three phosphorous atoms from the fluorophosphine ligands and one chlorine forming the equatorial plane. The pseudo-octahedron is completed with an axial chloride and the other rhodium center forming the apices.

Red luminescence is observed from solids and low temperature glasses of all three compounds. Each exhibits an intense band in the red region and Rh₂(0,0) and Rh₂(II,II)Cl₄ feature an additional emission to higher energy. Luminescence from solid Rh₂(II,II)Cl₄ can be detected up to room temperature while emission from the other two complexes reaches the limits of our instrumentation at ~ 220 K. The emission spectra of all the complexes are vibrationally featureless even at temperatures as low as 10 K. There is a slight variation in the emission maximum of the Rh₂(0,II)Cl₂ complex varying from 730 to 780 nm depending on the preparation method used.¹⁵ The observation of luminescence from the complexes opens the possibility for regeneration of the Rh₂(0,0) complex from either of the other two because there exists an excited state allowing for escape from the thermodynamic well of the metal-halide bonds.

The focus of my work begins with the achievement of an intimate understanding of the photophysical properties of these systems. This knowledge may then be used toward the exploitation of the photochemical driving force of the excited states of the compounds in escaping the thermodynamic barriers of metal-halide complexes. Prior to attempting photochemistry with the complexes, more detailed spectroscopy is necessary. Characterization of the electronic absorbance transitions must be made and a thorough understanding of the emissive excited state is necessary to rationally elaborate the reaction chemistry to lead to the desired photoproduct. Chapter Three addresses the spectroscopic characterization of

the compounds. The identification of the electronic absorption transitions is accomplished by comparison of the absorbances as the axially coordinated halides are changed from chloride to bromide and to iodide. The syntheses and characterization of the new compounds are included. The nature and lifetimes of the luminescent excited states are determined through excitation spectroscopy and temperature dependent emission lifetime measurments.

Chapter Four describes the photoreduction chemistry of the new complexes. Some interesting comparisons to $[Pt_2(pop)_4X_2]^{4-}$ photochemistry are noted and some emerging trends in reductive elimination photochemistry recognized.

Chapter Two

Experimental

A. Solvent Purification

1. Synthesis

All solvents for synthetic use were refluxed under N₂ for no less than 8 hours and freshly distilled prior to use. Hexane, cyclohexane, pentane diethyl ether, benzene toluene and tetrahydrofuran were refluxed over sodium. In the case of the latter three solvents, small amounts of benzophenone were added to form the blue or purple ketyl radical anion or dianion, respectively, as an indicator of water content. Methylcyclohexane and acetonitrile were refluxed over calcium hydride and all halogenated solvents were refluxed over P₂O₅.

2. Photochemistry and Spectroscopy

All solvents used for UV-Visible spectroscopy and photochemistry were spectroscopic grade (Burdick and Jackson Laboratories) or HPLC grade (Aldrich). Each of the solvents was deoxygenated by the freeze-pump-thaw method (10^{-6} torr) and then vacuum distilled into storage flasks

equipped with Kontes high-vacuum stopcocks. Dichloromethane was stored over Linde 4 Å molecular seives, which had been activated under dynamic vacuum (10-6 torr) at 250 °C for 12 hours. Hexane, benzene, toluene and tetrahydrofuran were stored over mixtures of sodium-potassium alloy. Small amounts of benzophenone were added to the latter three solvents. Because of the high water content of THF, it was first predried for two days over sodium / benzophenone and then vacuum transferred to a storage flask containing the Na/K alloy and benzophenone indicator.

Solvents used for NMR spectroscopy were deuterated THF, (Cambridge Isotope Laboratories, 99.95%) dichloromethane (Cambridge Isotope Laboratories, 99.96%) and chloroform (Cambridge Isotope Laboratories, 99.8%). THF was dried over sodium for 48 hours, vacuum transferred into a storage flask and deoxygenated by the freeze-pump-thaw method (10-6 torr) before use. Dichloromethane and chloroform were deoxygenated by the freeze-pump-thaw method (10-6 torr) and vacuum distilled into a storage flask containing Linde 4 Å molecular seives, which were activated as described in the previous paragraph.

B. Synthesis

1. General Procedures

All synthetic manipulations and filtrations, unless otherwise noted were performed under a purified argon atmosphere using standard Schlenk-line techniques with rigorously deoxygenated and dried solvents. All chemicals were reagent grade and used as received unless otherwise noted.

Cobaltocene was purchased from Aldrich Chemical Company and phosphorous trifluoride was obtained from Ozark-Mahoning Company.

2. Synthesis of Starting Compounds

The bis(diflurophosphino)methylamine ligand was prepared by the method of Nixon¹⁶ and characterized by ¹H NMR spectroscopy. [RhCl(PF₃)₂]₂, [RhBr(PF₃)₂]₂ and [RhI(PF₃)₂]₂ were prepared by literature methods ¹⁷ as was Cl₂IC₆H₅.¹⁸ The compounds Rh₂(0,II)Cl₂ and Rh₂(II,II)Cl₄ used for lifetime studies were prepared by Dr. Joel Dulebohn and those used for photochemistry were prepared according to his methods (Rh₂(0,II)Cl₂ was prepared by method ii).¹⁵ The latter two compounds were characterized by UV-Visible, and ¹H NMR spectroscopy

3. Synthesis of Dirhodium Fluorophosphine Bromide Complexes

a. Rh₂[μ-CH₃N(PF₂)₂]₃[(PF₂)NCH₃(F₂P)]Br₂ (1). The starting material [RhBr(PF₃)₂] was obtained by reacting [RhCl(PF₃)₂]₂ with excess NaBr. ¹⁴ Upon addition of CH₃N(PF₂)₂ (0.50 mL, 4.3 mmol) to [RhBr(PF₃)₂]₂ (0.13 g, 0.184 mmol) in 15 mL of benzene, the yellow solution turned dark red and PF₃ gas was liberated. The solution color lightened within seconds. Following nine hours of heating at reflux temperature the red-orange precipitate of the Rh₂(0,II)Br₂ compound was collected by filtration, washed with benzene, and dried under vacuum. Various methods were employed in an effort to obtain crystals suitable for X-ray crystallographic analysis. Among these were slow evaporation of a CH₂Cl₂ solution of the complex, diffusion of hexane vapor into a CH₂Cl₂

solution of the complex, and diffusion of a solvent in which the complex is insoluble into a solution of the compound. Various solvent systems were tried including acetone / hexane, THF / hexane, CH₃CN / hexane CH₂Cl₂ / benzene, CH₂Cl₂ / hexane. The systems were layered in a variety of ratios of the two solvents and some were allowed to diffuse at room temperature while others were kept at 0° C. Most crystallization attempts yielded crystals, however they were either multiples or were too small to be useful. Crystals suitable for X-ray studies were obtained from slow diffusion of hexane into a solution of the compound in CH₂Cl₂ at room temperature. This method, however was not invariably successful and yielded unsuitable crystals many times prior the successful attempt. Identification of the compound was made by mass spectrometry and X-ray crystallography.

b. Rh₂[CH₃N(PF₂)₂]₃Br₄ (2). In a typical synthesis, CH₃N(PF₂)₂ (0.2 mL, 1.73 mmol) was added via syringe to a 10 mL benzene solution of [RhBr(PF₃)₂]₂ (0.16 g, 0.22 mmol) causing the solution to turn from yellow to dark red and PF₃ gas to be evolved. The color of the mixture lightened within seconds. This reaction mixture was charged with bromine (0.02 mL, 0.39 mmol) and the solution was heated at reflux temperature for 3.5 hours. The solvent volume was reduced by two-thirds under an argon flow, and hexane (6 mL) was added to promote precipitation. The ensuing precipitate was filtered and dried under vacuum. Numerous attempts to obtain X-ray quality crystals of 2 were made by diffusing a solvent in which the complex was insoluble into a solution of the compound in another solvent. The solvent systems tried were CH₂Cl₂ / benzene, acetone / hexane, acetone / pentane, and CH₂Cl₂ / hexane employing various ratios of each solvent in each system. X-ray quality crystals were obtained by diffusion of hexane into a CH₂Cl₂

solution of the complex. This method was not always successful. Although always yielding crystals, many times the crystals obtained were either multiples or too small for X-ray analysis. Identification of the compound was made by mass spectrometry and X-ray crystallographic analysis.

4. Synthesis of Dirhodium Fluorophosphine Iodide Complexes

- a. Rh₂[µ-CH₃N(PF₂)₂]₃[(PF₂)CH₃N(F₂P)]I₂ (3). The starting material [RhI(PF₃)₂]₂ was obtained by the reaction of [RhCl(PF₃)₂]₂ with excess NaI. ¹⁴ To a solution of [RhI(PF₃)₂] (0.1820 g, 0.223 mmol) in 10 mL of benzene was added CH₃N(PF₂)₂ (0.17 mL, 1.46 mmol). The mixture turned dark red and PF₃ gas was liberated. The solution color then lightened. This mixture was stirred for 2 hours, after which time the ensuing precipitate was filtered under argon, washed with benzene and dried under vacuum. After numerous attempts employing the same methods used to obtain crystals of 1, X-ray quality crystals of the compound were grown from CH₂Cl₂ solutions of the complex layered with hexane. The compound was identified by mass spectrometry and X-ray crystallography.
- b. Rh₂[CH₃N(PF₂)₂]₃I₄ (4). The starting material for this synthesis was Rh₂[CH₃N(PF₂)₂]₃(PF₃)₂ which was provided by Dr. Joel Dulebohn and was prepared according to methods described elsewhere. To a solution of Rh₂[CH₃N(PF₂)₂]₃(PF₃)₂ (0.0343 g, 0.0388 mmol) in 10 mL of benzene was added I₂(s) (0.0637 g, 0.251 mmol) and the solution was heated to reflux temperature for two hours. The mixture was cooled and the solvent volume was reduced by half under an argon flow at which time hexane was added to promote precipitation. No precipitate was obtained and the solvent was

removed by vacuum, yielding a dark solid. The ensuing solid was redissolved in benzene and precipitated with hexane two times. The final solid compound was filtered under argon and dried under vacuum. The compound was characterized by mass spectrometry. Attempts to obtain crystals suitable for X-ray crystallographic analysis were made using methods described in Section 3 (a) and all resulted in multiples.

5. Synthesis of Rh₂[μ -CH₃N(PF₂)₂]₃[(PF₂)NHCH₃)₂ (5)

The starting material [RhCl(PF₃)₂]₂ (0.070 g, 0.111 mmol) was dissolved in 15 mL of CH₂Cl₂ and CH₃N(PF₂)₂ (0.12 mL, 1.03 mmol) was added via syringe. After PF₃ gas was evolved, cobaltocene (0.10 g, 0.528 mmol) was added. The solution was stirred for one-half hour during which time PF₃(g) was slowly bubbled in. The solution was filtered under argon and the filtrate was taken to dryness under vacuum. The resulting product was dissolved in CH₂Cl₂, introduced onto a Florasil column and eluted with 15% CH₂Cl₂ in hexane. The product was characterized by mass spectrometry and NMR and IR spectroscopy.

C. Spectroscopic Instrumentation and Methods

1. Electronic Absorption Spectroscopy

Electronic absorption spectra were recorded on either a Cary 17 or Varian 2300 UV-Vis-NIR spectrometer. Molar absorptivities were determined using 1 cm quartz cuvettes, by standard procedures from solutions prepared in a glove box and calculated from Beer-Lambert plots of at least four experimental points.

2. Steady-State Luminescence Spectroscopy

Steady-state luminescence spectra were recorded on a high resolution emission spectrometer constructed at Michigan State University. ¹⁹ Excitation light ($\lambda = 365$ nm) from a 200 W Xe-Hg lamp was selected by a double monochromator in conjunction with an Oriel 365 nm interference filter. The luminescence from the sample was directed through a single monochromator and onto a dry ice cooled PMT (R-316-02 Hamamatsu). A 715 nm cutoff filter was installed in front of the emission monochromator and slit widths were 5 mm / 5 mm and 3 mm / 3 mm for excitation and emission monochromators, respectively. Samples employed for measurements were in crystalline or powder form in EPR tubes that were immersed in liquid nitrogen in a finger Dewar flask.

3. Excitation Spectroscopy

Unpolarized excitation spectra were recorded on the aforementioned emission spectrometer with modifications fully described elsewhere.²⁰ Samples were prepared and handled in the same manner as described for emission measurements.

4. Time Resolved Luminescence Spectroscopy

A Nd:YAG pulsed laser system (λ = 355 nm, fwhm = 8 ns) was employed for lifetime measurements. Temperature dependent measurements were achieved by cooling of the samples with an Air Products cryogenic system, by methods described elsewhere,²¹ with a slight modification of the sample preparation procedure for the dirhodium fluorophosphine bromide complexes. The samples were dissolved in CH₂Cl₂, deposited on the sample holder and allowed to dry under an argon atmosphere in a glove box. Data fitting was accomplished by the use of KaleidaGraph data analysis / graphics application program published and distributed by Synergy Software.

5. Nuclear Magnetic Resonance Spectroscopy

The NMR spectra were recorded at the Max T. Rogers NMR facility at Michigan State University. The $^{31}P\{^{1}H\}$ NMR spectra were recorded on a Varian VXR-300S spectrometer Phosphorous chemical shifts are reported in parts per million (δ scale), and measured relative to 85% H₃PO₄. Positive chemical shifts are downfield from the standard. The ^{1}H spectra were recorded on either a Varian VXR-300S or Varian Gemini 300 spectrometer and chemical shifts were referenced to the chemical shifts of the deuterated solvent.

6. Mass Spectrometry

The fast atom bombardment mass spectra (FABMS) were recorded on a JEOL HX 110 double focusing mass spectrometer housed in the NIH / MSU

Mass Spectrometry Facility. Samples were dissolved in o-nitrobenzyl alcohol matrices. The acceleration potential for this work was 10 kV. Data were acquired, stored, and processed on a JEOL DA5000 data system. Fast Atom Bombardment (FAB) ionization was performed using a 6 kV neutral beam of Xenon atoms.

7. Infrared Spectroscopy

Infrared spectra were obtained as KBr pellets on a Nicolet IR/42 spectrometer.

D. Crystal Structure Determinations

1. General Procedures

Crystal structure determinations were performed by Dr. Donald L. Ward of the X-ray Crystal Structure Facility at Michigan State University. The diffraction data for the complexes were collected on a Rigaku AFC6S diffractometer using graphite monochromated MoK α (λ = 0.71069 Å) radiation and a 2 KW sealed tube generator. The intensity data were collected by using ω - 2 θ scans at a rate of 4.0 / min (in ω ; three rescans) for Rh₂[μ -CH₃N(PF₂)₂]₃[(PF₂)NCH₃(F₂P)]Br₂, 16.0 / min (in ω ; two rescans) for Rh₂[μ -CH₃N(PF₂)₂]₃[(PF₂)NCH₃(F₂P)]I₂. Calculations were performed on a VAX 11/750 computer using the TEXSAN ²² crystallographic software package provided by Molecular Structure Corporation.

2. Methods

a. Rh₂[μ -CH₃N(PF₂)₂]₃[(PF₂)NCH₃(F₂P)]Br₂ (1) A deep maroon irregular crystal of 1 (approximate dimensions, 0.14 × 0.20 × 0.30 mm) was mounted at the end of a glass fiber and coated with N-Paratone oil. The cell parameters and an orientation matrix were obtained from a least squares refinement of 25 reflections in the range 15.50 < 20 < 19.21. The space group was found to be P2₁2₁2₁.

A total of 2614 reflections were collected at a temperature of $-90 \pm 3^{\circ}$ C. The structure was solved by direct methods. The non-hydrogen atoms were refined anisotropically. The final cycle of full-matrix least squares refinement was based on 1748 observed reflections (I > 3.00 σ (I)) and 320 variable parameters and converged (largest parameter shift was 0.11 times it's esd) with weighted and unweighted agreement factors of 0.052 and 0.062, respectively. The largest peak in the final difference map was 1.12e / Å³.

b. Rh₂[CH₃N(PF₂)₂]₃Br₄ (2) An orange irregular crystal of 2 (approximate dimensions, $0.08 \times 0.12 \times 0.20$ mm) was mounted on a glass fiber. The cell parameters and an orientation matrix were obtained from a least squares refinement using the setting angles of six carefully centered reflections in the range 20.48 < 20 < 22.61 corresponding to a monoclinic cell. The space group was determined to be C2/c.

The data were collected at a temperature of 23 ± 1 °C. A total of 2389 reflections were collected of which 2279 were unique. The intensities of three representative reflections, which were measured after every 150 reflections, declined by 0.080%. A linear correction factor was applied to the data to account for this phenomenon. The structure was solved by direct

methods. The non-hydrogen atoms were refined either anisotropically or isotropically. The final cycle of full-matrix least squares refinement was based on 729 observed reflections (I > 3.00σ (I)) and converged (largest parameter shift was 0.01 times it's esd) with weighted and unweighted agreement factors of 0.058 and 0.056, respectively. The largest peak in the final difference map was 1.09 e / Å³.

c. $Rh_2[\mu-CH_3N(PF_2)_2]_3[(PF_2)NCH_3(F_2P)]I_2$ (3). A dark red irregular crystal of 3 (approximate dimensions $0.06 \times 0.12 \times 0.17$ mm) was mounted on a glass fiber. Cell parameters and an orientation matrix were obtained from a least squares refinement using the setting angles of seven carefully centered reflections in the range $5.72 < 2\theta < 15.80$ corresponding to an orthorhombic cell. The space group was determined to be $P2_12_12_1$.

The data were collected at a temperature of 23 ± 1 °C, and a total of 1283 reflections were collected. The intensities of three representative reflections which were measured after every 150 reflections declined by 0.71%. A linear correction factor was applied to the data to account for this phenomenon. The structure was solved and non-hydrogen atoms were refined as for the previous structure. The final cycle of full matrix least squares refinement was based on 800 observed reflections (I > 3.00 σ (I)) and 165 variable parameters and converged (largest parameter shift was 0.00 times it's esd) with unweighted and weighted agreement factors of 0.059 and 0.069 respectively. The largest peak in the final difference map was 1.03 e / Å3.

E. Photochemistry

Photoreactions were monitored in a specially adapted high-vacuum UV-Vis cell consisting of a 1 cm quartz cuvette and a 10 mL side-arm. The two chambers were separated by two Kontes high-vacuum quick release Teflon stopcocks. The samples were placed in the cuvette and the photoreagent (CH₃N(PF₂)₂ when used) was transferred to the 10 mL side-arm by high vacuum distillation. After freeze-pump-thaw degassing of the photoreagent (10-6) the appropriate solvent was then transferred to the side-arm bulb by high vacuum distillation. After subsequent freeze-pump-thaw cycles the photoreagent and solvent were mixed with the sample. When photolysis was carried out in only the presence of solvent, the sample was placed in the cuvette and the solvent was vacuum distilled into the sidearm. After freeze-pump-thaw degassing of the solvent, it was mixed with the sample.

Irradiations were performed using an Oriel 1000 W Xe / Hg high pressure lamp, powered by an Oriel 1 kW power supply. The beam was collimated and passed through a circulating water bath which absorbed the IR light and cooled the Schott high-energy cutoff filter used for wavelength selection. The collimated and filtered beam was then focussed onto the sample isolated in a separate glass water circulating bath, by use of an Oriel fused silica lens (f/N = 5). The experimental apparatus used for photolysis is shown in Figure 13. The sample temperatures were thermostatted using a Neslab Exacal 200 water circulator / heater in conjunction with a Neslab 200 Endocal refrigerator.

Photochemical reactions were followed by UV-Vis spectroscopy,

monitoring the disappearance of absorptions of starting material. Upon completion of the photoreactions, as determined by UV-Vis spectroscopy, solvent was removed from the photoproducts under vacuum.

Figure 13. Experimental apparatus for photolysis.

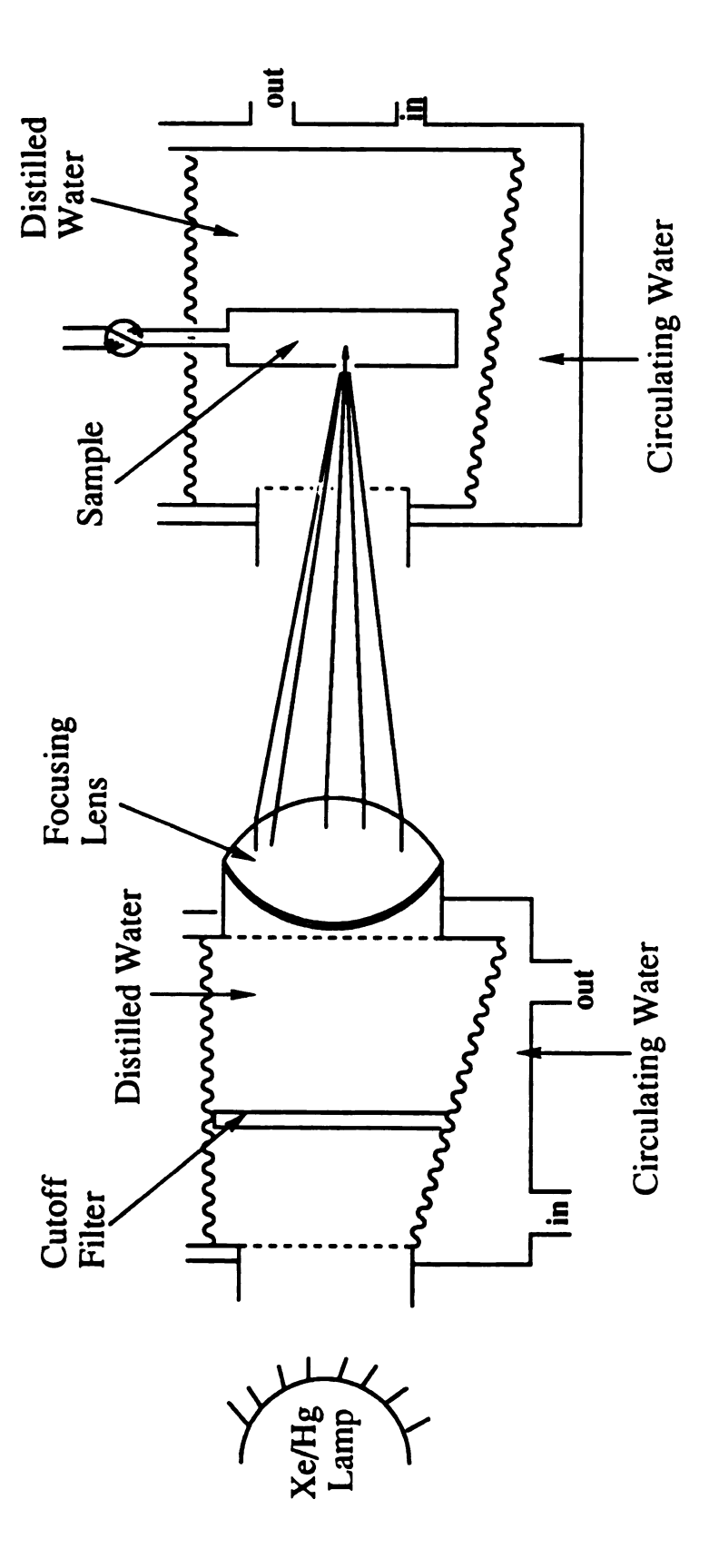


Figure 13

Chapter Three

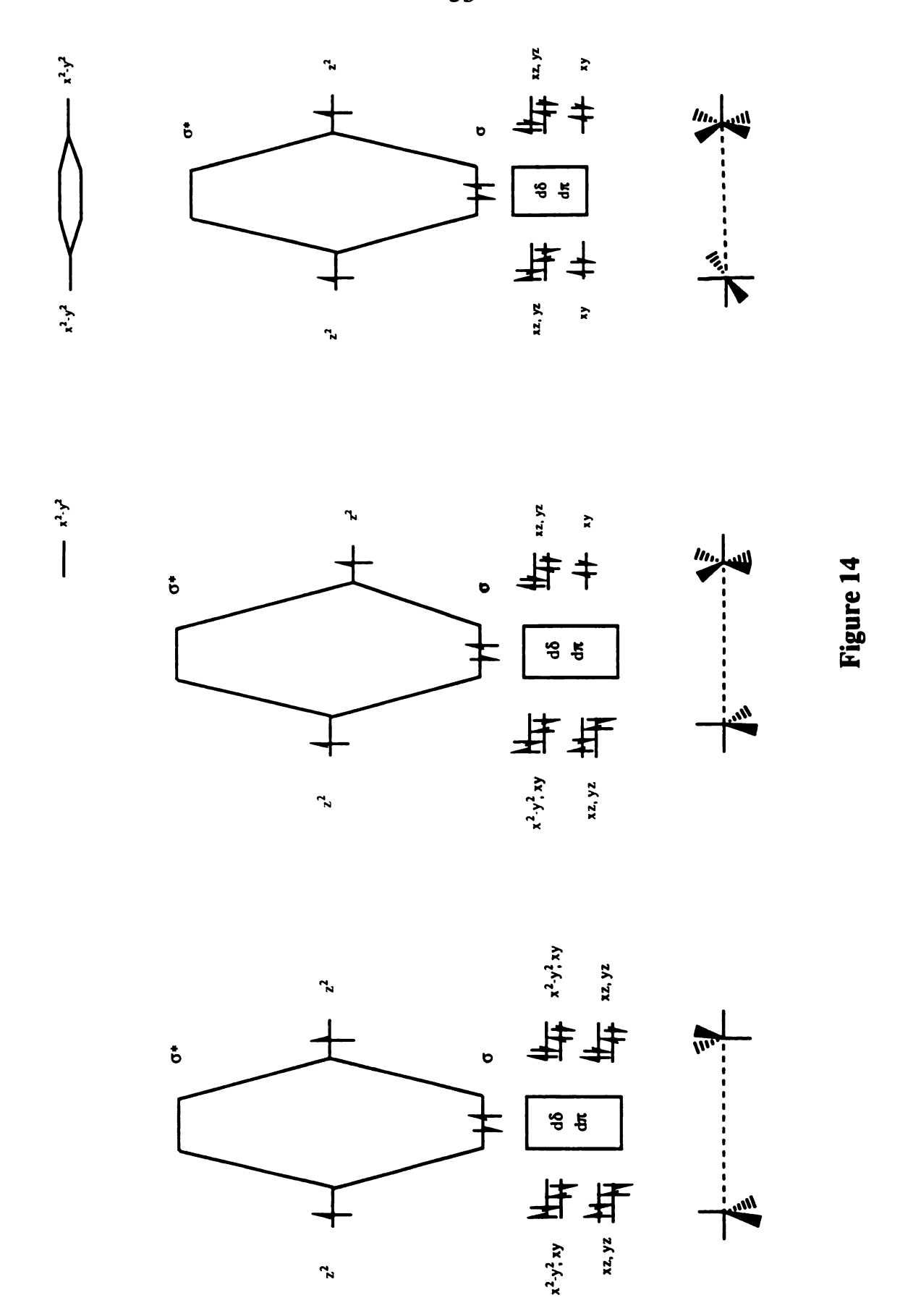
Dirhodium Fluorophosphine Halides: Molecular Structures and Photophysical Properties

A. Introduction

The electronically excited molecule is the crucial reactant in a photochemical transformation. Therefore a clear understanding of the electronic structure and excited state properties of the photoreactant is imperative. To this end, photophysical studies of the dirhodium fluorophosphine complexes were undertaken in an effort to assign the transitions in the absorption spectra of the complexes and determine the nature and lifetimes of the excited states.

We began by considering the simple molecular orbital diagrams of the dirhodium fluorophosphine complexes, shown in Figure 14. MO theory predicts that in the case of the d^9 Rh(0) center, eight electrons reside in orbitals of π (d_{xz} , d_{yz}) and δ (d_{xy} , $d_{x^2-y^2}$) symmetry, with the remaining electron occupying the σ (d_{z^2}) level, as is the case for the Co(CO)₄ fragment of Co(CO)₈.²³ For the case of the d^7 Rh(II) center, we predict six electrons to occupy orbitals of π (d_{xz} , d_{yz}) and δ (d_{xy}) symmetry with the remaining electron occupying the σ (d_{z^2}) level, and the $d_{x^2-y^2}$ level to be destabilized to high energy due to metal-ligand interactions in the equatorial plane; this same

Figure 14. Qualitative energy level diagrams for $Rh_2[CH_3N(PF_2)_2]_3(PF_3)_2$, $Rh_2[CH_3N(PF_2)_2]_3(PF_3)Cl_2$, and $Rh_2[CH_3N(PF_2)_2]_3Cl_4$ generated by mixing of the appropriate C_{3v} and C_{4v} fragments.



picture applies to the Mn(CO)₅ fragment of Mn₂(CO)₁₀.²⁴ MO level diagrams for each of the three complexes can the be formed by mixing of the appropriate fragments. Within this framework, we see that the complexes Rh₂[CH₃N(PF₂)₂]₃(PF₃)₂ and Rh₂[CH₃N(PF₂)₂]₃Cl₄ are isoelectronic with Co₂(CO)₈ and Mn₂(CO)₁₀ respectively with Rh₂[CH₃N(PF₂)₂]₃(PF)₃Cl₂ completing the series. For all three of our dirhodium fluorophosphine complexes the lowest energy transitions are predicted to be $d\pi \rightarrow d\sigma^*$ and $d\sigma \rightarrow d\sigma^*$.

The diagram in Figure 14 does not consider ligand orbitals for simplicity. Let's bring one halide ligand to the metal—metal bond along the axial direction. This orbital can interact with the metal bonding and antibonding pair yielding a σ orbital that is mostly ligand based. As shown in Figure 15, a $Cl(\sigma) \rightarrow d\sigma^*$ transition may be seen for the dichloride and the tetrachloride dinuclear complexes. This introduction of a $L(\sigma) \rightarrow d\sigma^*$ transition has been postulated for other M—M complexes and it is known to red shift on substitution of bromide and more so on substitution of iodide in the complexes,²⁵ whereas the $d\pi \rightarrow d\sigma^*$ transition should remain relatively unaffected by halide substitution.

According to this model, excited state luminescence from the complexes is predicted to arise from the $d\sigma^*$ excited state. Despite the synthesis of several bridged complexes, where photodissociation is prevented by spanning the M—M cores with bidentate ligands, $d\sigma^*$ luminescence has only been recently observed for these types of compounds.²⁶ This fact underscores the subtle electronic factors play in the deactivation of $d\sigma^*$ excited states. Photophysical studies performed by our group on singly bonded LPtIIIPtIIIL (L = Cl, Br, and H₂O) tetraphosphates ²⁷ clearly show

Figure 15. Molecular orbital diagram showing the interaction of Rh₂ with one halide ligand in the axial coordination site. The allowed electronic transitions are indicated by the arrows.

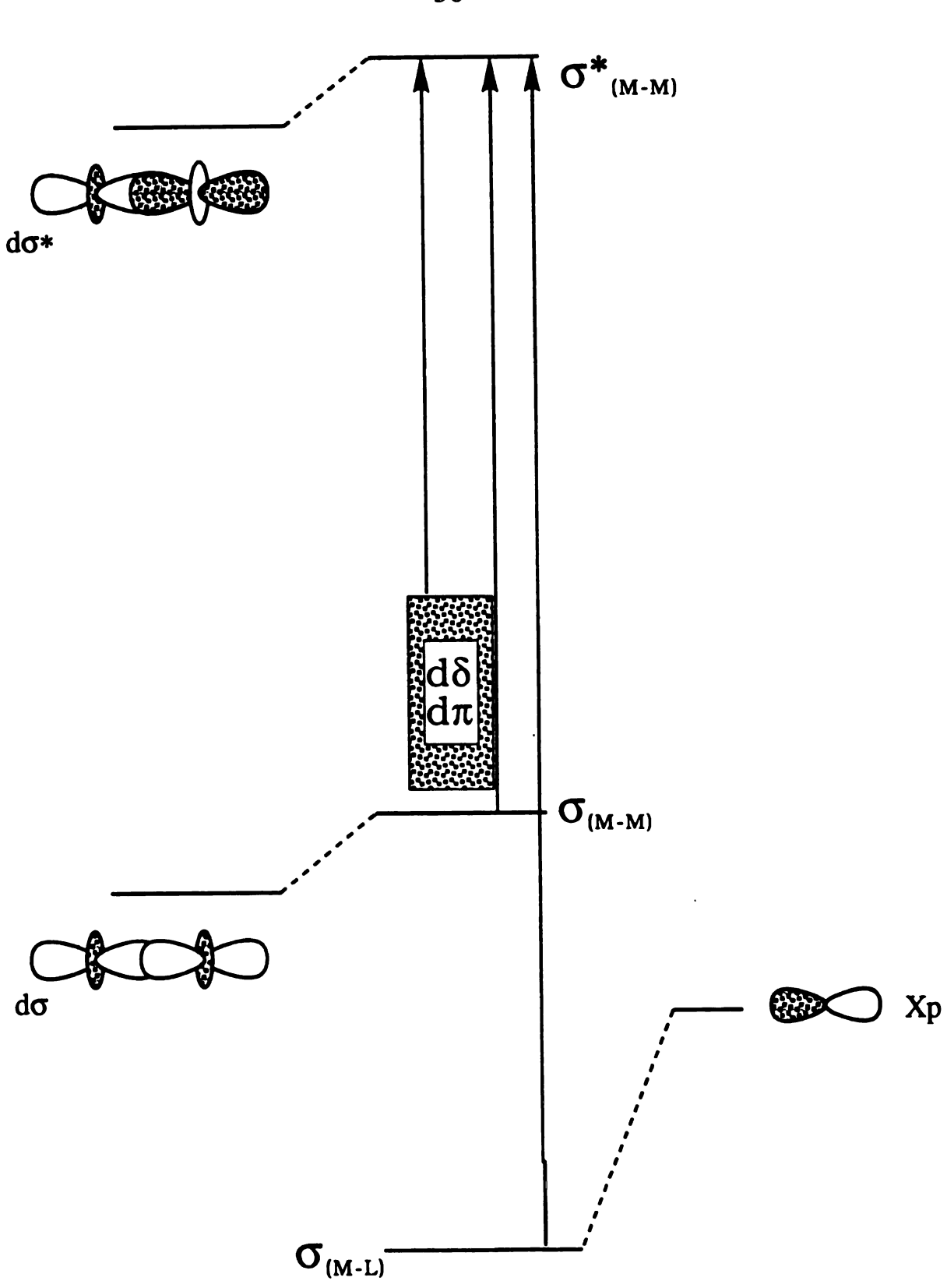


Figure 15

this to be the case. Time resolved spectroscopy of these diplatinum complexes reveals a significant temperature dependence of the $d\sigma^*$ luminescence arising from the thermal population of an E_u state in the $^3(d\pi^*d\sigma^*)$ manifold, which acquires significant singlet character via a spin-orbit coupling mechanism. It is reasonable to consider that luminescence of this series of fluorophosphine complexes is similar to that originating from the $d\pi^*d\sigma^*$ excited state of LPtIIIPtIIIL tetraphosphates.

Our efforts at elaborating the photophysics of the dirhodium fluorophosphine complexes begin with the synthesis and characterization of the parallel bromide and iodide series. X-ray crystallographic studies revealed that whereas the chloride and bromide complexes of Rh₂[CH₃N(PF₂)₂]₃X₄ are structurally analogous, the PF₃ bound axially to Rh(0)center replaced by singly the is a coordinated bis(difluorophosphino)methylamine ligand in the dibromide and diiodide complexes to give $Rh_2[\mu-CH_3N(PF_2)_2]_3X_2.[(F_2P)CH_3N(PF_2)]$ (X = Br, I). Absorption spectra, however suggest the halide congeners to be electronically similar. Electronic transitions followed the postulated molecular orbital model, allowing the absorption spectral transitions to be identified. Characteristics of emission from the complexes are also consistent with the proposed molecular orbital scheme and suggestive of a $d\sigma^*$ emissive state. Temperature dependent emission lifetime studies reveal long lived emission at temperatures below 100 K followed by a monotonic increase in efficient nonradiative decay analogous to the platinum tetraphosphates.

B. Results and Discussion

1. Synthesis

The compounds $Rh_2[\mu-CH_3N(PF_2)_2]_3[(PF_2)NCH_3(F_2P)]Br_2$ and Rh₂[µ-CH₃N(PF₂)₂]₃[(PF₂)NCH₃(F₂P)]I₂ are obtained from the reaction of the symmetric Rh₂(I,I) complexes, [RhBr(PF₃)₂] and [RhI(PF₃)₂], respectively with an excess of bis(difluorophosphino)methylamine. The reactions proceed smoothly yielding the Rh(0,II)Br2 or Rh(0,II)I2 cores ligated by three bridging fluorophosphine ligands. Similar to our observations for the analogous chloride complex, the reaction corresponds to an intramolecular disproportionation of the Rh₂(I,I) starting material. When Br₂ is introduced to the [RhBr(PF₃)₂] complex in the presence of the bidentate fluorophosphine, the two electron mixed valence compound is not stable and the fully oxidized Rh₂(II,II)Br₄ core is obtained. The fully oxidized Rh₂(II,II)I₄ complex is obtained from direct oxidation of Rh₂(0,0). The dirhodium fluorophosphine halide complexes were characterized by mass spectroscopy and the bromide compounds and the diiodide complex were characterized by x-ray crystallography. X-ray quality crystals of the tetraiodide complex were never obtained.

2. Characterization and Structural Interpretation

a. Fast Atom Bombardment Mass Spectrometry

Figure 16 shows the isotope intensity pattern arising from compounds containing varying numbers of bromine atoms.²⁸ Comparison of this figure

Figure 16. Isotope peak intensity pattern for ions containing the indicated number of bromine atoms, taken from Reference 28.

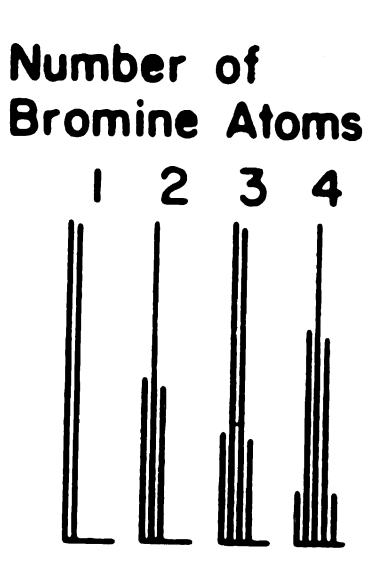


Figure 16

to the mass spectra of the compounds shows the correct number of bromine atoms present for all the proposed fragments. Figure 17 is the mass spectrum of $Rh_2[\mu\text{-CH}_3N(PF_2)_2]_3[(PF_2)NCH_3(F_2P)]Br_2$ in the mass / charge [M/Z] range 600-1000 amu. A molecular ion peak is not observable for this dimer. The highest formula weight peak at 965 amu corresponds to loss of PF_2 from the complex. Peaks at 884 amu and 866 amu, respectively indicate loss of one bromine and loss of a fluorophosphine ligand. Observable peaks at 785, 699, and 618 amu correspond to loss of bromine and a fluorophosphine, loss of two fluorophosphines, and loss of a bromine and two fluorophosphines. To rule out the possibility of the formation during synthesis of the hydrolysis product, $Rh_2[\mu\text{-CH}_3N(PF_2)_2]_3[(PF_2)CH_3NH]Br_2$, infrared spectroscopy was performed. No N—H stretch was observed in the IR spectrum.

The FAB mass spectra of Rh₂[CH₃N(PF₂)₂]₃Br₄ in the [M / Z] range of 650-1050 is presented in Figure 18. No molecular ion peak is observed. Fragmentation peaks at 947, 866, 788, 699, and 618 amu correspond to loss of one bromine, two bromine, one bromine and one fluorophosphine ligand, two bromine and one fluorophosphine, and three bromine and one fluorophosphine.

Displayed in Figure 19 is the FAB mass spectrum of Rh₂[µ- $CH_3N(PF_2)_2]_3[(PF_2)NCH_3(F_2P)]I_2$ in the [M/Z] range 600-1100 amu. As with the complex $Rh_2[\mu-CH_3N(PF_2)_2]_3[(PF_2)NCH_3(F_2P)]Br_2$ a molecular ion is not observed. The peak of the highest mass at 1060 amu corresponds to loss of PF₂ from the complex. Peaks at 960 and 834 amu correspond to loss of one fluorophosphine ligand and one flourophosphine and one iodine. Fragmentation peaks at 793 and 666 amu show loss of two fluorophosphine ligands and two fluorophosphines and one iodine. The peak at 932 loss of PF₂ iodine. corresponds to and one

Figure 17. FAB mass spectrum of $Rh_2[\mu\text{-CH}_3N(PF_2)_2]_3$ - $[(PF_2)NCH_3(F_2P)]Br_2$ in the mass / charge range 600-1000 amu.



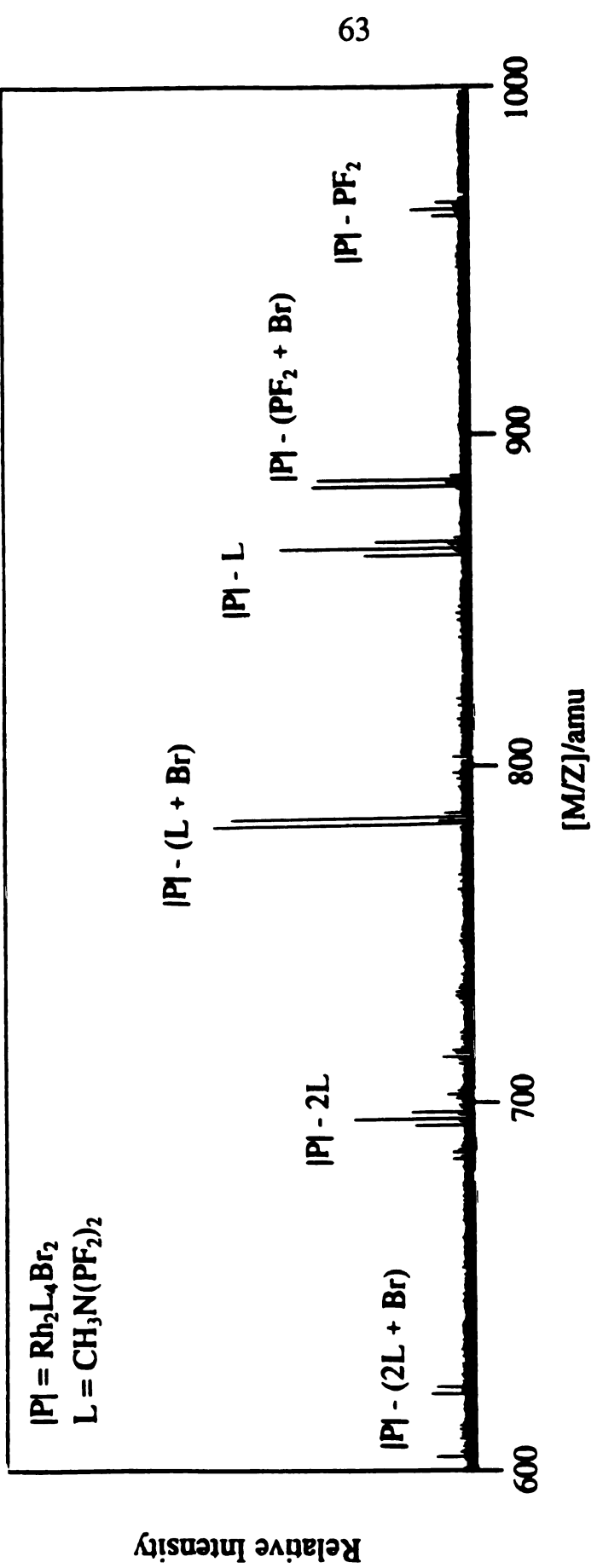


Figure 17

Figure 18. FAB mass spectrum of $Rh_2[CH_3N(PF_2)_2]_3Br_4$ in the mass / charge range 600-1100 amu.

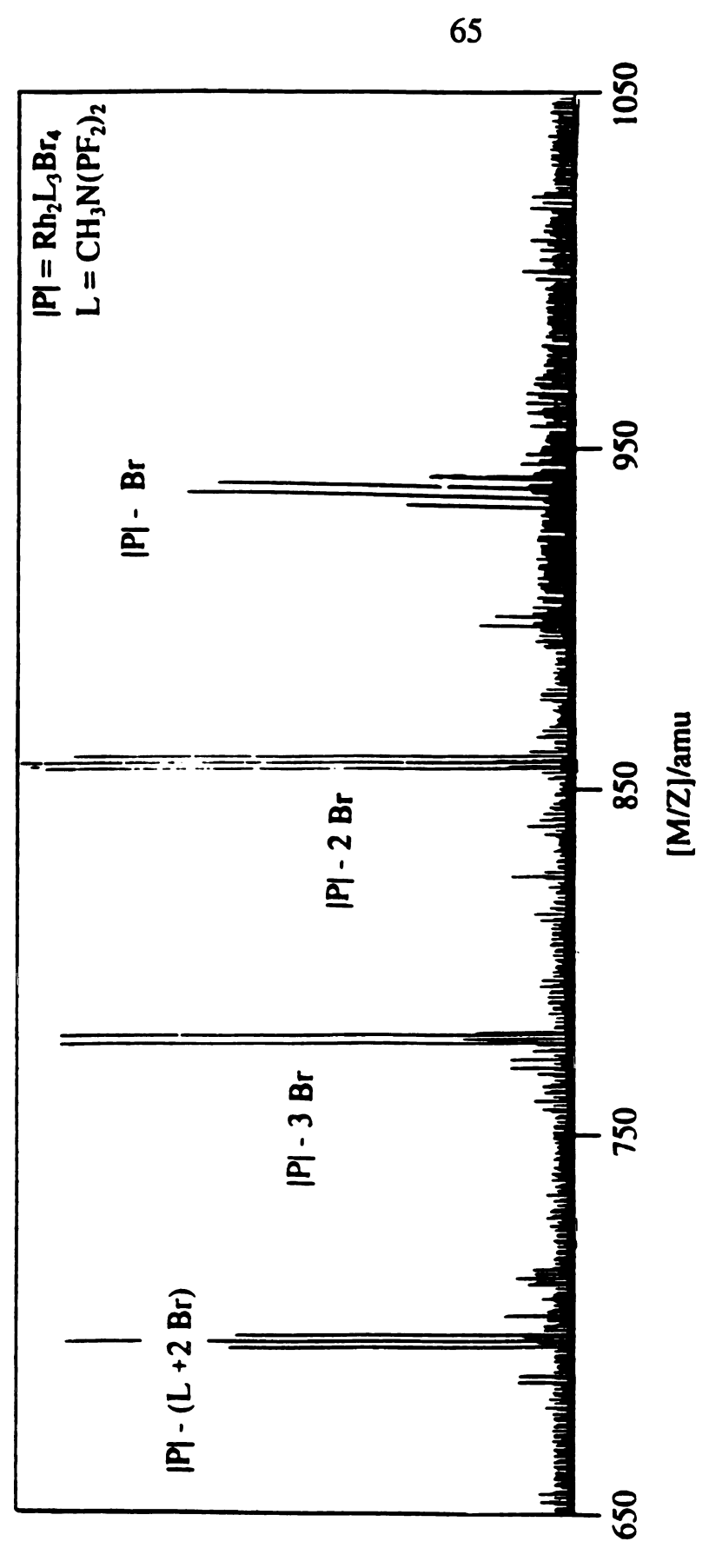


Figure 18

Figure 19. FAB mass spectrum of $Rh_2[\mu-CH_3N(PF_2)_2]_3-[(PF_2)NCH_3(F_2P)]I_2$ in the mass / charge range 600-1100 amu.

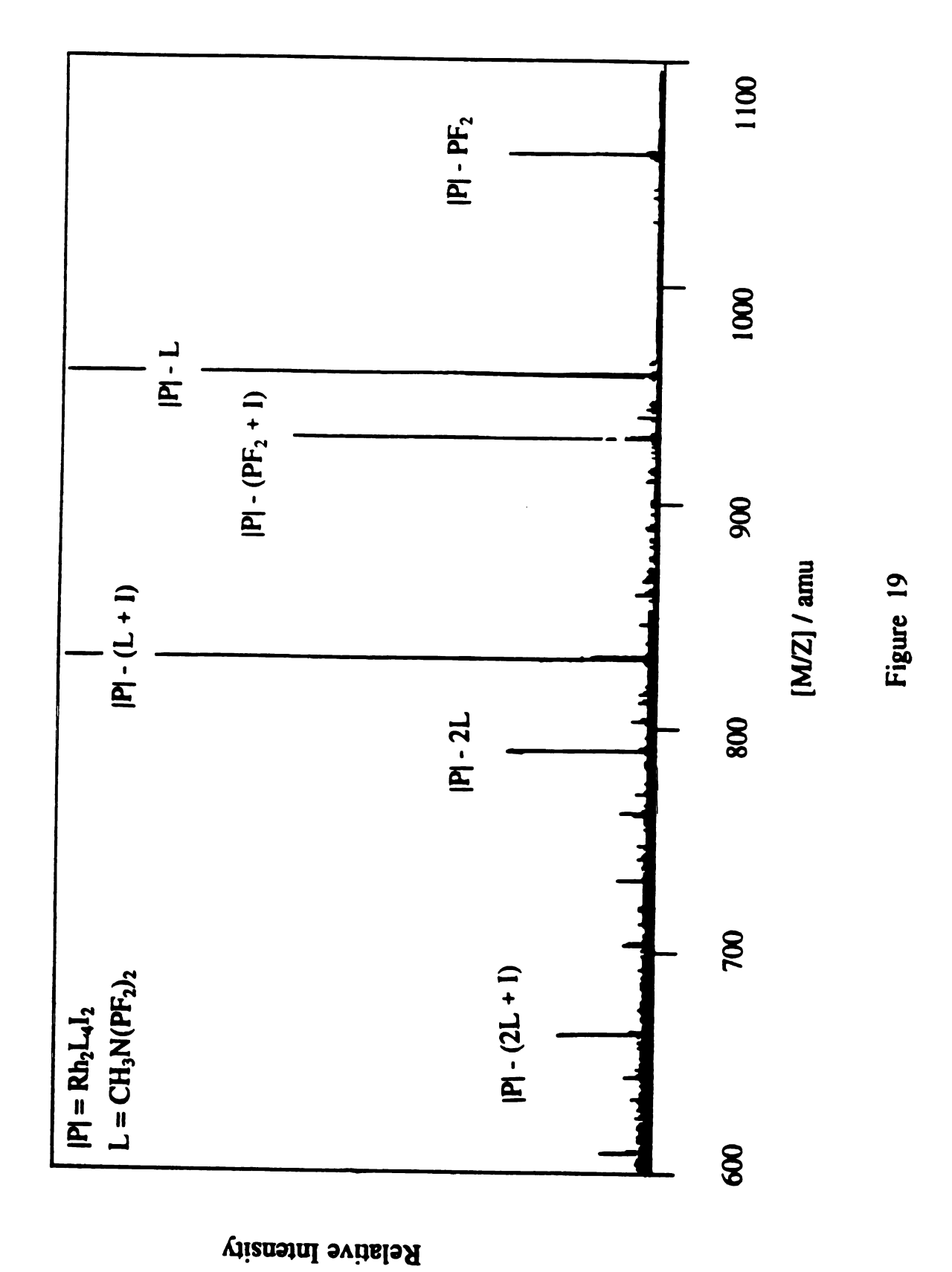


Figure 20. FAB mass spectrum of Rh₂[CH₃N(PF₂)₂]₃I₄ in the mass / charge range 700 – 1100 amu. Molecular ion peak is shown in the inset.

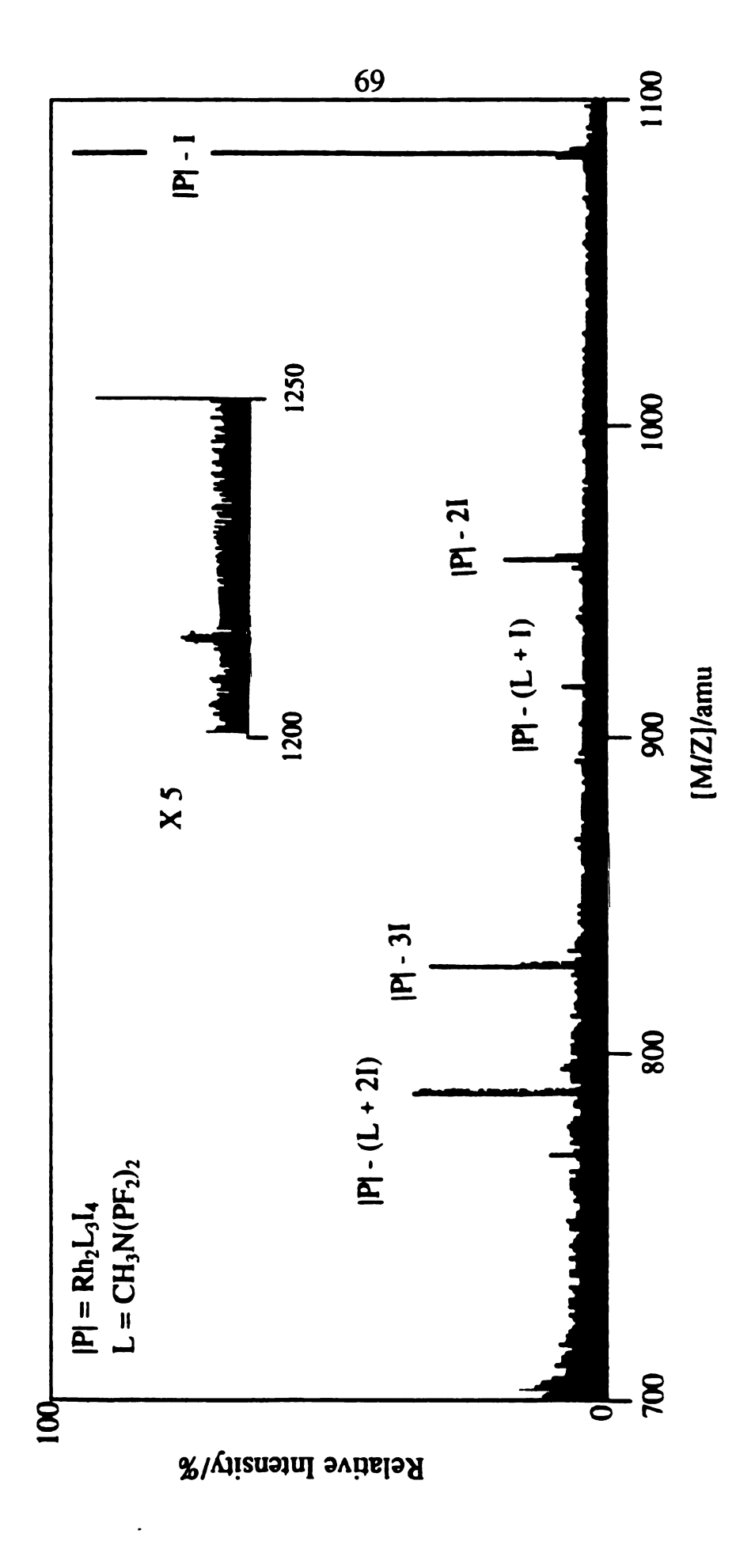


Figure 20

Shown in Figure 20 is the FAB mass spectrum of the complex Rh₂[CH₃N(PF₂)₂]₃I₄ in the [M/Z] range 700-1100 amu. A small molecular ion peak is observed at 1215 amu, as shown in the inset. Peaks in the spectrum correspond to loss of one iodine at 1088 amu, two iodine at 961 amu, one iodine and one fluorophosphine at 921 amu, three iodine at 834 amu, and two iodines and two fluorophosphines at 794 amu.

b. X-ray Crystallography

Crystal parameters and details of intensity collection for 1, 2 and 3 are listed in Table 1. Positional parameters for 1, 2 and 3 are given in Tables 2-4, respectively.

The ORTEP diagrams of the complexes 1, 2 and 3 are shown in Figures 21-23. The structural features observed for the Rh₂(0,II)Cl₂ and Rh₂(II,II)Cl₄ cores are retained in these complexes with trigonal bipyramidal geometry observed about the Rh(0) center and a pseudo-octahedral coordination sphere surrounding the Rh(II) center. Preference for axial coordination of only one phosphorous of the ligand CH₃N(PF₂)₂ as opposed to coordination of a small π -accepting ligand such as PF₃ has been observed previously in the reaction of Co₂(CO)₈ with CH₃N(PF₂)₂ to yield Co₂[CH₃N(PF₂)₂]₃[(PF₂)NCH₃(F₂P)]₂. ²⁹

Inspection of selected bond distances as given in Tables 5-7 reveal trends similar to those observed for the compounds Rh₂(0,II)Cl₂ and Rh₂(II,II)Cl₄¹¹. In all cases the Rh—X bond trans to a Rh—P bond are significantly shorter than Rh—X bonds trans to the Rh—Rh axis. Along the same lines, Rh—P bonds which are trans to a halide are consistently shorter than Rh—P bonds which are trans to another phosphorous. These trends

were previously explained by simple bonding considerations. The good π accepting ability of the fluorophosphine ligand should enhance the π donation from trans halide atoms. Accordingly, the π backbonding between the rhodium and the halide will be strengthened resulting in a shortening of the Rh—X_{eq} or Rh—P bond trans to the halide. The dirhodium complexes display bond lengths characteristic of Rh—Rh single bonds, 30 which arise from the pairing of an odd electron residing in the d_z^2 orbital of the d^9 Rh(0) fragment or the d⁷ Rh(II) fragment to yield species with d-electron configurations of $(d^8)d^1-d^1(d^8)$, $(d^8)d^1-d^1(d^6)$ and $(d^6)d^1-d^1(d^6)$, for the Rh₂(0,0), Rh₂(0,II)X₂ and Rh₂(II,II)X₄ cores, respectively. The increase in Rh—Rh bond length along the series $Rh_2(II,II) < Rh_2(0,II) < Rh_2(0,0)$ that was seen for the chloride series and explained by the larger atomic radius of Rh(0) as compared to Rh(II) is preserved in the X=Br and X=I complexes also. Both axial and equatorial Rh—X bond distances increase by ~ 0.14 Å upon substitution of chloride by bromide and ~0.31 Å when chloride is replaced with iodide. These figures are consistent with the larger atomic radii of bromine and iodine atoms, (r (Cl) in Cl₂ = 0.994 Å, r (Br) in Br₂ = 1.141 Å, rI in $I_2 = 1.333$ Å) $\Delta r = 0.147$ Å and 0.339Å between chlorine and bromine and chlorine and iodine, respectively. The Rh—Rh separation of a given complex increases when X = Br and again when X = I. These trends have been observed for other binuclear compounds including Rh₂X₆(dppm)₂ where the Rh—Rh separation increases by 0.102 Å and the Rh—X bond length increases by 0.131 Å upon substitution of bromide for chloride.²²

Figure 21. ORTEP drawing and numbering scheme of $Rh_2[\mu-CH_3N(PF_2)_2]_3[(PF_2)NCH_3(F_2P)]Br_2$ with 50% probability ellipsoids.

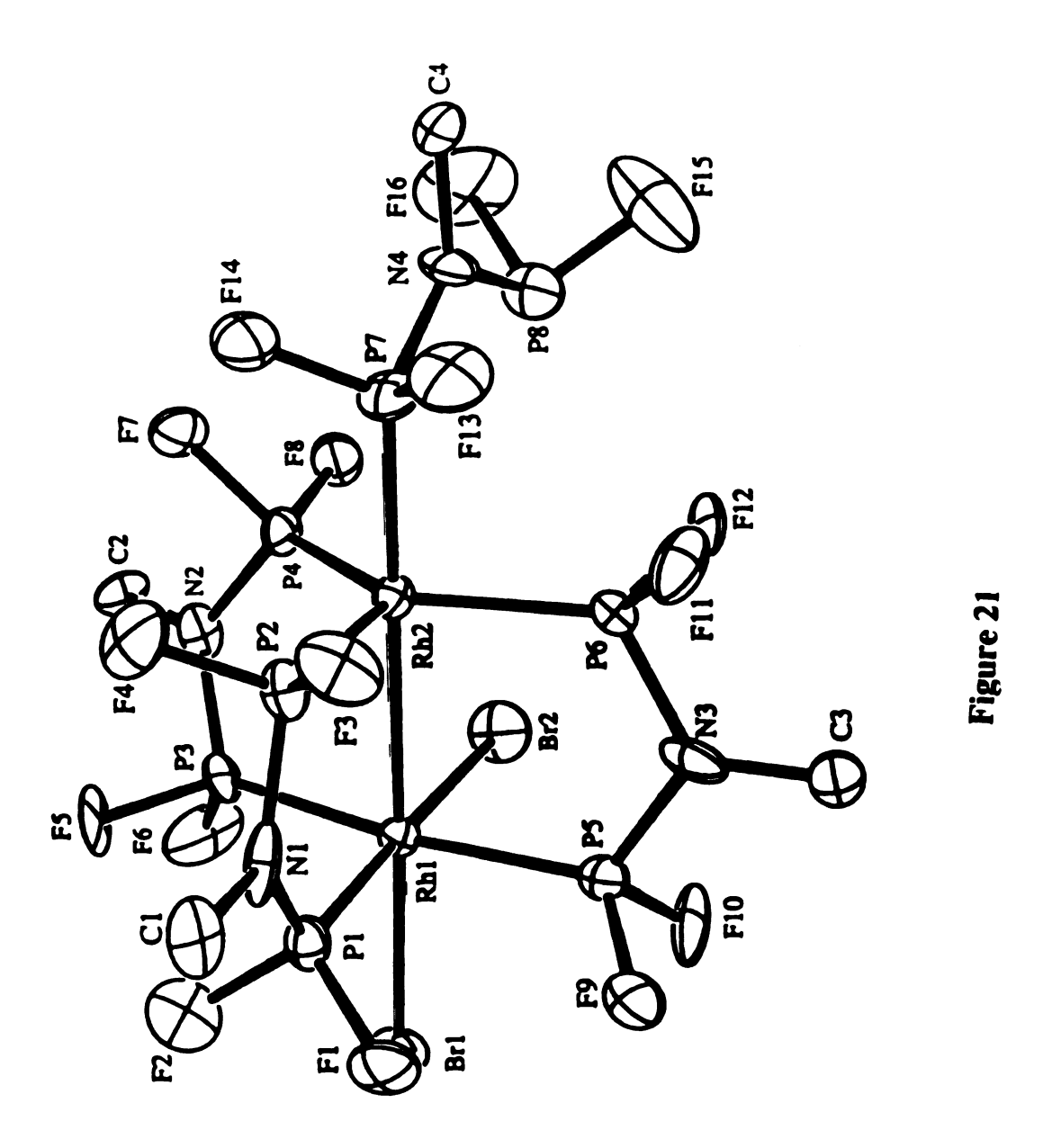


Figure 22. Ortep view of Rh₂[CH₃N(PF₂)₂]₃Br₄ showing the numbering scheme. Thermal parameters are shown at the 50 % level.

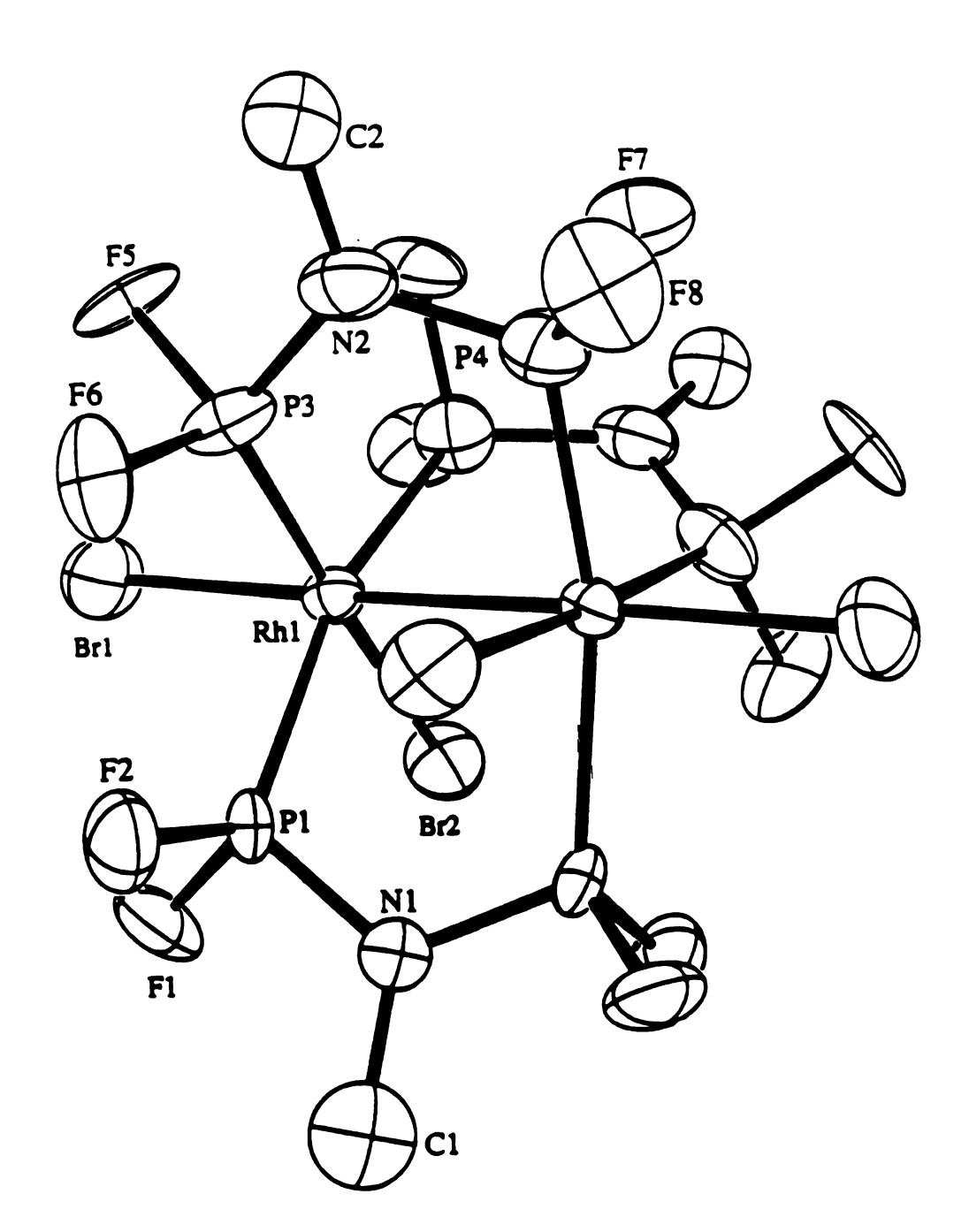


Figure 22

Figure 23. ORTEP drawing and numbering scheme for $Rh_2[\mu-CH_3N(PF_2)_2]_3[(PF_2)NCH_3(F_2P)]I_2$ showing 50% probability ellipsoids.

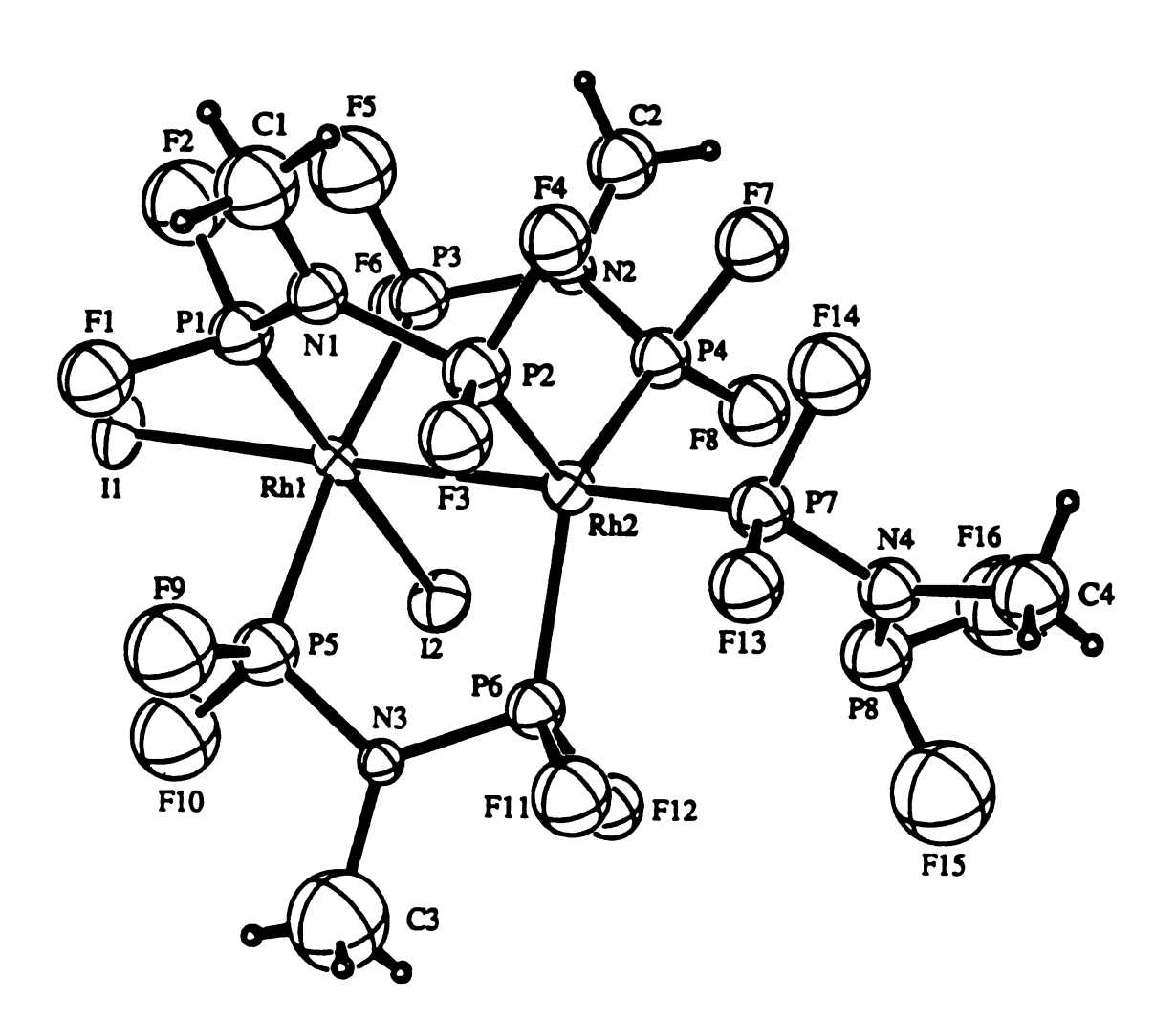


Figure 23

Table 1 Crystallographic Data for Rh2|CII3N(PF2)2|3|(PF2)CH3N(F2P)|Br2 (1), Rh2|CH3N(PF2)2|3Br4 (2) and Rh2|CH3N(PF2)2|3|(PF2)CH3N(F2P)|I2 (3)

	_	2	33
formula formula weight Space group cell parameters	Rl ₁₂ F ₁₆ Br ₂ P ₈ N ₄ C ₄ H ₁₂ 1033.55 P2 ₁ 2 ₁ 2 ₁	Rh2F12Br4P6N3C3H9 1026.37 C2/c	Rh2F1612P8N4C4H12 1127.55 P212121
а, С, Ъ, А	13.868(7) 16.090(5) 11.614(5)	14.62(6) 12.20(2) 14.33(1)	14.28(2) 16.41(2)
α, deg β, deg γ, deg	06 06 06	106.0(2)	11.753(8) 90 90
, A3 Z 1	2591(3) 4 2.649	2457(11) 4	90 2754(8) 4
μ(Mo Kα), cm ⁻¹ radiation (λ, Å) temp. °C	49.17 0.71069	2.775 82.44 0.71069	2.719 39.72 0.71069
ļ	-90 0.052 0.062	23 0.058 0.056	23 0.059 0.069

^a $R = \Sigma ||F_0| - |F_0| \Sigma |F_0|$. ^b $R_w = [\Sigma w(|F_0| - |F_0|)^2 / \Sigma w |F_0|^2]^{1/2}$; $w = 1/s^2 (|F_0|)$.

Table 2 Atomic Positional and Isotropic Displacement Parameters (Å2) for (1)

Atom	x	у	Z	B/Å ²
Br(1)	0.4995(2)	0.5754(1)	0.2384(2)	2.7(1)
Br(2)	0.3205(2)	0.6729(2)	0.4319(2)	3.2(1)
P(1)	0.6366(5)	0.5686(4)	0.4639(5)	2.0(3)
P(2)	0.6346(5)	0.6027(5)	0.7041(6)	2.1(3)
P(3)	0.4196(5)	0.4968(4)	0.5033(6)	2.2(3)
P(4)	0.3594(5)	0.5747(4)	0.7028(6)	1.8(3)
P(5)	0.5358(5)	0.7458(4)	0.4031(5)	2.1(3)
P(6)	0.4960(6)	0.7921(4)	0.6328(4)	2.0(3)
P(7)	0.4835(6)	0.6905(4)	0.8709(5)	2.4(3)
P(8)	0.2962(6)	0.7714(5)	0.8504(6)	3.3(4)
F (1)	0.712(1)	0.608(1)	0.383(1)	3.2(7)
F(2)	0.649(1)	0.479(1)	0.425(1)	4.0(9)
F(3)	0.713(1)	0.655(1)	0.760(1)	3.8(8)
F(4)	0.648(1)	0.525(1)	0.786(1)	4(1)
F(5)	0.485(1)	0.4195(8)	0.526(2)	6(1)
F(6)	0.365(1)	0.456(1)	0.410(1)	5(1)
F(7)	0.353(1)	0.5251(9)	0.818(1)	2.8(7)
F(8)	0.255(1)	0.6063(9)	0.709(1)	3.0(7)
F(9)	0.638(1)	0.758(1)	0.350(1)	4.2(9)
F(10)	0.482(1)	0.7857(7)	0.301(1)	4.0(8)

Table 2 (cont'd)

Atom	х	у	Z	B/Å2
F11	0.566(1)	0.846(1)	0.705(1)	3.5(7)
F12	0.408(1)	0.8540(9)	0.648(1)	5(1)
F13	0.571(1)	0.743(1)	0.917(1)	4.0(9)
F14	0.498(1)	0.6147(9)	0.954(1)	4.0(7)
F15	0.284(2)	0.861(1)	0.902(2)	7(1)
F16	0.214(1)	0.736(1)	0.928(2)	7(1)
N1	0.694(2)	0.569(1)	0.586(2)	3(10
N2	0.343(1)	0.496(1)	0.612(2)	2(1)
N3	0.533(2)	0.821(1)	0.500(2)	3(1)
N4	0.391(2)	0.736(1)	0.933(2)	3(1)
C1	0.796(2)	0.540(2)	0.598(2)	3(1)
C2	0.271(2)	0.433(2)	0.629(2)	2(1)
C3	0.557(2)	0.907(2)	0.470(2)	2.5(5)
C4	0.395(2)	0.753(2)	1.059(2)	4(1)

Table 3 Atomic Positional and Isotropic Displacement Parameters (Å²)for (2)

atom	x	у	Z	B/Å ²
Rh(1)	0.0529(02)	0.2343(02)	0.1841(02)	2.2(1)
Br (1)	0.1345(03)	0.2348(03)	0.0476(02)	5.0(2)
Br(2)	0.1992(02)	0.1495(03)	0.2966(02)	4.1(2)
P(1)	0.0105(06)	0.0558(07)	0.1549(05)	2.8(4)
P(3)	-0.0665(06)	0.3196(07)	0.0872(07)	3.9(4)
P(4)	-0.1270(06)	0.3859(07)	0.2481(07)	3.9(4)
F(1)	0.0821(12)	-0.0160(13)	0.1205(12)	4.7(9)
F(2)	-0.0790(12)	0.0222(13)	0.0726(11)	5(1)
F(5)	-0.0415(12)	0.4007(13)	0.0156	5(1)
F(6)	-0.1931(11)	0.249(02)	0.0115(11)	54(9)
F(7)	-0.0884(11)	0.4982(13)	0.2971	4.5(9)
F(8)	-0.2307(11)	0.4000(01)	0.252(01)	6(1)
N(1)	0	-0.014(03)	1/4	2.9(7)
N(2)	-0.134(02)	0.406(02)	0.132(02)	4(1)
C(1)	0	-0.138(04)	1/4	6(1)
C(2)	-0.200(02)	0.489(03)	0.075(02)	4.7(7)

Table 3 Atomic Positional and Isotropic Displacement Parameters (Å²)for (2)

atom	x	v	Z	B/Å ²
atom		y		
Rh (1)	0.0529(02)	0.2343(02)	0.1841(02)	2.2(1)
Br (1)	0.1345(03)	0.2348(03)	0.0476(02)	5.0(2)
Br(2)	0.1992(02)	0.1495(03)	0.2966(02)	4.1(2)
P(1)	0.0105(06)	0.0558(07)	0.1549(05)	2.8(4)
P(3)	-0.0665(06)	0.3196(07)	0.0872(07)	3.9(4)
P(4)	-0.1270(06)	0.3859(07)	0.2481(07)	3.9(4)
F(1)	0.0821(12)	-0.0160(13)	0.1205(12)	4.7(9)
F(2)	-0.0790(12)	0.0222(13)	0.0726(11)	5(1)
F(5)	-0.0415(12)	0.4007(13)	0.0156	5(1)
F(6)	-0.1931(11)	0.249(02)	0.0115(11)	54(9)
F(7)	-0.0884(11)	0.4982(13)	0.2971	4.5(9)
F(8)	-0.2307(11)	0.4000(01)	0.252(01)	6(1)
N(1)	0	-0.014(03)	1/4	2.9(7)
N(2)	-0.134(02)	0.406(02)	0.132(02)	4(1)
C(1)	0	-0.138(04)	1/4	6(1)
C(2)	-0.200(02)	0.489(03)	0.075(02)	4.7(7)

Table 4 Atomic Positional and Isotropic Displacement (Å2) Parameters for (3)

atom	x	у	Z	B/Å ²
I(1)	-0.0079(4)	0.9214(3)	0.7654(3)	3.8(3)
I (2)	0.1861(3)	0.8199(3)	0.5796(4)	3.3(2)
Rh(1)	0.0106(4)	0.8780(3)	0.5416(4)	2.0(3)
Rh(2)	0.0206(4)	0.8371(3)	0.3087(3)	2.1(3)
P(1)	-0.133(1)	0.924(1)	0.518(1)	3.0(4)
P(2)	-0.117(1)	0.891(1)	0.282(1)	3.2(5)
P(3)	-0.033(1)	0.751(1)	0.589(1)	3.1(4)
P(4)	0.015(1)	0.704(1)	0.364(1)	3.0(4)
P(5)	0.080(1)	0.996(1)	0.498(2)	3.5(4)
P(6)	0.143(1)	0.920(1)	0.296(1)	2.7(4)
P(7)	0.029(1)	0.804(1)	0.130(1)	3.0(4)
P(8)	0.214(1)	0.730(1)	0.154(2)	4.1(5)
F(1)	-0.154(2)	1.014(2)	0.555(3)	4(1)
F(2)	-0.207(3)	0.890(2)	0.600(3)	^(1)
F(3)	-0.132(2)	0.966(2)	0.197(3)	3.6(9)
F(4)	-0.192(2)	0.839(2)	0.224(2)	3.4(8)
F(5)	-0.138(3)	0.748(3)	0.629(3)	7(1)
F(6)	0.012(3)	0.714(2)	0.691(2)	3.6(8)
F(7)	-0.055(2)	0.651(2)	0.291(3)	4.3(9)
F(8)	0.101(3)	0.646(2)	0.357(3)	4(1)
F(9)	0.014(3)	1.071(2)	0.469(3)	6(1)
F(10)	0.144(3)	0.651(2)	0.595(4)	7(1)

Table 4 (cont'd)

atom	x	у	Z	B/Å ²
F(11)	0.147(3)	0.975(2)	0.183(3)	5(1)
F(12)	0.246(2)	0.895(2)	0.283(3)	3.4(8)
F(13)	0.019(3)	0.880(2)	0.050(2)	3.7(7)
F(14)	-0.053(3)	0.755(2)	0.081(3)	5(1)
F(15)	0.294(4)	0.760(3)	0.073(4)	9(1)
F(16)	0.227(3)	0.644(3)	0.107(4)	8(1)
N (1)	-0.186(4)	0.926(3)	0.389(4)	3(1)
N(2)	-0.023(3)	0.678(3)	0.493(3)	2(1)
N(3)	0.150(3)	0.996(3)	0.388(3)	2(1)
N(4)	0.119(5)	0.759(3)	0.073(4)	3(1)
C (1)	-0.281(5)	0.945(4)	0.381(6)	5(2)
C(2)	-0.055(5)	0.591(4)	0.526(5)	4(2)
C(3)	0.229(6)	1.068(5)	0.380(7)	8(3)
C(4)	0.119(5)	0.731(4)	-0.047(6)	4(2)

Table 5 Selected Bond Distances (Å) and Bond Angles (deg) for (1)

	Bond Distances		
atom 1	atom 2	distance	
Rh(1)	Rh(2)	2.798(2)	
Rh(1)	Br(1)	2.579(3)	
Rh(1)	Br (2)	2.524(4)	
Rh(1)	P(1)	2.185(7)	
Rh(1)	P(3)	2.241(7)	
Rh (1)	P(5)	2.247(7)	
Rh(2)	P(2)	2.229(7)	
Rh(2)	P(4)	2.246(7)	
Rh(2)	P(6)	2.243(6)	
Rh(2)	P(7)	2.203(6)	

Bond	Angles
------	---------------

atom 1	atom 2	atom 3	angle
Rh(2)	Rh (1)	Br(1)	177.1(1)
Rh(2)	Rh (1)	Br(2)	90.0(1)
Rh(2)	Rh (1)	P(1)	91.9(2)
Rh(2)	Rh(1)	P(3)	87.0(2)
Rh(2)	Rh(1)	P(5)	91.7(2)
Br(1)	Rh(1)	Br(2)	92.9(1)
Br(1)	Rh (1)	P(1)	85.2(2)
Br (1)	Rh (1)	P(3)	93.1(2)
Br(1)	Rh(1)	P(5)	88.7(2)
Br(2)	Rh(1)	P(1)	178.0(2)
Br(2)	Rh(1)	P(3)	86.0(2)
Br(2)	Rh (1)	P(5)	84.9(2)
P(1)	Rh(1)	P(3)	94.8(3)
P(1)	Rh(1)	P(5)	94.4(3)
P(3)	Rh(1)	P(5)	170.8(3)

Table 5 (cont.)

Bond	Angles	(cont.)	
tom 2		atom 3	

atom 1	atom 2	atom 3	angle
Rh(1)	Rh(2)	P(2)	89.2(2)
Rh(1)	Rh(2)	P(4)	86.8(2)
Rh(1)	Rh(2)	P(6)	87.6(1)
Rh(1)	Rh(2)	P(7)	178.7(2)
P(2)	Rh(2)	P(4)	118.4(3)
P(2)	Rh(2)	P(6)	111.5(3)
P(2)	Rh(2)	P(7)	91.9(3)
P(4)	Rh(2)	P(6)	129.6(3)
P(4)	Rh(2)	P(7)	92.0(3)
P(6)	Rh(2)	P(7)	92.7(2)

Torsional Angles

atom 1	atom 2	atom 3	atom 4	angle
P(1)	Rh(1)	Rh(2)	P(2)	-3.3(3)
P(3)	Rh(1)	Rh(2)	P(4)	-27.2(3)
P(5)	Rh(1)	Rh(2)	P(6)	13.8(3)

Table 6 Selected Bond Distances (Å) and Bond Angles (deg) for (2)

	Bond Distances	
atom 1	atom 2	distance
Rh(1)	Rh(1)'	2.750(8)
Rh(1)	Br(1)	2.555(6)
Rh(1)	Br(2)	2.519(9)
Rh(1)	P(1)	2.271(9)
Rh(1)	P(3)	2.17(1)
Rh(1)	P(4)	2.23(1)

Bon	d	An	øl	es
DVII	u	4 7 11	6,	LJ

atom 1	atom 2	atom 3	angle
Rh(1)	Rh(1)'	Br(1)	173.9(2)
Rh(1)	Rh (1)'	Br(2)	95.7(3)
Rh (1)	Rh (1)'	P(1)	87.1(2)
Rh (1)	Rh(1)'	P(3)	86.2(3)
Rh (1)	Rh(1)'	P(4)	89.9(3)
Br(1)	Rh (1)	Br(2)	89.9(3)
Br(1)	Rh (1)	P(1)	91.3(2)
Br(1)	Rh (1)	P(3)	88.4(3)
Br(1)	Rh (1)	P(4)	93.4(3)
Br(2)	Rh (1)	P(1)	82.2(3)
Br(2)	Rh (1)	P(3)	175.3(3)
Br(2)	Rh (1)	P(4)	80.6(3)
P(1)	Rh (1)	P(3)	102.2(4)
P(1)	Rh (1)	P(4)	162.2(3)
P(3)	Rh (1)	P(4)	95.2(4)

Table 6 (cont.)

Torsional Angles				
atom 1	atom 2	atom 3	atom 4	angle
P(1)	Rh(1)	Rh(1)'	P(1)'	32.5(4)
P(3)	Rh(1)	Rh(1)'	P(3)'	-122.6(5)
P(4)	Rh(1)	Rh(1)'	P(4)'	67.7(6)

Table 7 Selected Bond Distances (Å) and Bond Angles (deg) for (3)

	Bond Distances	
atom 1	atom 2	distance
Rh(1)	Rh(2)	2.822(6)
Rh(1)	I (1)	2.737(6)
Rh(1)	I (2)	2.713(8)
Rh(1)	P(1)	2.20(2)
Rh(1)	P(3)	2.24(2)
Rh(1)	P(5)	2.24(2)
Rh(2)	P(2)	2.18(2)
Rh(2)	P(4)	2.27(2)
Rh(2)	P(6)	2.22(2)
Rh(2)	P(7)	2.18(2)

Bond Angles

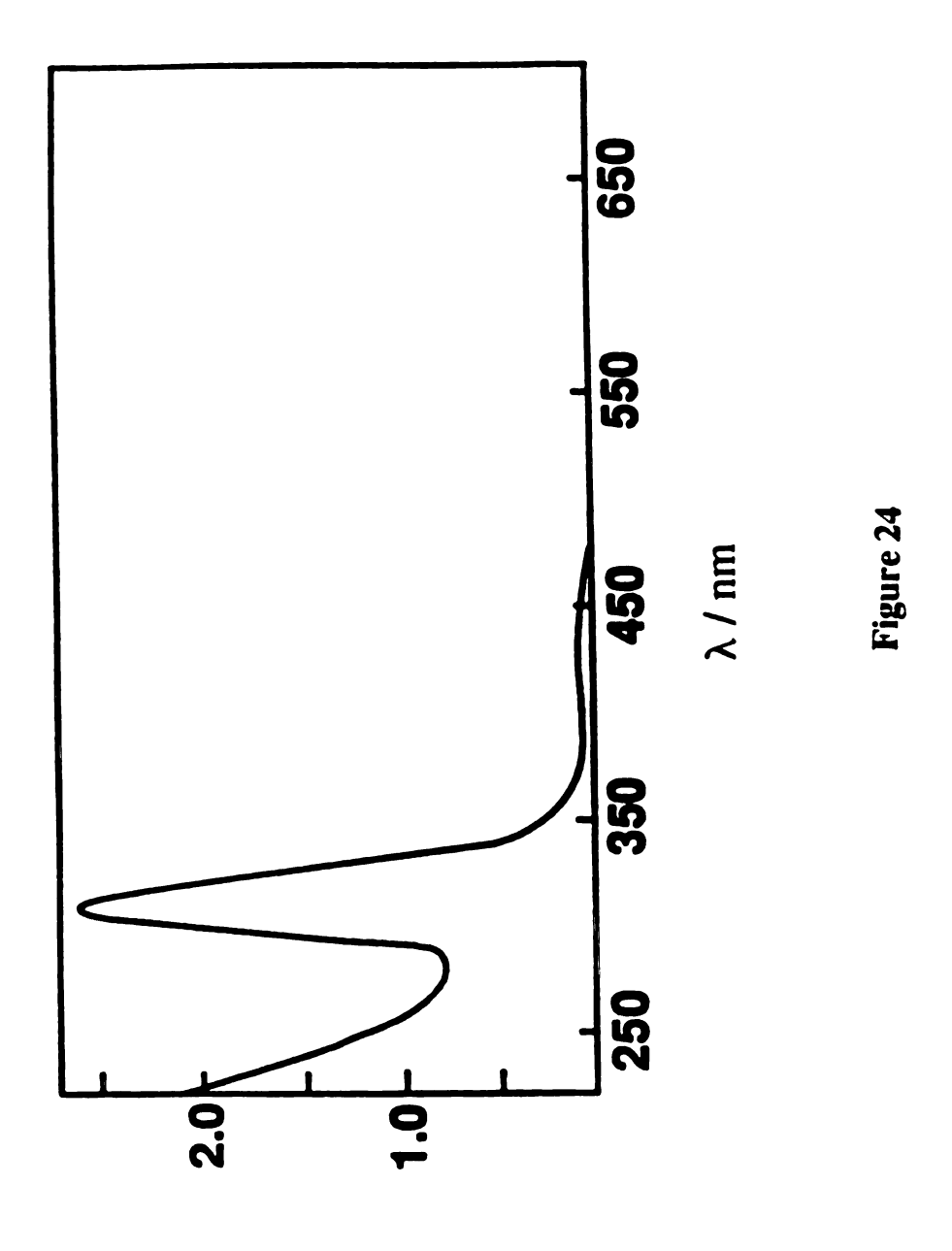
atom 1	atom 2	atom 3	angle
Rh(2)	Rh(1)	I(1)	177.0(3)
Rh(2)	Rh(1)	I (2)	91.0(2)
Rh(2)	Rh(1)	P(1)	90.0(4)
Rh(2)	Rh (1)	P(3)	92.0(5)
Rh(2)	Rh(1)	P(5)	87.7(5)
I(1)	Rh (1)	I (2)	91.9(2)
I(1)	Rh(1)	P(1)	86.6(5)
I(1)	Rh(1)	P(3)	88.5(5)
I(1)	Rh (1)	P(5)	92.3(5)
I(2)	Rh(1)	P(1)	178.2(5)
I(2)	Rh(1)	P(3)	84.0(6)
I(2)	Rh (1)	P(5)	86.2(6)
P(1)	Rh(1)	P(3)	94.9(7)
P(1)	Rh(1)	P(5)	94.9(7)
P(3)	Rh(1)	P(5)	170.1(8)

3. Photophysical Studies

The electronic absorption spectrum of Rh₂[CH₃N(PF₂)₂]₃(PF₃)₂, shown in Figure 24, provides a benchmark for interpreting the electronic absorption spectra of this series of singly bonded metal-metal compounds. The absorption spectrum is typical of M—M compounds with an intense 305 nm band attributable to the allowed $d\sigma \rightarrow \sigma^*$ transition and the less intense band at 440 nm consistent with $d\pi^* \rightarrow d\sigma^*$ promotion. The high optical electronegativity of the terminal PF₃ ligands reduces configurational mixing of the $d\sigma$ and $L\sigma$ orbitals, which is observed when more easily ionizable ligands such as halides or pseudohalides are coordinated axially to a M—M core.³¹ Accordingly, the importance of configurational mixing of the $L\sigma$ and $d\sigma$ orbitals for the dirhodium fluorophosphines is apparent upon comparison of the spectra of Rh₂(0,II)X₂ and Rh₂(II,II)X₄ (X=Cl, Br, I) ²⁵ to that of Rh₂(0,0).

The absorption profiles of the d^7 — d^7 dimers Rh₂(II,II)Cl₄ and Rh₂(II,II)Br₄, shown in Figure 25, are more congested in the uv spectral region. Though the Rh—Rh separation differs by no more than 0.15 Å in this set of complexes, no absorption comparable in energy to the 305 nm $d\sigma \rightarrow \sigma^*$ transition is observed. However, intense transitions to higher and lower energy of the Rh₂(0,0) $d\sigma \rightarrow \sigma^*$ absorption are present ($\lambda_{max}/nm(\epsilon/M^{-1}cm^{-1})$) = 265 (18,700) and 335 (23,000) for Rh₂(II,II)Cl₄; ($\lambda_{max}/nm(\epsilon/M^{-1}cm^{-1})$) = 289 (19,600) and 398 (11,400) for Rh₂(II,II)Br₄. Notably, these transitions exhibit a ~3,500 - 4,500 cm⁻¹ red shift with the replacement of chloride by bromide. In contrast, the energy of the lowest band is much less sensitive to halide substitution ($\lambda_{max}/nm(\epsilon/M^{-1}cm^{-1})$) = 445 (9,430) for Rh₂(II,II)Cl₄; ($\lambda_{max}/nm(\epsilon/M^{-1}cm^{-1})$) = 462(11,700) for Rh₂(II,II)Br₄. The

Figure 24. Electronic absorption spectrum of Rh₂[CH₃N(PF₂)₂]₃(PF₃)₂ taken in CH₂Cl₂ at room temperature.



 $\epsilon \setminus 10^4 \, \mathrm{M}^{-1} \, \mathrm{cm}^{-1}$

Figure 25. Electronic absorption spectra of Rh₂[CH₃N(PF₂)₂]₃Cl₄ (—) and Rh₂[CH₃N(PF₂)₂]₃Br₄ (---) dissolved in CH₂Cl₂ at room temperature.

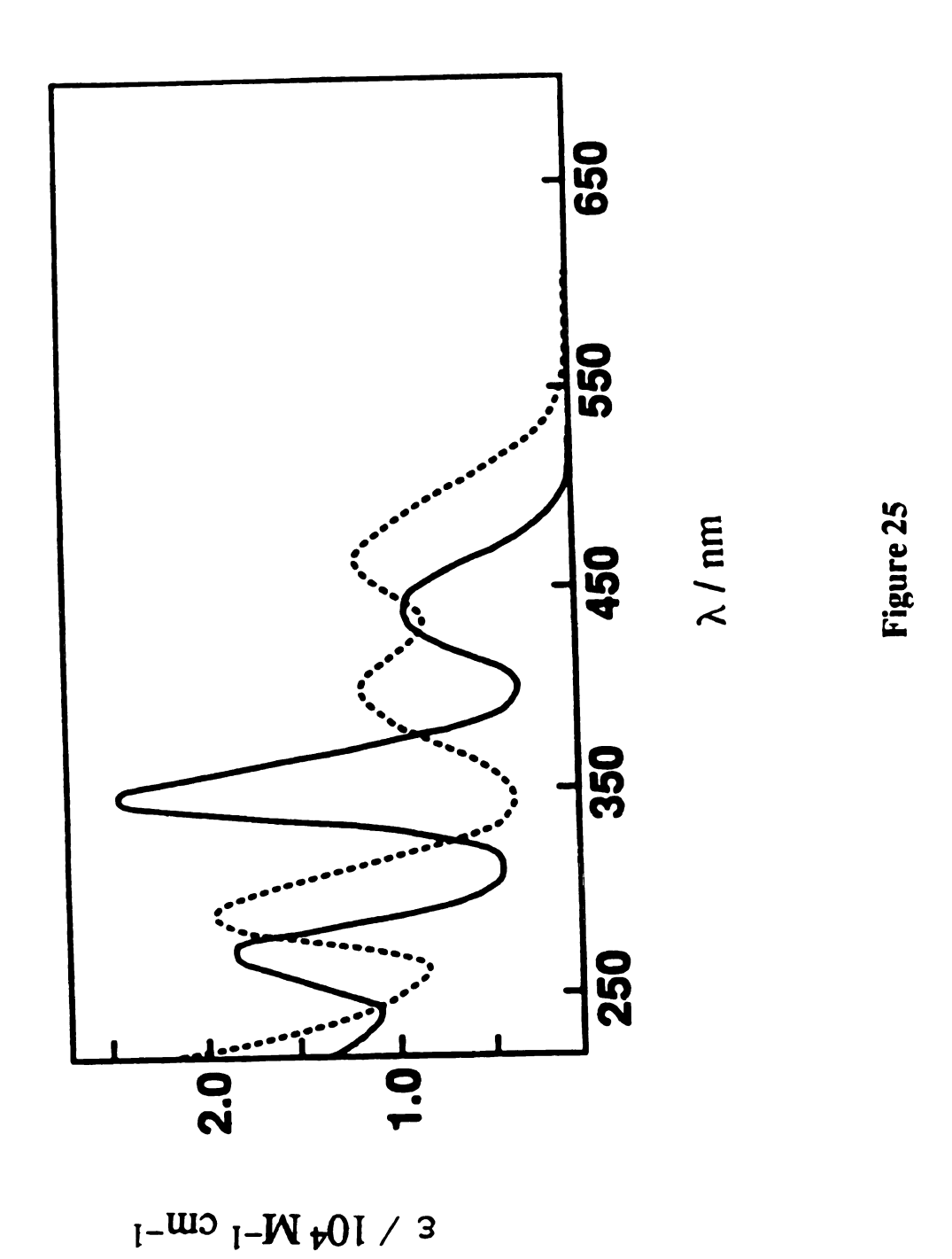
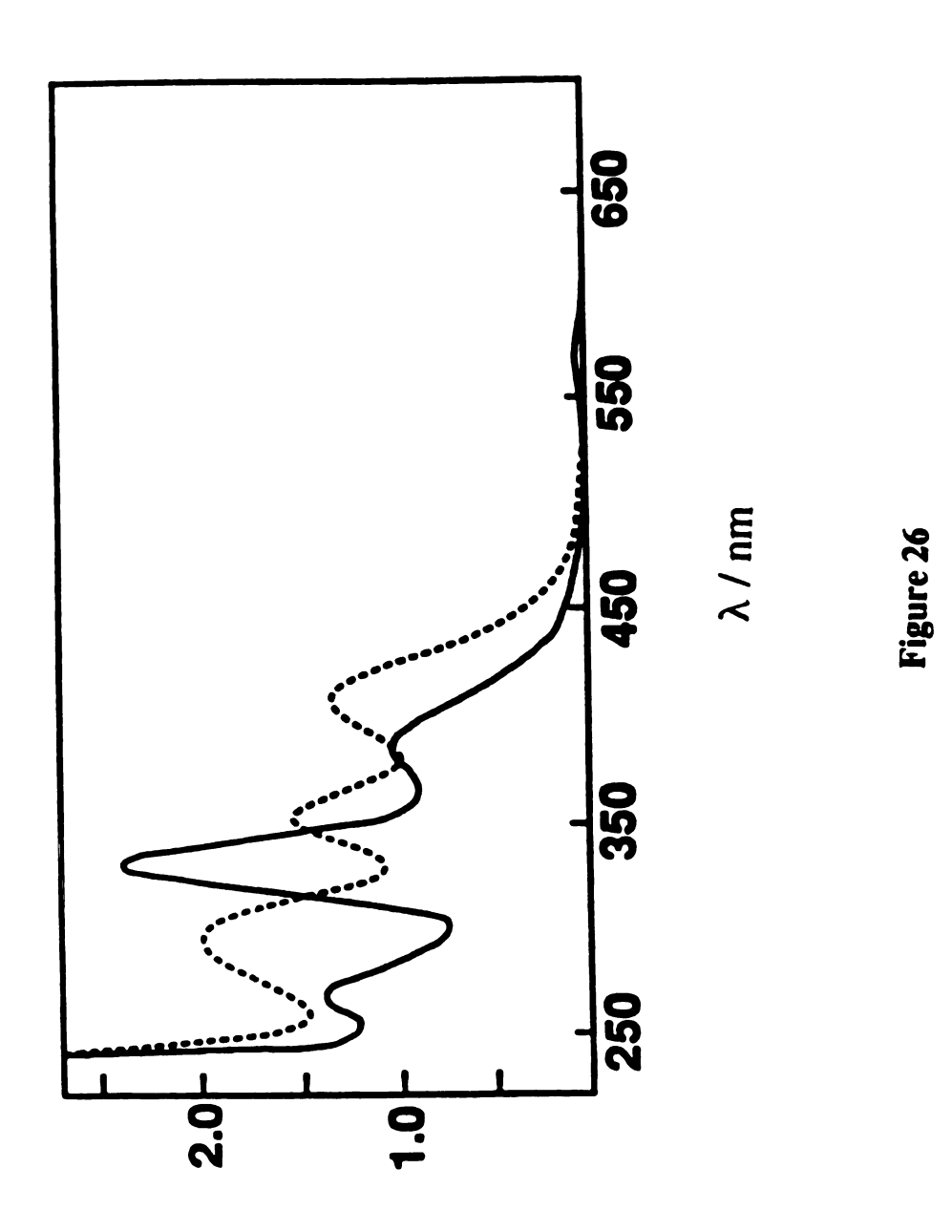


Figure 26. Electronic absorption spectra of $Rh_2[CH_3N(PF_2)_2]_3(PF_3)Cl_2$ (—) and $Rh_2[\mu\text{-}CH_3N(PF_2)_2]_3[(PF_2)NCH_3(F_2P)]Br_2$ (---) dissolved in CH_2Cl_2 at room temperature.

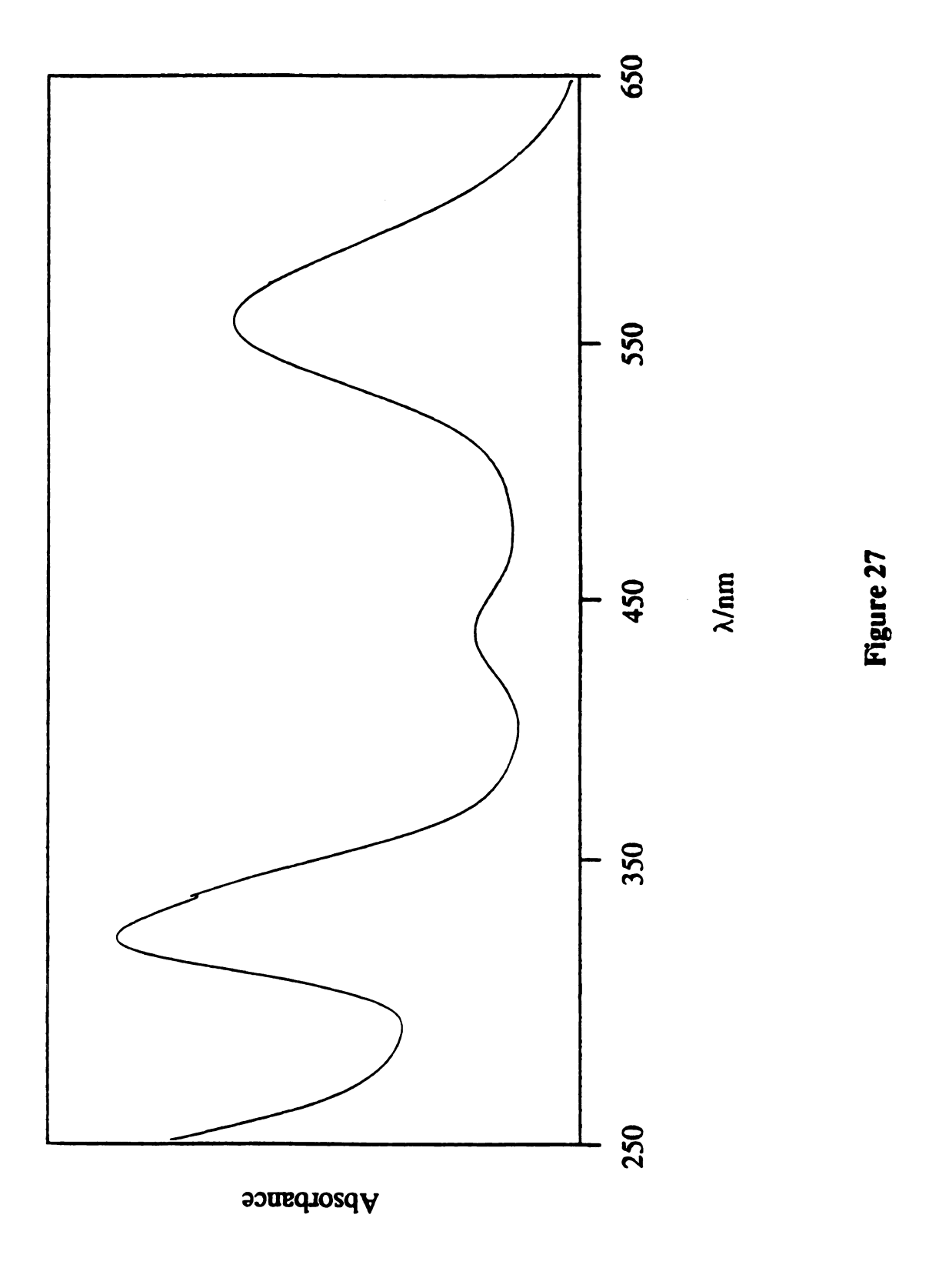


 $\epsilon \setminus 10^4 \, \mathrm{M}^{-1} \, \mathrm{cm}^{-1}$

energy shift on replacing chloride by bromide is approximately 1,000 cm⁻¹ This trend is also observed in the absorption spectra of the Rh₂(0,II)X₂ compounds shown in Figure 26. Absorption profiles show bands in energy regions similar to Rh₂(II,II)X₄ and a red shift is observed upon bromide substitution. Figures 27 is the electronic absorption spectrum of the complex Rh₂(II,II)I₄. Each peak shows a marked red shift from it's chloride counterpart and again from the bromide analog. Additionally, as previously encountered, the lower energy band shows less of a halide dependence than the two bands to higher energy, red shifting 4,400 cm⁻¹ as compared to 7,600 cm⁻¹ and 6,000 cm⁻¹ red shifts for the other bands on replacement of chloride with iodide. A similar situation is observed for the diiodide complex. This result is not surprising in view of the similarities of the frontier molecular orbitals of the d⁷—d⁷ and d⁹—d⁹ dirhodium compounds.

These spectral trends of the dirhodium fluorophosphine series are comparable to those of the d^7 — d^7 Rh₂TMB₄L₂n+ compounds (TMB = 2,5-dimethyl-2,5-diisocyanohexane); L = H₂O, CH₃CN (n = 4); L = Cl, Br (n = 2). In the cases of L= H₂O or CH₃CN, a single intense absorption is observed at 308 nm and assigned to $d\sigma \rightarrow d\sigma^*$. The considerable red shift of the $d\sigma \rightarrow d\sigma^*$ transition upon substitution of L by axial chloride and further red shift with bromide (~2200 cm⁻¹) is attributed to extensive mixing of the metal $d\sigma$ orbital with the axial (X) σ orbitals of the halide substituted compounds. As expected from a configurational interaction scheme, the ligand-to-metal charge transfer transition, (X) $\sigma \rightarrow d\sigma^*$, appears to higher energy of the $d\sigma \rightarrow d\sigma^*$ transition. The lowest energy $d\pi \rightarrow d\sigma^*$ transition shows only a moderate halide dependence, red shifting less along a halide series.

Figure 27. Electronic absorption spectrum of Rh₂[CH₃N(PF₂)₂]₃I₄ dissolved in CH₂Cl₂ at room temperature.



Despite similarities in the energy of the spectral profile of Rh₂(0,II)X₂ and Rh₂(II,II)X₄ to other M—M dimers, there are notable differences. For a typical M—M compound, the spectrum is dominated by the $d\sigma \rightarrow d\sigma^*$ band and the higher energy configurationally mixed $(X)\sigma \to d\sigma^*$ bands exhibit weaker intensity; the weakest transition is usually $d\pi^* \to d\sigma^*$. Conversely, the intensities of the three bands in the absorption manifold of the Rh₂(0,II)X₂ and Rh₂(II,II)X₄ complexes are similar. Undoubtedly this result is due, in large part to the lower molecular symmetry of the dirhodium complexes as compared to the D_{4h} symmetry of the many M—M dimers reported to date. In these lower symmetry molecules, configuration interaction between metal- and ligand-based orbitals will be more extensive. Hence, it is difficult to quantitatively correlate the transitions arising from the $d\pi$ and $d\delta$ orbital symmetries in D_{4h} dimers with those of Rh₂(0,II)X₂ and Rh₂(II,II)X₄ complexes. Thus definitive assignments for the dirhodium fluorophosphine series based on spectral trends of higher symmetry D_{4h} M—M complexes is tenuous. Nonetheless, the band shapes and energy trends of the absorption profile observed in this dirhodium series are consistent with transitions involving the promotion of an electron from configurationally mixed Lo and do orbitals to do* and with a low energy transition manifold of $d\pi^* \rightarrow d\sigma^*$ parentage.

The luminescence of the dirhodium compounds further support an electronic structure dominated by M—M parentage. Table 8 lists the luminescence band energy maxima and emission lifetimes (T = 77 K). The luminescence spectral features are commensurate with the emerging characteristics of $d\sigma^*$ luminescence.³¹ The full-width at half height of the emission bands exhibit a substantial temperature sensitivity, increasing by more than 1,500 cm⁻¹ from 10K to the highest temperatures at which

Table 8 Spectral Information of Bimetallic Rhodium Fluorphosphine Compounds

Compound	dπ*→dσ*	λmax,ab / nm do→do*	σ(X)→dσ*	λmax,em / τ/μs nm	τ/μs
Rh ₂ (0,0)	440	305		805	74
Rh ₂ (II,0)Cl ₂	385	330	270	810	270
	(240)#				
Rh ₂ (II,0)Br ₂	412	354	298	160	190
Rh ₂ (II,0)I ₂	480	432	326		
Rh ₂ (II,II)Cl ₄	445	335	265	820	300
Rh ₂ (II,II)Br ₄	462	395	290	850	278
Rh ₂ (II,II)I ₄	554	434	324		

* Singlet ground state to triplet $d\pi* \rightarrow d\sigma*$ state

emission can be detected for each complex. Moreover, luminescence is not detected from solutions at temperatures equivalent to those at which the crystalline solids emit.

Several data suggest that the state parentage of the $d\sigma^*$ luminescence is the promotion of an electron from the $(d\pi^*, d\sigma^*)$ manifold that is triplet paired. First, the nature of the halide affects the emission energy only marginally across the series, as shown in Figure 28. This energy insensitivity is consistent with the expectation of only small configurational mixing of the $d\sigma^*$ orbital (owing to the large energy gap between (L) σ and $d\sigma^*$ orbitals) and, as observed in the absorption spectra, with the slight energy dependence of the lowest energy absorption manifold. Second, excitation spectra of the dirhodium series suggests that the emission arises from the spin forbidden states of this lowest energy manifold. The excitation spectrum for Rh₂(0,II)Cl₂ in Figure 29 is representative of the dirhodium series.

The luminescence from each of the bimetallic complexes decays monoexponentially. Figures 30 - 32 depict the temperature dependencies of the Rh₂(0,0), Rh₂(0,II)X₂ and Rh₂(II,II)X₄ fluorophosphines respectively. The lifetimes exhibit a temperature independent regime followed by a monotonic decrease with increasing temperatures. The temperature dependence accords well with a two-state Boltzmann distribution in which a state possessing facile decay to ground state is accessed with increasing temperature according to the relation,

$$k_{obs} = \frac{k_0 + k_1 \exp(-\Delta E/k_B T)}{1 + \exp(-\Delta E/k_B T)}$$
 (1)

Calculated rate constants and energy gaps for the dirhodium series are summarized in Table 9 where k₀ and k₁ are decay constants for lower and

Figure 28. Emission spectra of $Rh_2[CH_3N(PF_2)_2]_3(PF_3)_2$ (a), $Rh_2[CH_3N(PF_2)_2]_3Cl_2$ (---) and $Rh_2[μ-CH_3N(PF_2)_2]_3[(PF_2)NCH_3(F_2P)]Br_2$ (—) (b), $Rh_2[CH_3N(PF_2)_2]_3Cl_4$ (---) and $Rh_2[CH_3N(PF_2)_2]_3Br_4$ (—) (c). All obtained at 77 K as the solids.

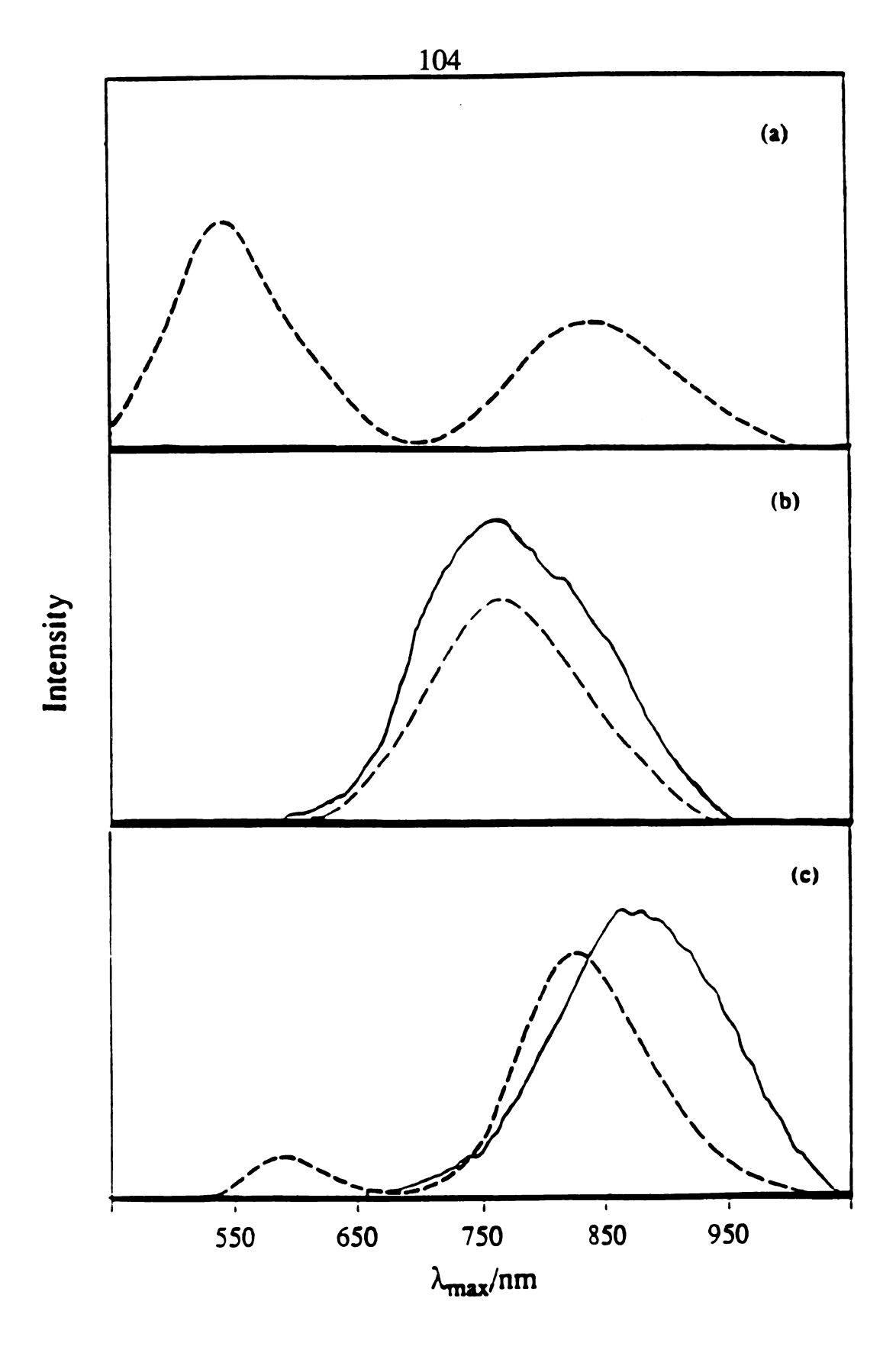
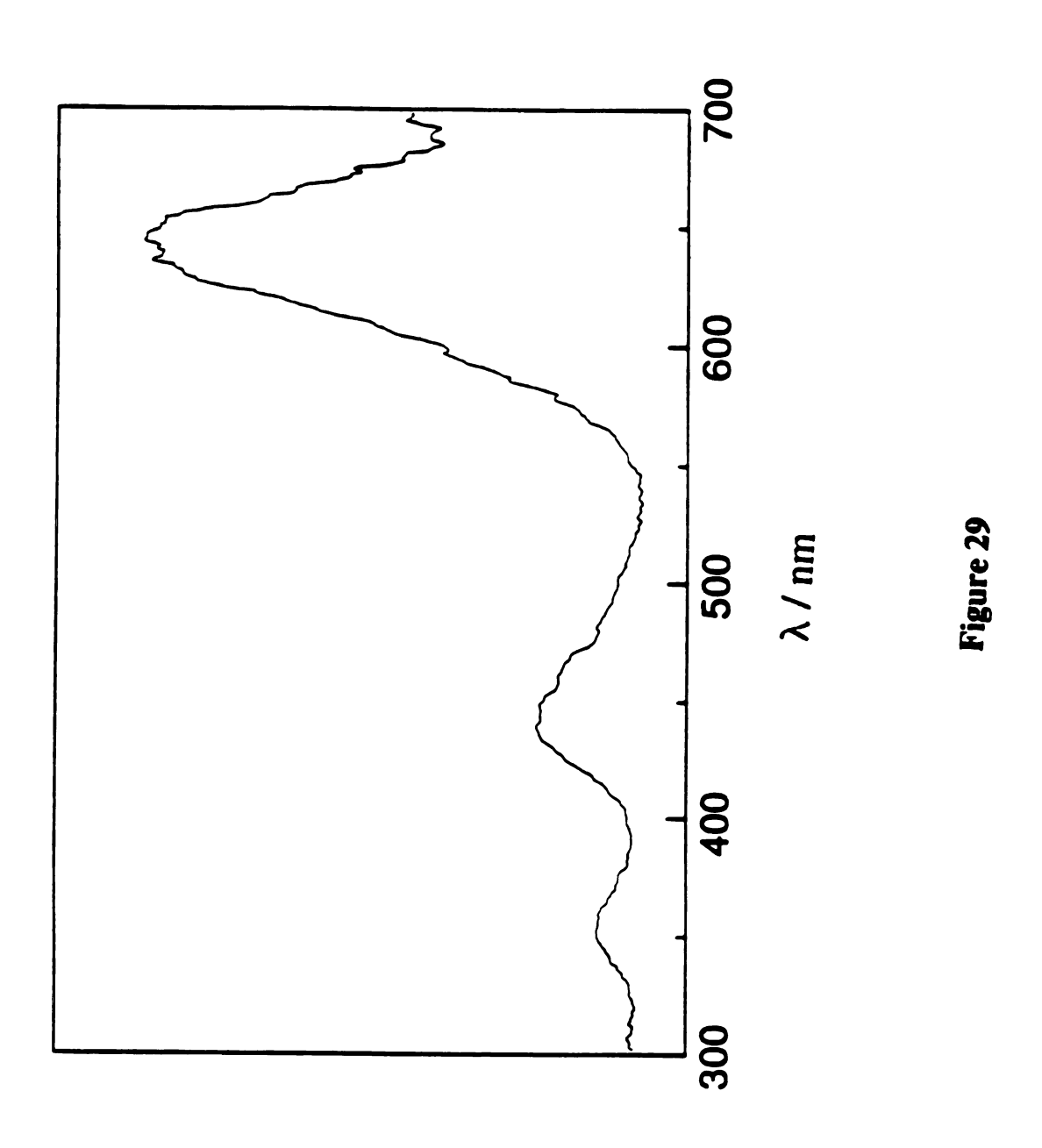


Figure 28

Figure 29. Unpolarized excitation spectrum of crystalline Rh₂[CH₃N(PF₂)₂]₃(PF₃)Cl₂ at 77 K. Emission monitored at 810 nm.



Intensity

Table 9 Calculated Decay Rate Constants and Energy Gaps of Dirhodium Fluorophosphine Complexes

Compound	ΔE/cm ⁻¹	k ₀ / s ⁻¹	k_1/s^{-1}
Rh ₂ (0,0)	369	1.1×10^4	1.2×10^6
Rh ₂ (0,II)Cl ₂	425	3.3×10^3	3.4×10^5
$Rh_2(0,II)Br_2$	596	5.4×10^3	2.1×10^6
Rh ₂ (II,II)Cl ₄	439	3.0×10^3	2.8×10^{5}
Rh ₂ (II,II)Br ₄	895	1.3×10^4	1.6×10^{7}

upper excited states respectively, in thermal equilibrium and ΔE is the energy gap. Best fits to Equation 1 are indicated by the solid lines in Figures 30-32. The experimentally determined decay constant of the higher energy, thermally accessible excited state is 10^2-10^3 greater than that of the lower energy state. Additionally, the calculated energy gap increases with increased halide substitution ($\Delta E(Rh_2(0,0) < \Delta E((Rh_2(0,\Pi)X_2) < \Delta E(Rh_2(\Pi,\Pi)X_4))$). For a given complex, the energy gaps of the bromide derivative is larger than that for it's chloride counterpart, as is the decay constant from the upper excited state ($k_1/k_0 \sim 10^3$ for bromide compounds, as compared to only 10^2 for the chloride compounds).

These trends in Boltzmann behavior and the halide dependence of the photophysical properties have been previously observed for the singly bonded LPt^{III}Pt^{III}L tetraphosphates²⁷, and more recently for LPt^{III}Pt^{III}L tetrasulfates.³² For the former, these trends have been adequately explained by a spin-orbit coupling model where the luminescence originates from a spin-orbit excited state that is predicted to nearly pure triplet in character, with the temperature dependence arising from the thermal population of the $E_u(^3E_u)$ state in the $^3(d\sigma^*d\pi^*)$ manifold acquiring significant singlet character from it's energetically proximate counterpart of singlet parentage $E_u(^1E_u)$. This model is represented in Figure 33, where ΔE is the energy gap between the weakly coupled singlet and triplet of the excited state for the two–state Boltzmann model, where the upper excited state provides a facile pathway to ground state.

For the Rh₂(0,II)X₂ and Rh₂(II,II)X₄ complexes, however descent in symmetry to C_s and C_2 molecular symmetry point groups allows for extensive mixing and the lowest energy excited states do not necessarily remain unique from the ${}^1(d\pi^*d\sigma^*)$ manifold under a spin-orbit coupling

Figure 30. Plot of the temperature dependence of the observed emission decay constant for a solid sample of Rh₂[CH₃N(PF₂)₂]₃(PF₃)₂. The solid line is the fit of the data to Equation 1.

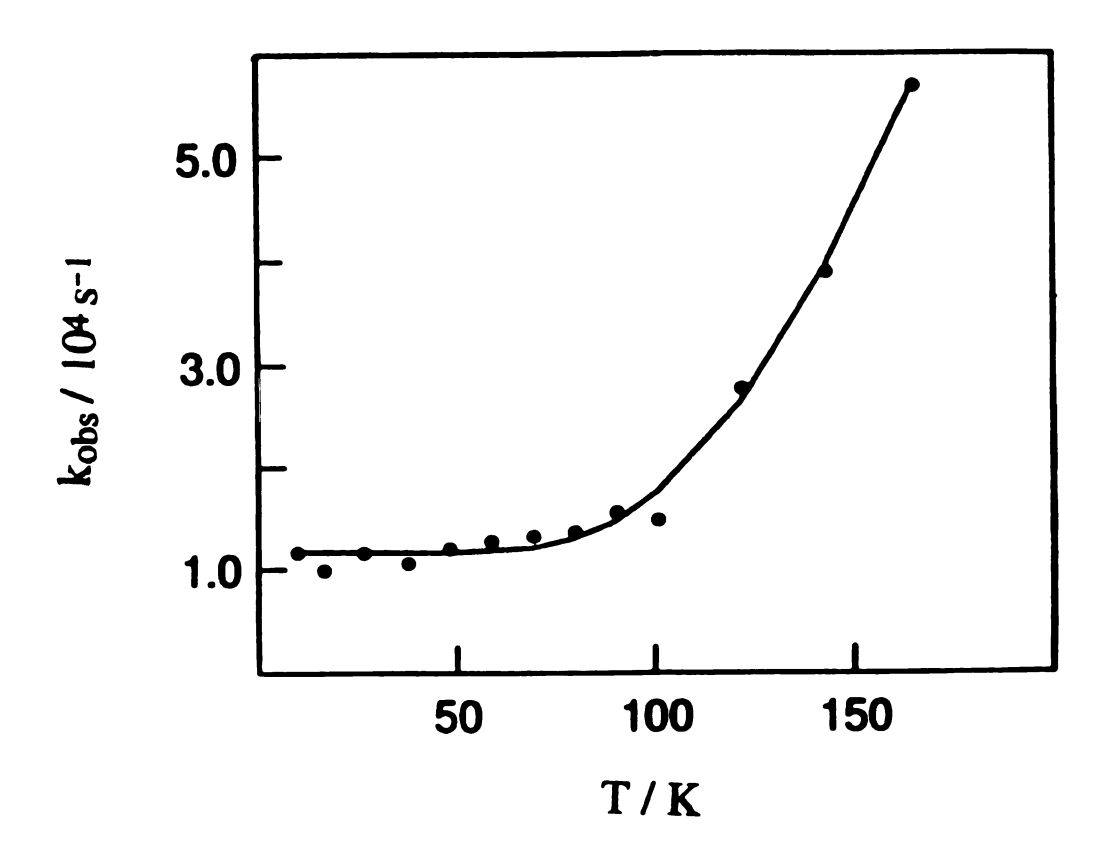


Figure 30

Figure 31. Plot of the temperature dependence of the observed emission decay constant from solid samples of $Rh_2[CH_3N(PF_2)_2]_3(PF_3)Cl_2$ (a) and $Rh_2[\mu-CH_3N(PF_2)_2]_3[(PF_2)NCH_3(F_2P)]Br_2$ (b). The solid line is the fit of the data to Equation 1.

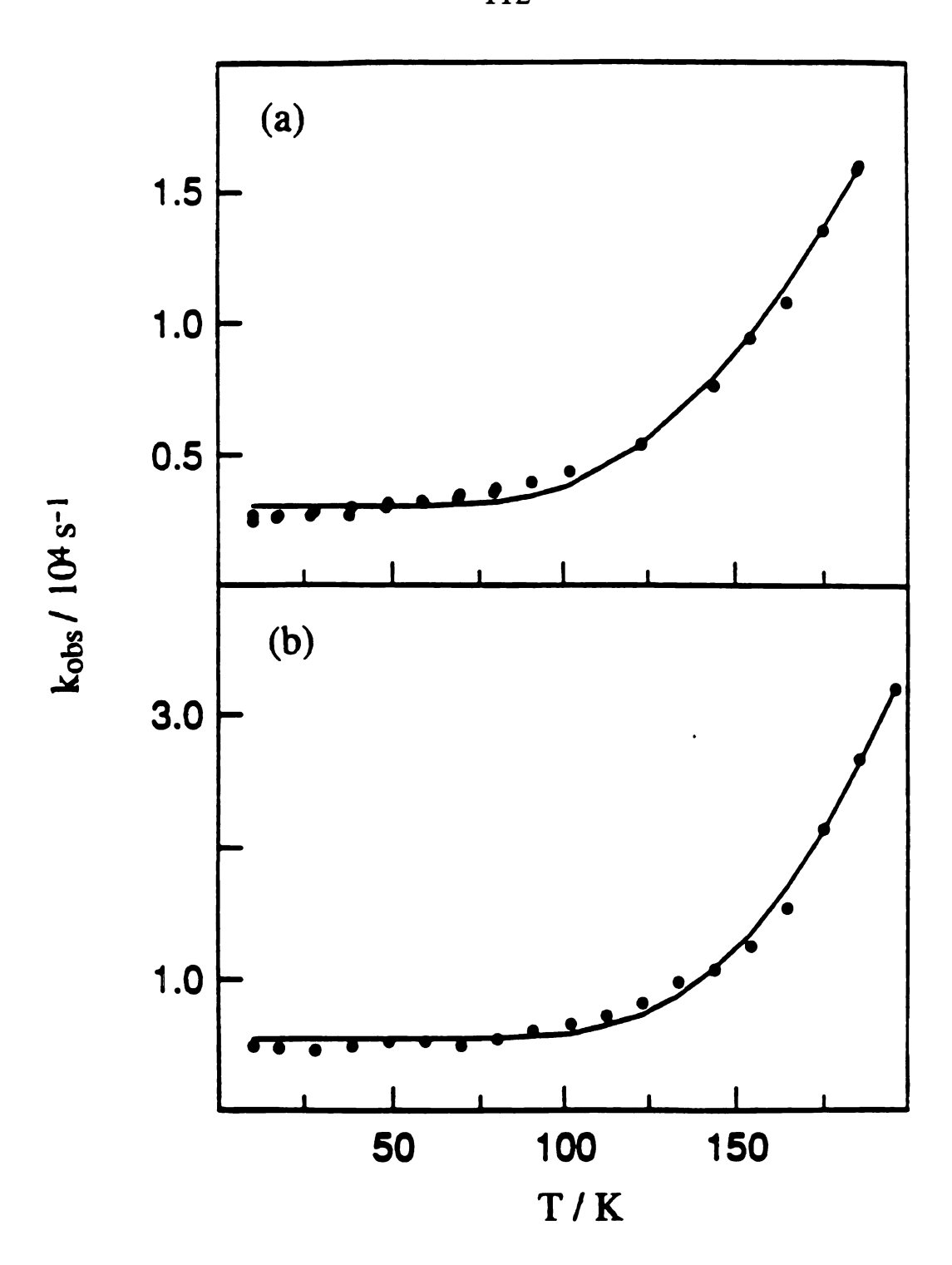


Figure 31

Figure 32. Plot of the temperature dependence of the observed emission decay constant from solid samples of Rh₂[CH₃N(PF₂)₂]₃Cl₄ (a) and Rh₂[CH₃N(PF₂)₂]₃Br₄ (b). The solid line is the fit of the data to Equation 1.

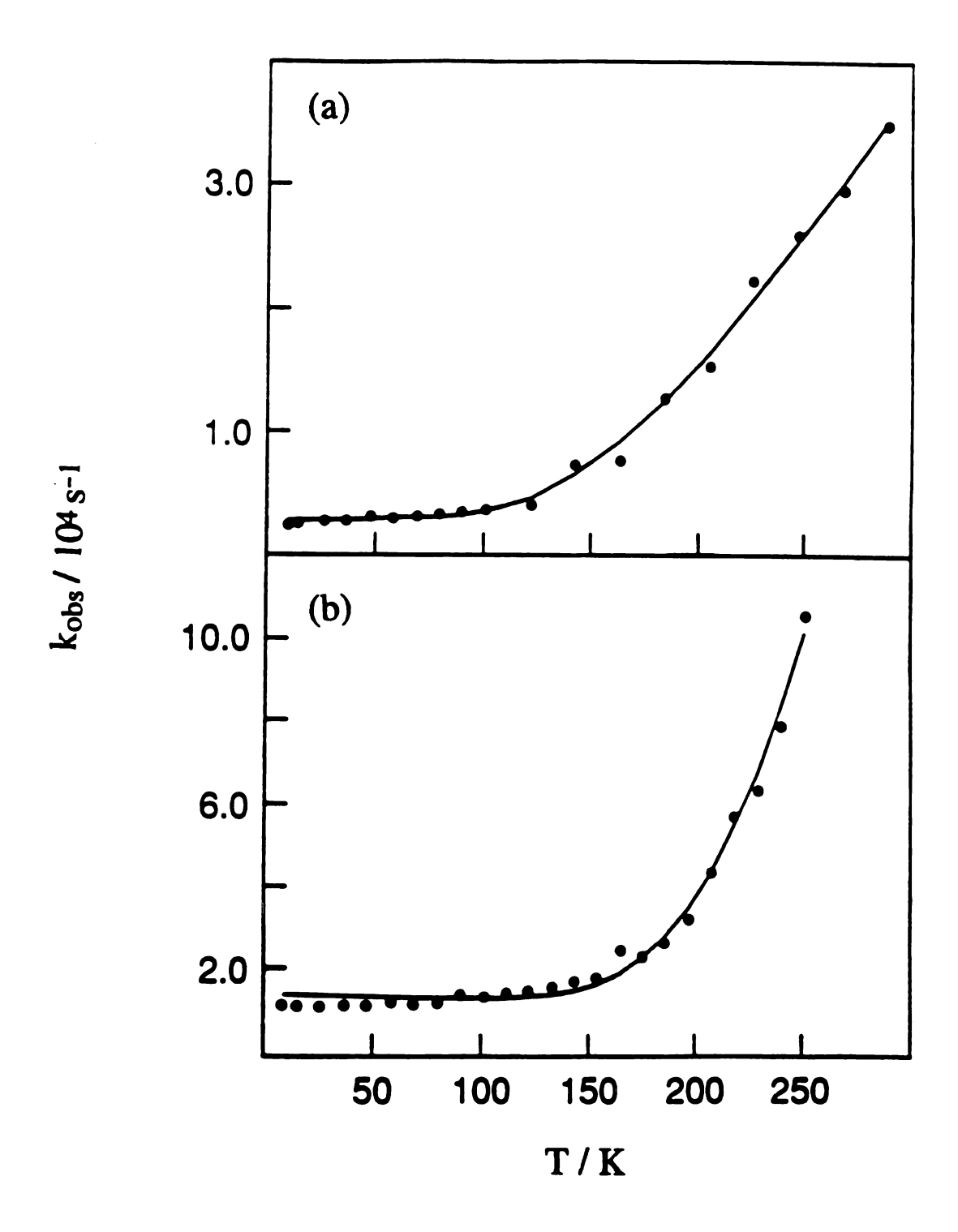
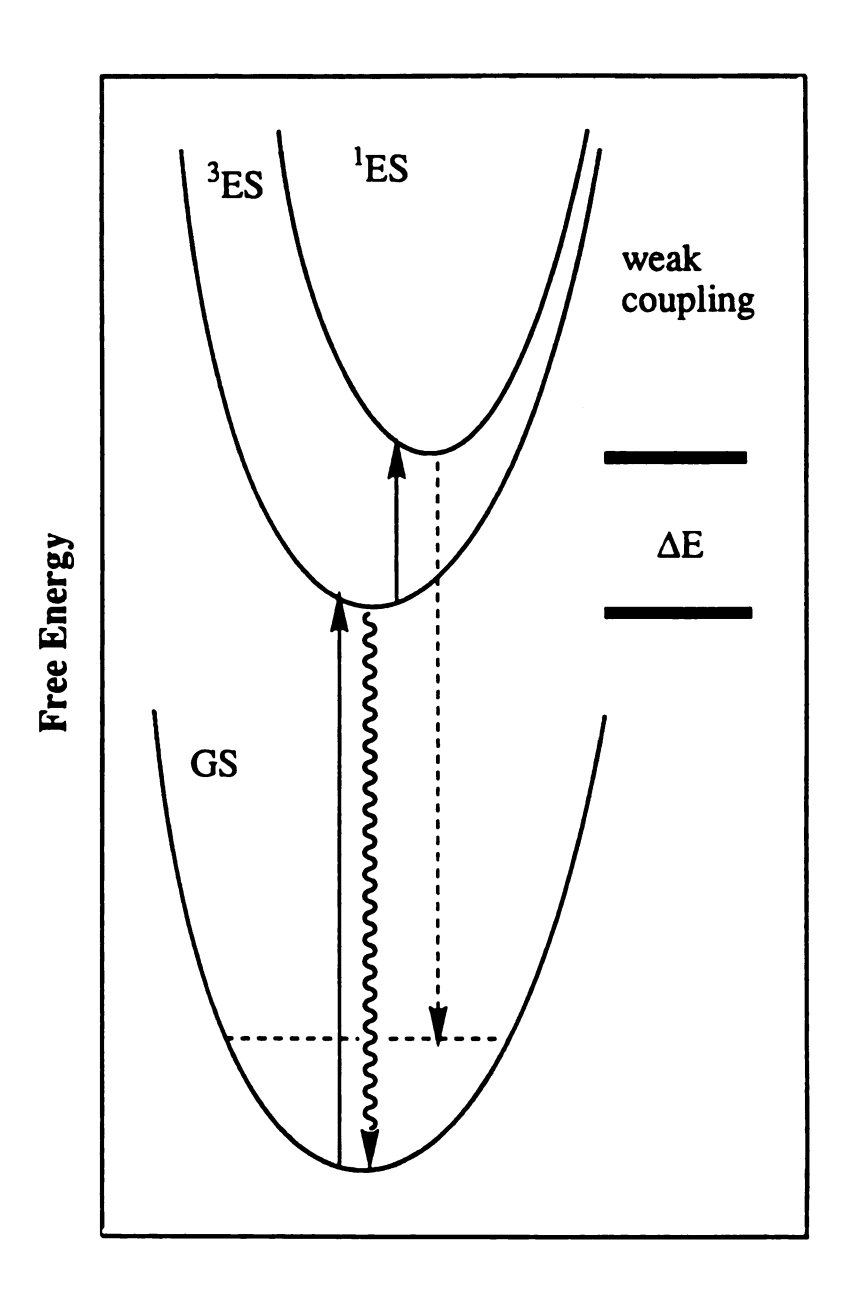


Figure 32

Figure 33. Potential energy diagram showing a singlet excited state in close proximity to a triplet excited state. ΔE is the energy gap between the two states. Radiative decay is represented by zig-zag arrow; non-radiative decay by dotted line.



Nuclear Axis

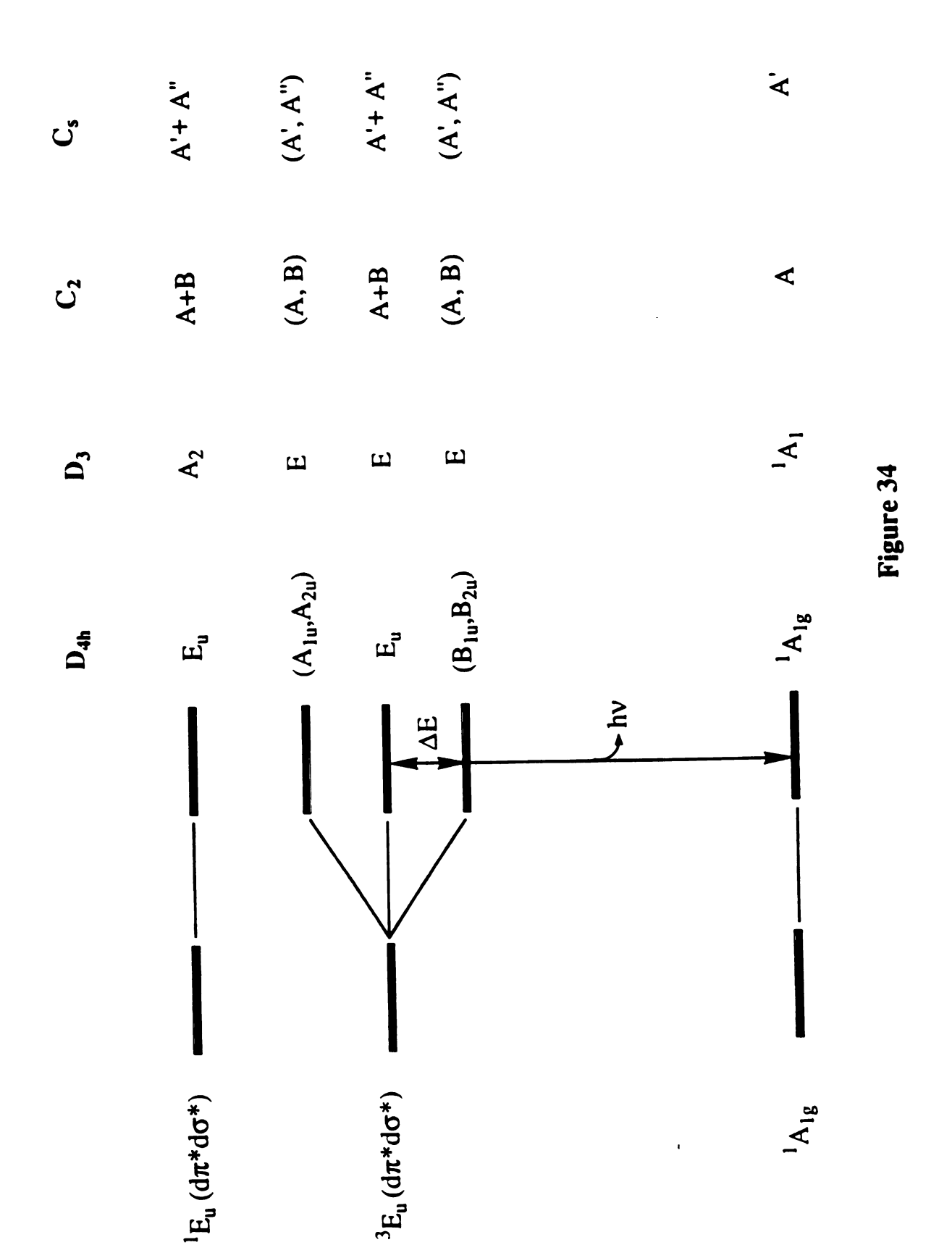
Figure 33

mechanism, as shown in Figure 34. Nevertheless, the importance of spin-orbit coupling to the luminescent properties is suggested by the increased energy gap and enhanced nonradiative decay of the deactivating state in the bromide complexes as compared to the chloride series. Thus, even though the overall molecular symmetry is low, the electronic structure of these compounds appear to reflect the pseudo-octahedral and trigonal bipyramidal symmetry of the rhodium group fragments.

Alternatively, in view of the low symmetry mixing of states, the data may be better represented by either a weak coupling model in which the emissive state is vibrationally coupled to the ground state, or a model in which the excited state is strongly coupled to a third state, allowing deactivating transitions to occur at the barrier crossing. The functional form of the equation for such a model would remain the same with only E_{act} the activation energy being substituted for ΔE . The strong coupling model applies principally to relaxation processes via rearrangement, whereas weak coupling is generally presumed to be the situation for small configurational changes and intersystem crossing.

The coupling of the metal-metal stretching frequency to a ground state vibration is shown in Figure 35. The coupling would then allow for non-radiative decay to ground state. There is precedence for this explanation of the thermal variation of the emission lifetimes. Steigman and Miskowski⁸ suggest hot band effects involving $v(Re_2)$, as an important factor in the temperature dependence of the emission from solid samples of $Re_2(dmpm)_2(CO)_6$. These thermal effects are well known for metal-metal $d\sigma \rightarrow d\sigma^*$ absorption transitions, due to the low frequency, thermally accessible, ground state metal-metal stretch.^{25(a)} This being the case for the

Figure 34. Proposed energy diagrams of the lowest energy excited states of Pt_2 (III,III) tetraphosphates and dirhodium fluorophosphine compounds. State manifolds are derived from the spin-orbit coupling perturbations of the $^{1,3}E_u$ states arising from one electron $(d\pi^* \rightarrow d\sigma^*)$ promotions. The point groups D_3 , C_s , and C_2 correspond to the complexes $Rh_2(0,0)$, $Rh_2(0,II)X_2$ and $Rh_2(II,II)X_4$ respectively.



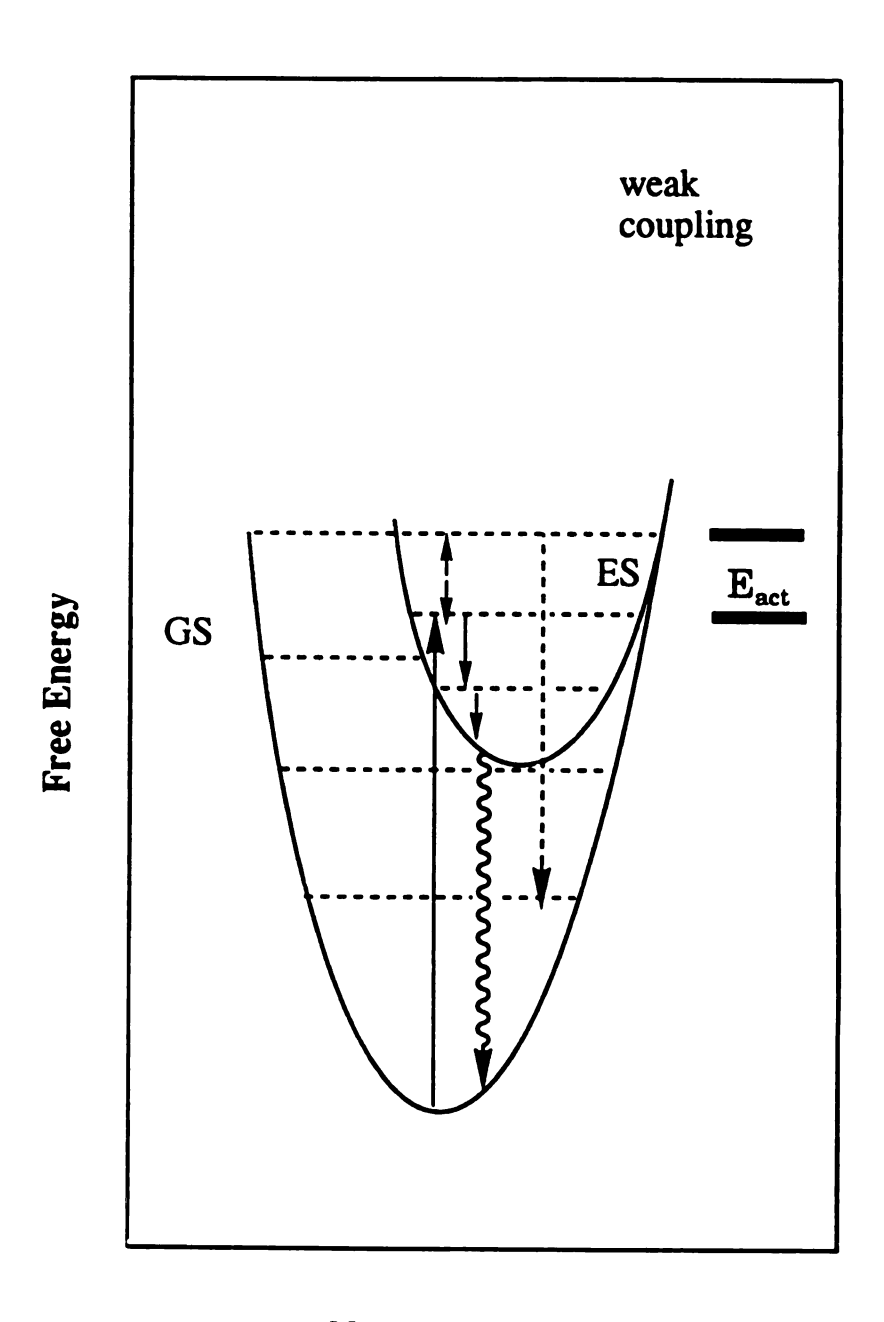
ground state of metal-metal singly bonded complexes, it is not unreasonable, then, to expect a thermally proximate metal-metal stretching frequency in the excited state where weakening of the M—M bond should even lower the energy of the metal-metal stretch.

Along similar lines, another possible explanation for the observed temperature dependency of the excited state lifetimes could be thermal promotion of an electron to an excited vibrational level leading to a twisting motion along the internuclear axis as depicted in Figure 36. Once at the top of the activation barrier, other deactivation pathways for the excited complex could become available, since it is well known that radiationless deactivations often take place at "critical" molecular configurations where touching or crossing of potential energy surfaces occur.³³

At this point, either the spin-orbit coupling model or the vibrational coupling model are the perfered explanations, in view of the fact that this temperature dependent behavior is observed from the complexes in the solid phase where twisting about the M—M bond should be hindered.

The electronic properties of the dirhodium fluorophosphine halides are well described by molecular orbital theory. These trends in absorbance and emission spectra along the series of halides are consistent with a $L(\sigma) \rightarrow d\sigma^*$ transition for the highest energy absorbance, followed by a $d\sigma \rightarrow d\sigma^*$ transition, with the lowest energy transition being $\pi^* \rightarrow d\sigma^*$. The greater shifts for the two higher energy transitionsalong the halide series is expected on the basis of configurational mixing arguments. The $L(\sigma)$ orbital will mix most strongly with $d\sigma$ orbitals as compared to orbitals with $d\pi$ symmetry. The lesser red shift in luminescence from the compounds is also consistent with emission arising from a $(d\pi^*d\sigma^*)$ excited state, which is also supported

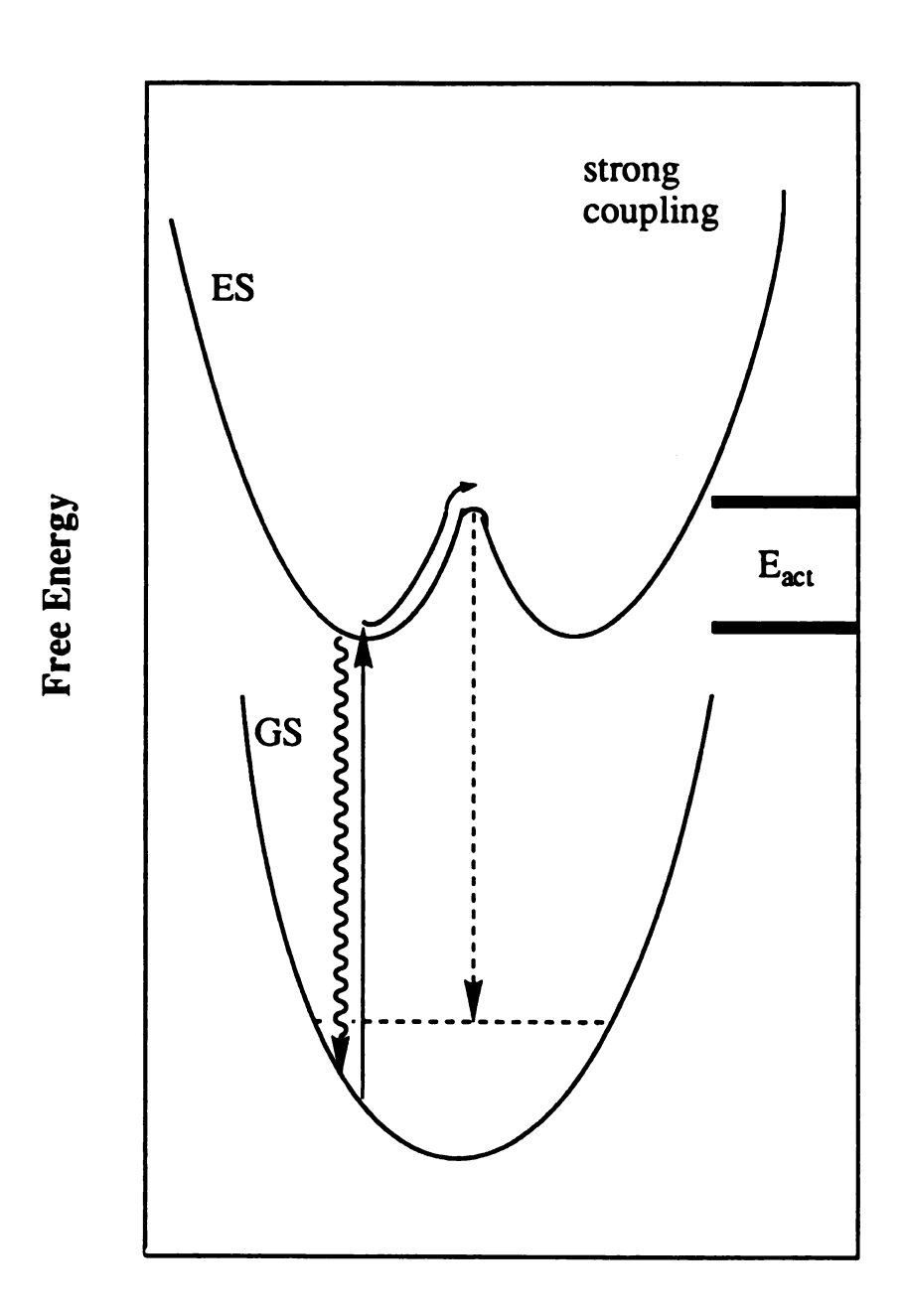
Figure 35. Potential surface illustrating coupling between vibrational levels of the excited state and ground state. Radiative decay is shown by zig-zag line; non-radiative by dotted line.



Nuclear Axis

Figure 35

Figure 36. Potential surface showing radiative and nonradiative deactivation pathways from an excited state which is strongly coupled to a second twisted excited state. Radiative transitions are depicted by zig-zag lines; non-radiative by dotted lines.



Metal—Metal Twist Axis

Figure 36

by excitation spectroscopy. Temperature dependence of the emission lifetimes are constent with a two-state Boltzmann model which places a nonradiatively deactivating state $\sim 400-1,000$ cm $^{-1}$ above the emissive excited state. The nonradiative decay rate constant of the upper excited state is 10^2-10^3 and 10^3-10^4 greater than the emissive excited state for complexes with X = Cl and X = Br, respectively.

The relatively long lifetimes of this ds* based excited state for these compounds, which is attenuated in fluid solution, is suggestive of a dissociative photochemistry for the complexes. Accordingly, studies were undertaken to investigate the photochemistry of these complexes in fluid solutions.

Chapter Four

Dirhodium Fluorophosphine Halides: Photochemistry

A. Introduction

Examples of photochemical oxidative addition of substrates to bimetallic complexes are numerous and include quadruply bonded compounds, dimetallic compounds strapped by a bidentate ligand across a core in which there is no metal-metal bond 10,32 and singly bonded metal complexes. 9,36 Examples, however, of reductive elimination from these complexes to leave the dimetallic core intact are far less known. For example, the compound $[Rh_2(bridge)_4Cl_2]^{2+}$, is obtained by photolysis of $[Rh_2(bridge)_4]^{2+}$ in the presence of HCl. 10 Attempts to reductively eliminate halides photochemically from this complex have resulted in only very small amounts of photoreduction. It is suggested that the dominant decay pathway of the $d\sigma \to d\sigma^*$ excited state is nonradiative decay to ground state with an excited state lifetime of less than $20 \text{ ps.}^{25(a)}$ This observation underscores the importance of a long lived excited state to this chemistry.

Even when reductive elimination photochemistry is observed, a number of conditions must be correct. $^{12(a)}$ UV-Visible irradiation of $[Pt_2(pop)_4X_2]^4$ [X = Cl, Br, I, H, CH₃I, Im (ImH = Imidazole)] in methanol results in the production of $[Pt_2(pop)_4]^4$ with nearly quantitative yield in all

cases. The proposed mechanism for the reaction begins with excitation of the $[Pt_2(pop)_4X_2]^{4-}$ complex producing $(\sigma)^1(\sigma^*)^1$ and $(\pi)^1(\sigma^*)^1$ singlet and triplet excited states. These excited states having one electron in a σ^* antibonding orbital have distortions along the Pt₂ axis which would perturb the Pt—X bonds causing axial ligand dissociation. Homolytic cleavage of the Pt—X bond generates the mixed valence X—PtIII—PtII intermediate which could then disproportionate to give [Pt2(pop)4]4- and [Pt2(pop)4X2]4- The photoreactions are wavelength dependent and suggestive of chemistry from more than one excited state, with the quantum yield from the higher energy excitation being almost ten times greater than from any lower excitations, in all cases. This phenomenon is attributed to the fact that the $X \to Pt^{III}$ charge transfer character in the $(\sigma)^1(\sigma^*)^1$ higher energy state should promote redox reaction with the formation of X—PtIII—PtII and halide radical species. In addition the photochemistry is solvent dependent as exemplified by the fact that even though the reactions are almost quantitative in methanol, the yield decreases to ~ 40 % when water is the solvent employed. These differences dramatically point to the role that conditions can play in either promoting or hindering the photoreductive elimination.

In attempting to effect multi-electron reduction of the dirhodium fluorophosphine halide complexes it will be shown that factors such as choice of solvent and wavelength of irradiation are tremendously important.

B. Results and Discussion

1. Attempted Photoreduction In the Presence of Excess Phosphine

Early attempts at photoreduction were undertaken employing Rh₂(II,II)Cl₂ with CH₃CN as solvent. The compound was irradiated using a 435 nm cutoff filter for wavelength selection and PF₃ was slowly bubbled into the photocell through a septum while the reaction was thermostatted at 20 °C. The solution was irradiated for a total of 120 min and the solvent was removed under vacuum. The FAB mass spectrum of the photoproduct was consistent with decomposition with no observable mass peaks above 512 amu. The same result was observed for the reaction when carried out in the dark at room temperature. These results were indicative of either impurities in the gas causing decomposition or oxygen leaking in through the needles or around the septum. An easier and more rigorous method involved the use of a solid or liquid phosphine which could be purified and rigorously deoxygenated prior to use. This method also could be carried out in a sealed photocell circumventing the need for a septum and the possibility of any leaks.

A variety of phosphines and phosphites were substituted in place of PF3 based on electronic and steric properties.³⁰ The electronic property monitored was phosphine or phosphite basicity and the steric property phosphine cone angle. Attempts were made employing PMe3, PEt3, PPh3, P(CH3CH2N)3, P(OMe)3, and P(OEt)3. Table 10 lists the solvents and conditions employed for irradiations carried out in the presence of PMe3, PEt3, PPh3, P(CH3CH2N)3, P(OMe)3, and P(OEt)3 and summarizes the observed results. In all cases, any phosphine or phosphite that reacted

Table 10 Reaction Conditions and Observed Results for Photolysis of Rh₂(0,II)Cl₂ in the Presence of Excess Phosphine or Phosphite

Phosphine or Phosphite	Solvent	Temp / °C	Reaction Time	Result
P(CH ₃ CH ₂ N) ₃	CH ₂ Cl ₂	20	110 min	NR
PMe ₃	CH ₂ Cl ₂	20	Instantaneous	Δ Reaction
PEt ₃	CH ₂ Cl ₂	20	Instantaneous	Δ Reaction
PPh ₃	CH ₂ Cl ₂	20	180 min	NR
P(OMe)3	CH ₂ Cl ₂	20	Instantaneous	Δ Reaction
P(OEt)3	CH ₂ Cl ₂	-20	12 hr	Δ Reaction
CH ₃ N(PF ₂) ₂	CH ₂ Cl ₂	20	12 hr	Δ Reaction

photochemically with the complex would also react thermally. The trends in reactivity followed neither trends in phosphine bascity nor sterics and is probably due to some combination of both.

2. Attempted Photoreduction In A Coordinating Solvent

Because PR3 reacted thermally with the Rh2(0,II)Cl2 complex, irradiations were performed in the absence of excess ligand. The rationale was that CH₃CN would occupy the axial coordination site upon photoinduced reductive elimination. This solvent is known to stabilize a [Rh₂]⁴⁺ center requiring no other ligands for coordination.³⁷ Irradiation of Rh₂(0,II)Cl₂ was carried out at 0 °C at wavelengths greater than 375 nm. After two hours there was a minimal reduction of starting material as evidenced by UV–Visible spectroscopy. This result suggested the use of a chloride radical trap may drive the reaction further toward completion.

The radical trap chosen was 2,3- dimethyl-1,3- butadiene. As no comparison of the Cl· radical trapping abilities of various compounds could be found, my choice was based on information concerning the various classes of olefins toward methyl radical addition.³⁸ In this study isolated dienes show reactivities approximately twice as high as the corresponding monoolefins with the reactivities of conjugated dienes much greater. This is due to the resonance stabilization of the radical formed. The presence of methyl groups on C(2) and C(3) can further stabilize the radical through hyperconjugation. Because this compound is not soluble in CH₃CN, the coordinating solvent THF, was employed in it's place for the photolysis.

3. Photochemistry In Tetrahydrofuran

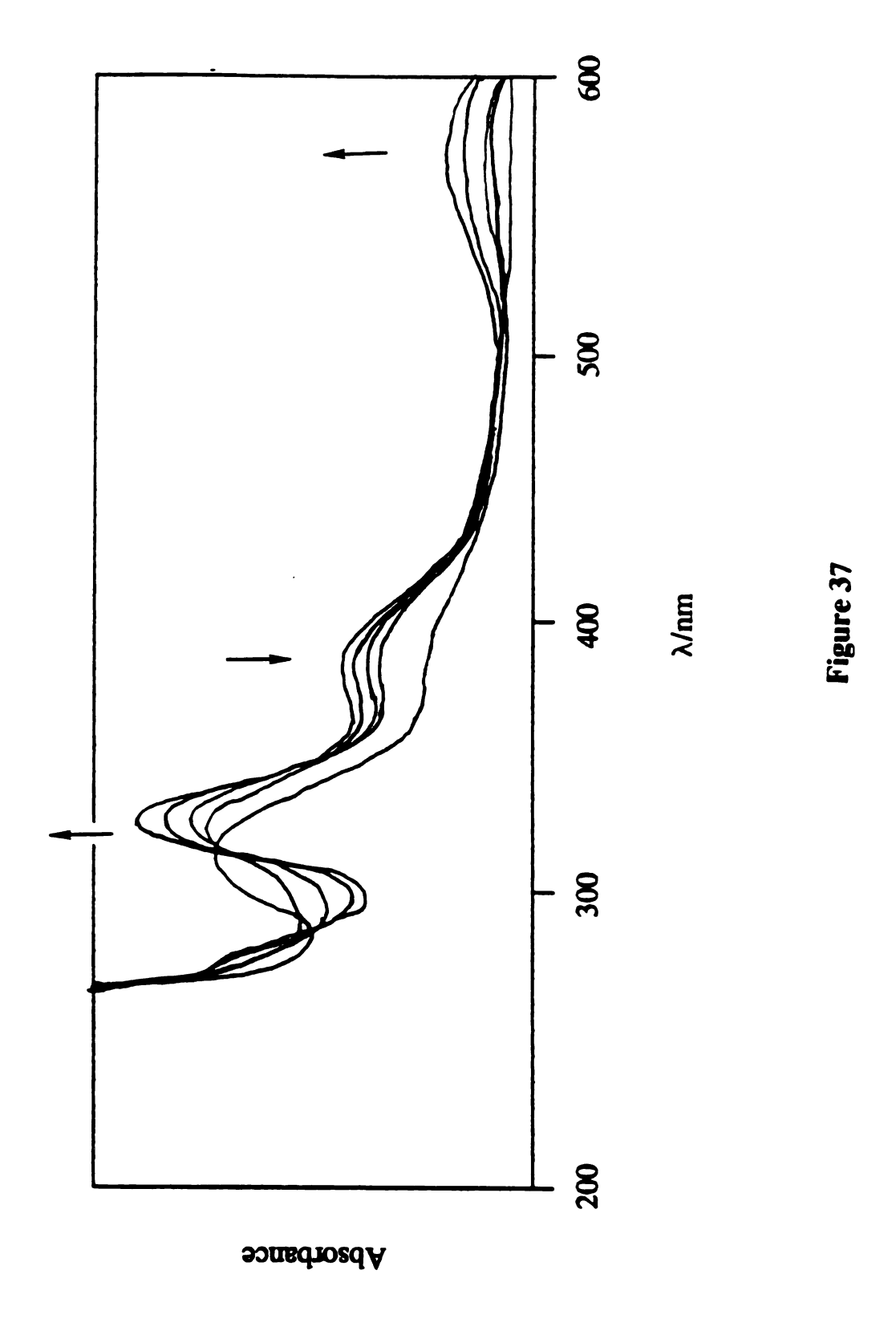
Irradiation was undertaken on a solution of Rh₂(0,II)Cl₂ in THF, containing 2,3-dimethyl-1,3-butadiene. The solution in the photocell was thermostatted at -10 °C and a 375 nm cutoff filter was employed to select the wavelengths for irradiation. Figure 37 displays the changes in the UV-Visible spectrum during 195 min of photolysis. The absorption spectrum displays an isosbestic point which is maintained during 105 min of photolysis. There is also a band at 570 nm which is observed to grow in during the first 105 min of the reaction and then disappear in the final spectrum. The removal of the solvent and subsequent FAB mass spectral analysis of the remaining solid exhibited peaks only indicative of the starting compound. Heating of a similar solution to 50°C, while protecting the cell from light for 11 hours resulted in no reaction as evidenced by UV-Vis spectroscopy.

The appearance and subsequent disappearance of the band at 570 nm in the photoreaction indicated the possibility of formation of a one - electron mixed valent species. Low energy transitions within the $d\pi$ and $d\delta$ levels are possible with the removal of an electron. from the complex, accounting for the observed blue color in solution. An analogous mixed valent species is formed by the thermal reaction of HCl and $[Rh_2(bridge)_4]^{2+}$. That reaction proceeds according to the equations below;

$$\begin{array}{c}
\Delta \\
[Rh_2(bridge)_4]^{2+} + HCl \rightarrow [Rh_4(bridge)_8Cl]^{6+} + 1/2 H_2
\end{array} (1)$$

$$hv$$
[Rh₄(bridge)₈Cl]⁶⁺ + HCl \rightarrow [Rh₂(bridge)₄Cl2]²⁺ + 1/2 H₂ (2)

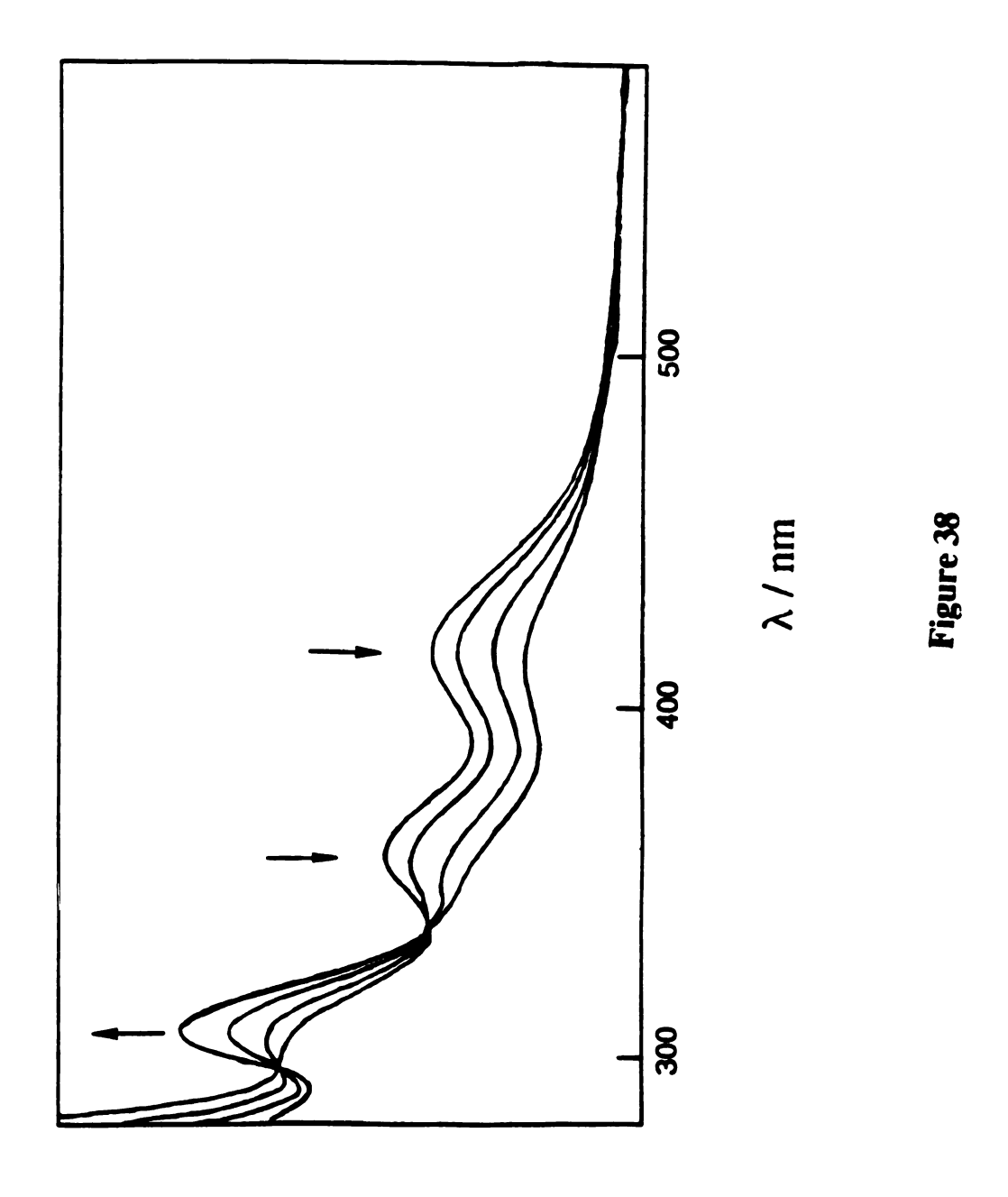
Figure 37. Electronic absorption spectral changes during photolysis ($\lambda > 375$ nm) of a THF solution of Rh₂(0,II)Cl₂ containing 2,3-dimethyl-1,3-butadiene at -10 °C. Total irradiation time was 195 min.



A blue mixed valent intermediate is formed in step 1 where [Rh₂(bridge)₄]²⁺ abstracts a chloride radical from HCl yielding a half mole of H₂ and forming a tetranuclear complex made up of two binuclear [Rh₂(bridge)₄]³⁺ units linked by a Rh—Rh bond. The Cl⁻ ion bridges the [Rh₄(bridge)₈]⁶⁺ units forming a linear infinite chain of repeating Rh₄Cl units. This complex is the active species which then goes on to do the photochemistry in step 2 yielding another half mole of H₂ and the binuclear [Rh₂(bridge)₄Cl₂]²⁺ cation. However, while the mixed valent Rh₄(bridge)₈Cl]⁶⁺ cation was stable enough to obtain crystals for X-ray analysis, our blue species is unstable when the solution is warmed to room temperature. ^{10(c)} Attempts to observe this species by low temperature EPR (-10 °C) failed yielding no signal.

If the photochemical reductive elimination from the dirhodium fluorophosphine dichloride species proceeded by a radical mechanism, with the primary activation step being M—X cleavage, perhaps reductive elimination of bromine from the dibromide complex would be facilitated owing to the weaker metal halide bond. Proceeding on this assumption, a tetrohydrofuran solution of the dibromide complex containing 2,3-dimethyl-1,3-butadiene was irradiated for two hours employing a 375 nm glass cutoff filter while thermostatted at 0° C. No reaction occurred during this time. However when the wavelength of irradiation was changed by switching to a 305 nm cutoff filter the photolysis proceeded quickly to yield a product with the UV-Visible spectrum observed in Figure 38. The photoreaction shown in the figure occurred within 115 min. The two lower energy bands are reduced significantly during this time and the band at 305 nm is observed to grow in. The 305 nm absorption peak is indicative of the formation of a reduced

Figure 38. Electronic absorption spectral changes during photolysis ($\lambda > 305$ nm) of a THF solution of Rh₂(0,II)Br₂ containing 2,3-dimethyl-1,3-butadiene at -10 °C. Total irradiation time was 115 min.



Absorbance

species; the complex Rh₂[CH₃N(PF₂)₂](PF₃)₂ having a similar absorption profile.¹² It is interesting to note that the same photochemistry is observed whether or not the radical trap is employed and even when no trap is used there occurs no significant amount of thermal back reaction over a period of 10 days.

The FAB mass spectrum of the photoproduct is shown in Figure 39. Observed are peaks indicative of a variety of products including Rh₂[CH₃N(PF₂)₂]₃[(F₂P)CH₃NH]₂. This compound was prepared independently and the mass spectrum is displayed in Figure 40. Peaks common to both specta include 905 amu corresponding to $Rh_2[CH_3N(PF_2)_2]_3[(F_2P)CH_3NH]_2$, 806 amu resulting from $Rh_2[CH_3N(PF_2)_2]_3[(F_2P)CH_3NH]$, and 707 amu, the mass of Rh₂[CH₃N(PF₂)₂]₃. Obviously, however there was not only one product formed in the reaction. Peaks at 874 and 776 correspond to $Rh_2[CH_3N(PF_2)_2]_3[(F_2P)CH_3NH](PF_2H)$ and $Rh_2[CH_3N(PF_2)]_3(PF_2H)$. Also observed are unknown peaks at [M/Z] 894, 787, and 688 amu. These unknown peaks do not correspond to any reasonable structure in which a rhodium center is coordinated by THF, to stabilize the photoproducts. Extremely noticeable however, is the role played by the fluorophosphine ligands in stabilizing the photoproducts. This fact led to attempting the photochemistry in the presence of excess fluorophosphine ligand.

A THF solution of $Rh_2(0,II)Br_2$ containing 2,3-dimethyl-1,3-butadiene and $CH_3N(PF_2)_2$ was irradiated $\lambda > 305$ nm. Irradiation was continued, while monitoring by UV-Vis spectroscopy for one hour and the spectrum shown in Figure 41 was obtained. During photolysis the two lower energy bands decrease and a band at 312 nm is grows in. This absorption maximum is found for the previously mentioned complex

Figure 39. FAB mass spectrum of the photoproducts isolated from photolysis (1 > 305 nm) of Rh₂(0,II)Br₂ in a THF solution containing 2,3-dimethyl-1,3-butadiene at -10 °C. Assignments of the peaks in the spectrum correspond to: (a) Rh₂[CH₃N(PF₂)₂]₃[(PF₂)CH₃NH]₂, (b) Rh₂[CH₃N(PF₂)₂]₃[(PF₂)CH₃NH](PF₂H), (c) unknown.

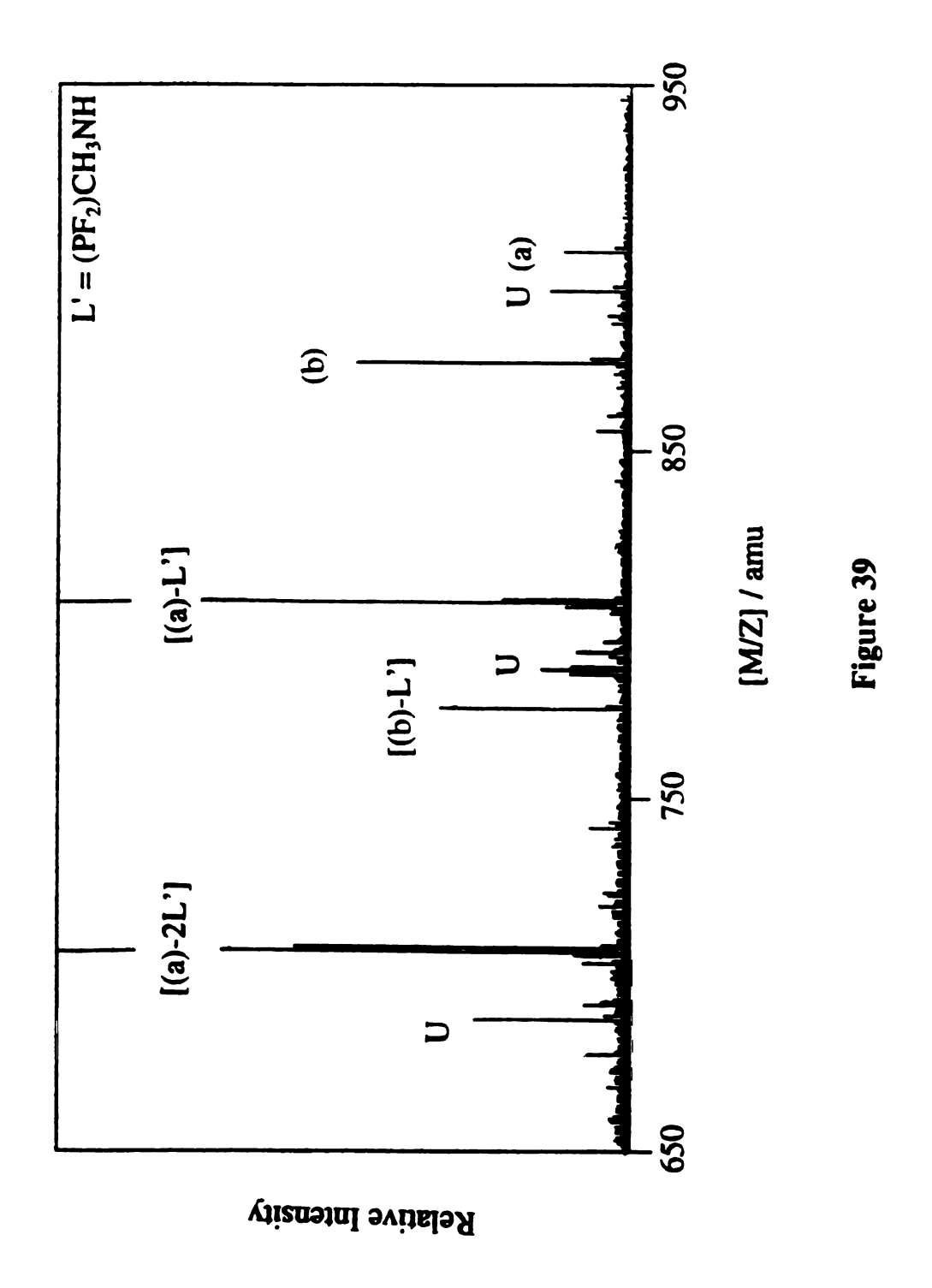


Figure 40. FAB mass spectrum of the compound $Rh_2[CH_3N(PF_2)_2]_3[(F_2P)CH_3NH]_2$ in the [M/Z] range 650-950 amu.

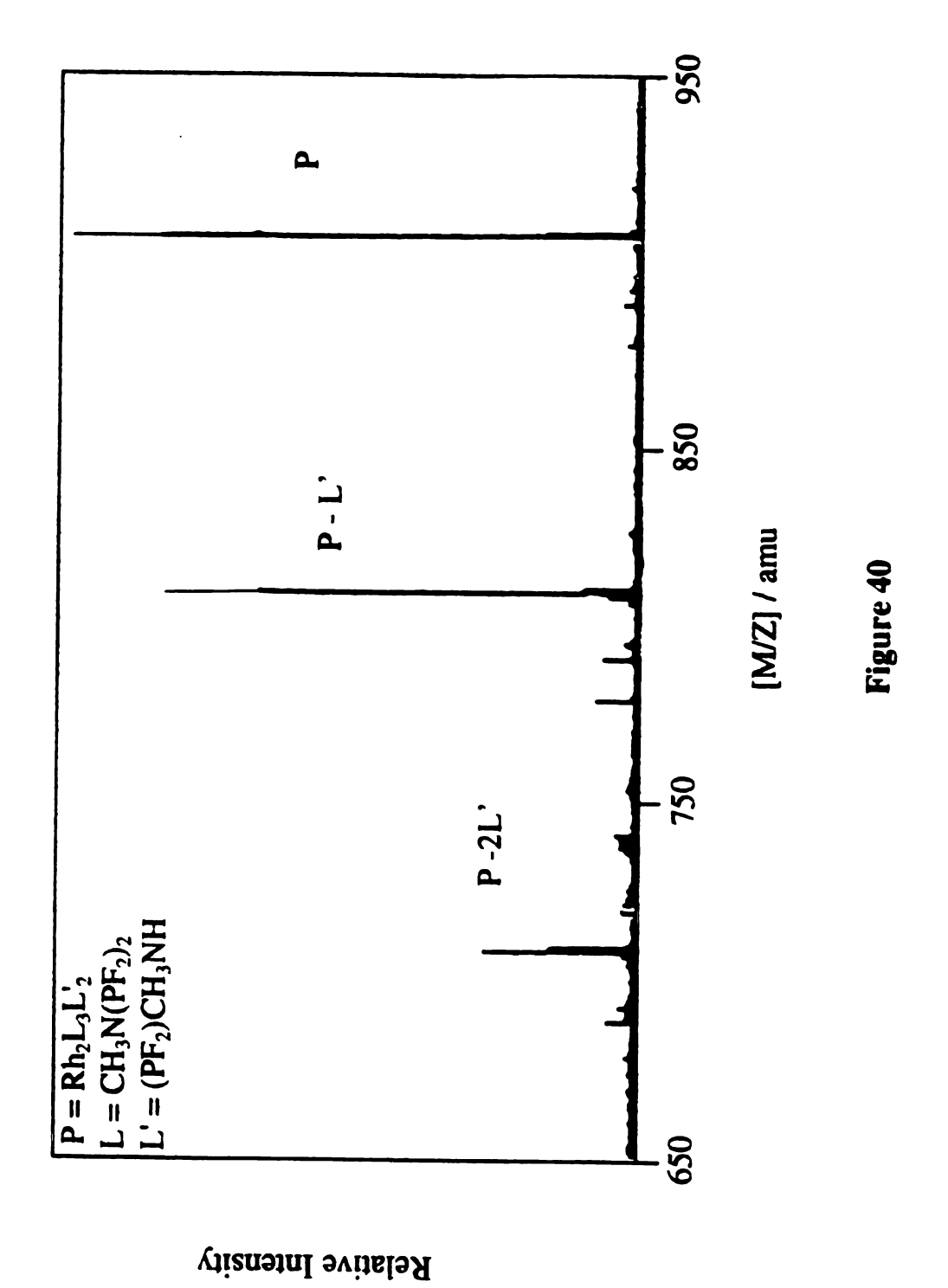


Figure 41. Electronic absorption spectral changes during irradiation ($\lambda > 305$ nm) of a THF solution of Rh₂(0,II)Br₂ containing 2,3-dimethyl-1,3-butadiene and CH₃N(PF₂)₂ in excess at -10 °C. Total irradiation time was 60 min.

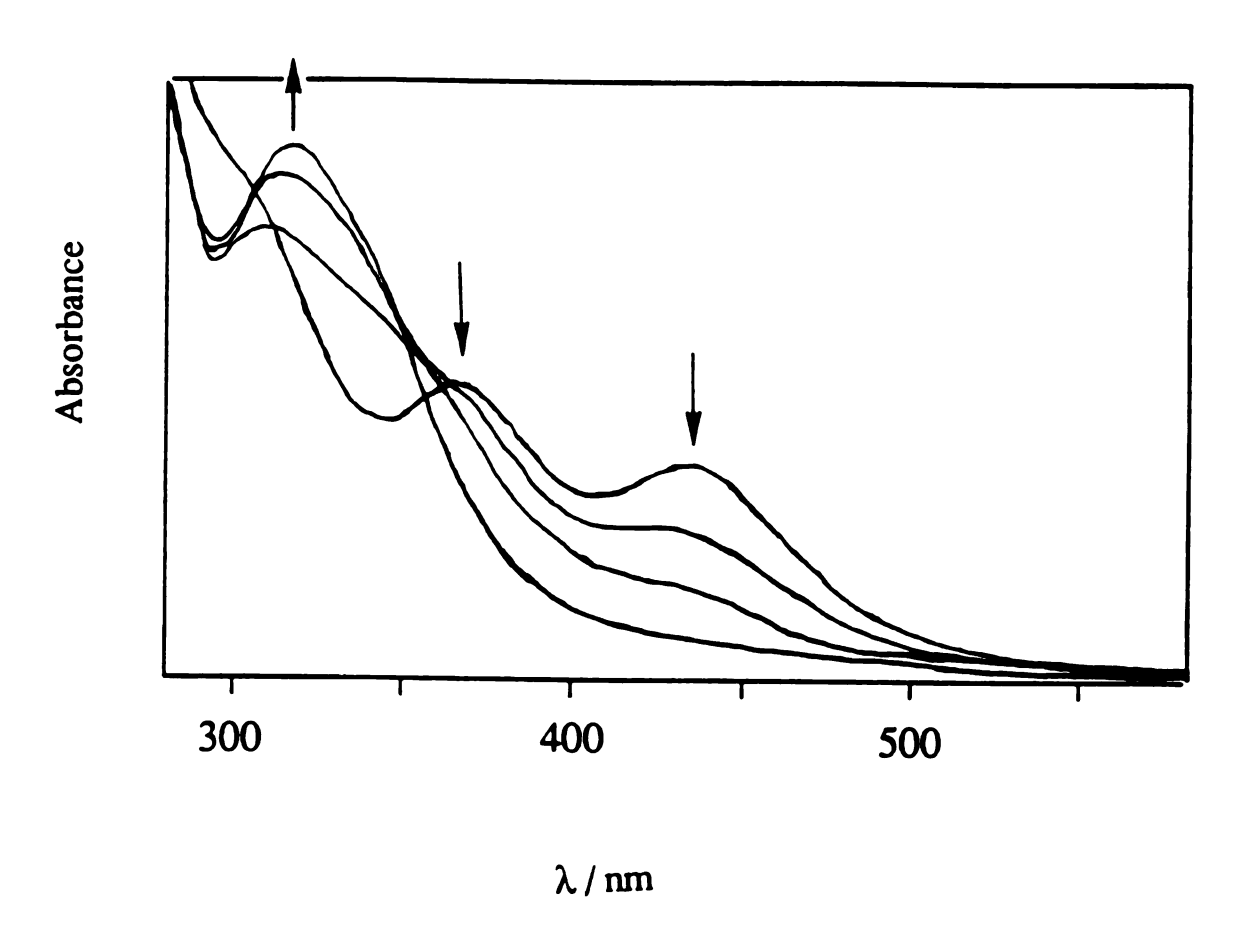


Figure 41

Rh₂[CH₃N(PF₂)₂]₃[(F₂P)CH₃NH)]₂. The absorption spectrum of the independently prepared complex is shown in Figure 42. This complex, however, while present, does not appear to be the predominant product of this reaction as evidenced by the FAB mass spectrum of the photoproduct, Figure 43. While this spectrum is complex and the low intensity of the peaks above the baseline noise make it more complicated, clearly a peak at 976 amu, corresponding to Rh₂[CH₃N(PF₂)₂]₄[(F₂P)CH₃NH)] which was not present in the spectrum of the previous photoproduct is observed. (No product of mass higher than 905 amu was observed in the mass spectrum of the products from the previous photoreaction.) This fact suggests that when excess fluorophosphine ligand is available, it will coordinate to the open axial site formed by reductive elimination of bromine. A thermal check of this reaction produced a different product which was not characterized.

Figure 44 summarizes the photochemistry which has been identified from the fast atom bombardment mass spectra and absorption data. Photolysis of the Rh₂(0,II)Br₂ complex in THF with no excess fluorophosphine present yields the products Rh₂[CH₃N(PF₂)₂]₃-[(F₂P)CH₃NH]₂ and Rh₂[CH₃N(PF₂)₂]₃[(F₂P)CH₃NH](PF₂) along with one or two unknowns. The same photochemistry occurs in the presence of excess fluorophosphine along with the production of Rh₂[CH₃N(PF₂)₂]₄[(F₂P)CH₃NH].

The observation of a photoreaction with irradiation of the dirhodium fluorophosphine dibromide complex at wavelengths greater than 305 nm which is not observed with irradiation at wavelengths greater than 375 nm is consistent with irradiation of the $(X)\sigma \to \sigma^*$ transition. The considerable charge transfer character of this transition allows more facile cleavage of the Rh—X bonds.

Figure 42. Electronic absorption spectrum of Rh₂[CH₃N(PF₂)₂]₃[(F₂P)CH₃NH]₂, dissolved in CH₂Cl₂ at room temperature.

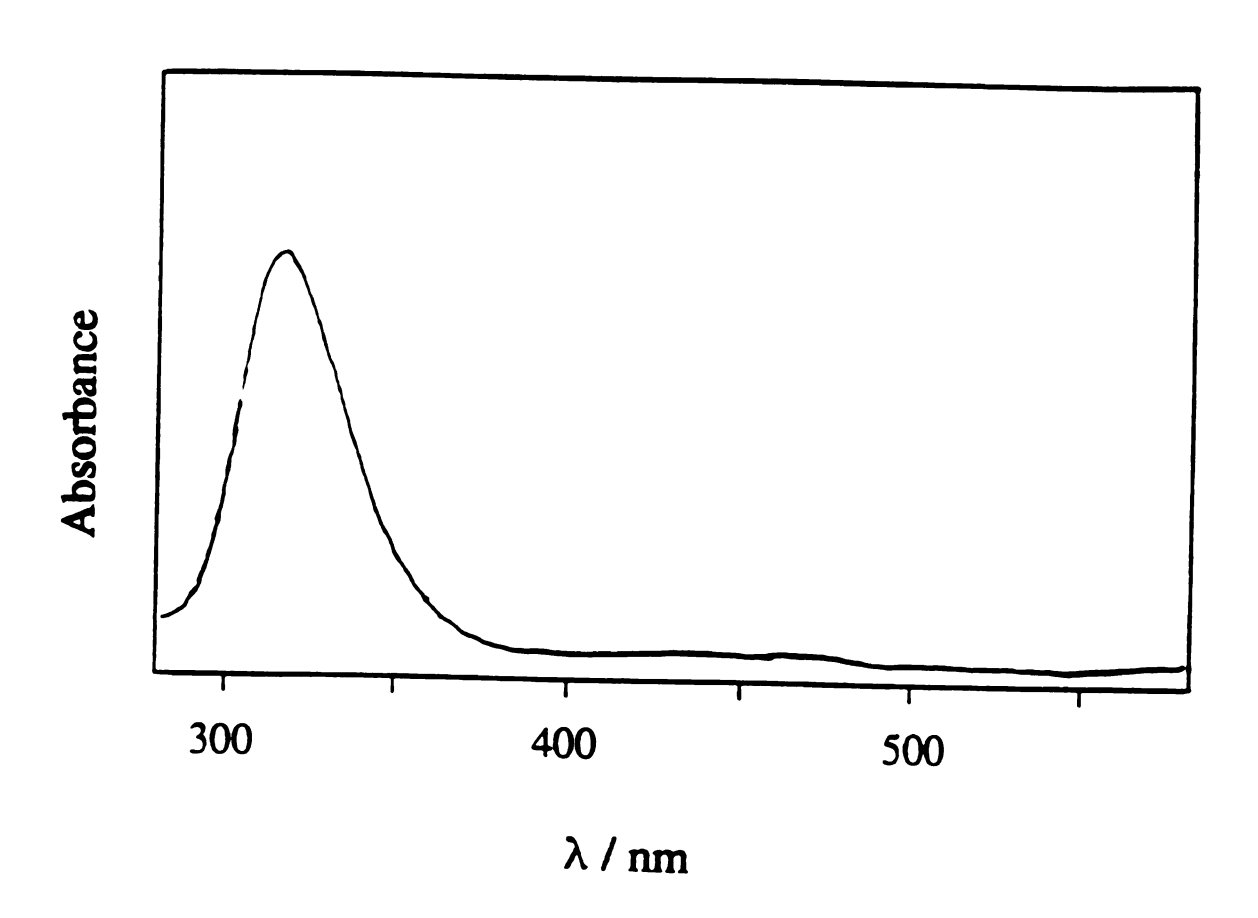


Figure 42

Figure 43. FAB mass spectrum of the photoproducts isolated from photolysis ($\lambda > 305$ nm) of Rh₂(0,II)Br₂ in a THF solution containing 2,3-dimethyl-1,3-butadiene and CH₃N(PF₂)₂ in excess at -10 °C. Peak at [M/Z] 976 amu corresponds to Rh₂[CH₃N(PF₂)₂]₄[(F₂P)CH₃NH)]. Other observable masses correspond to fragmentation peaks from (a) Rh₂[CH₃N(PF₂)₂]₃[(F₂P)CH₃NH]₂, (b) Rh₂(0,II)Br₂, and (c) unknown.

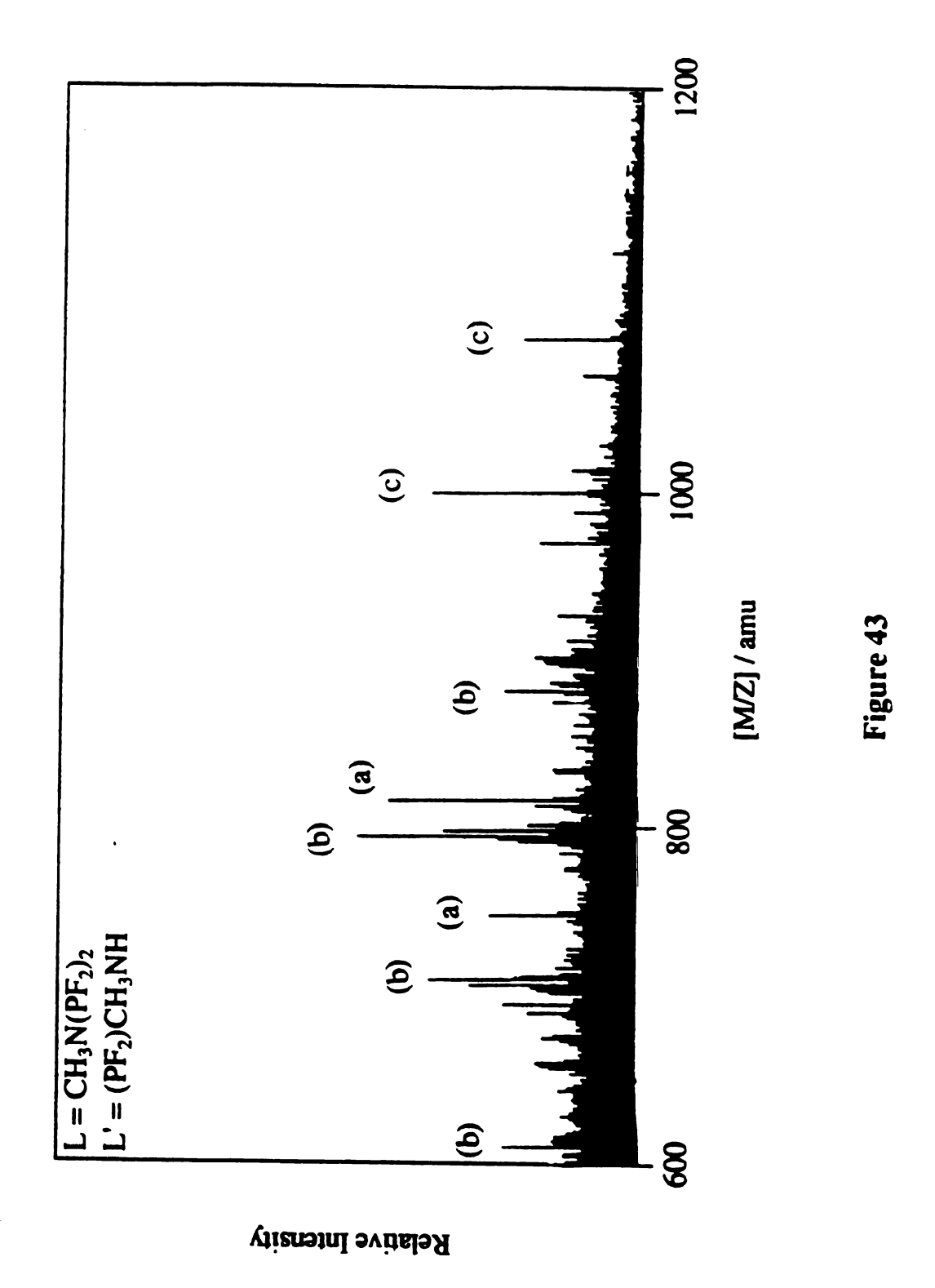


Figure 44. Summary of the photoproducts formed by the photolysis of Rh₂(0,II)Br₂ which have been identified by FAB mass spectroscopy and absorption spectroscopy.

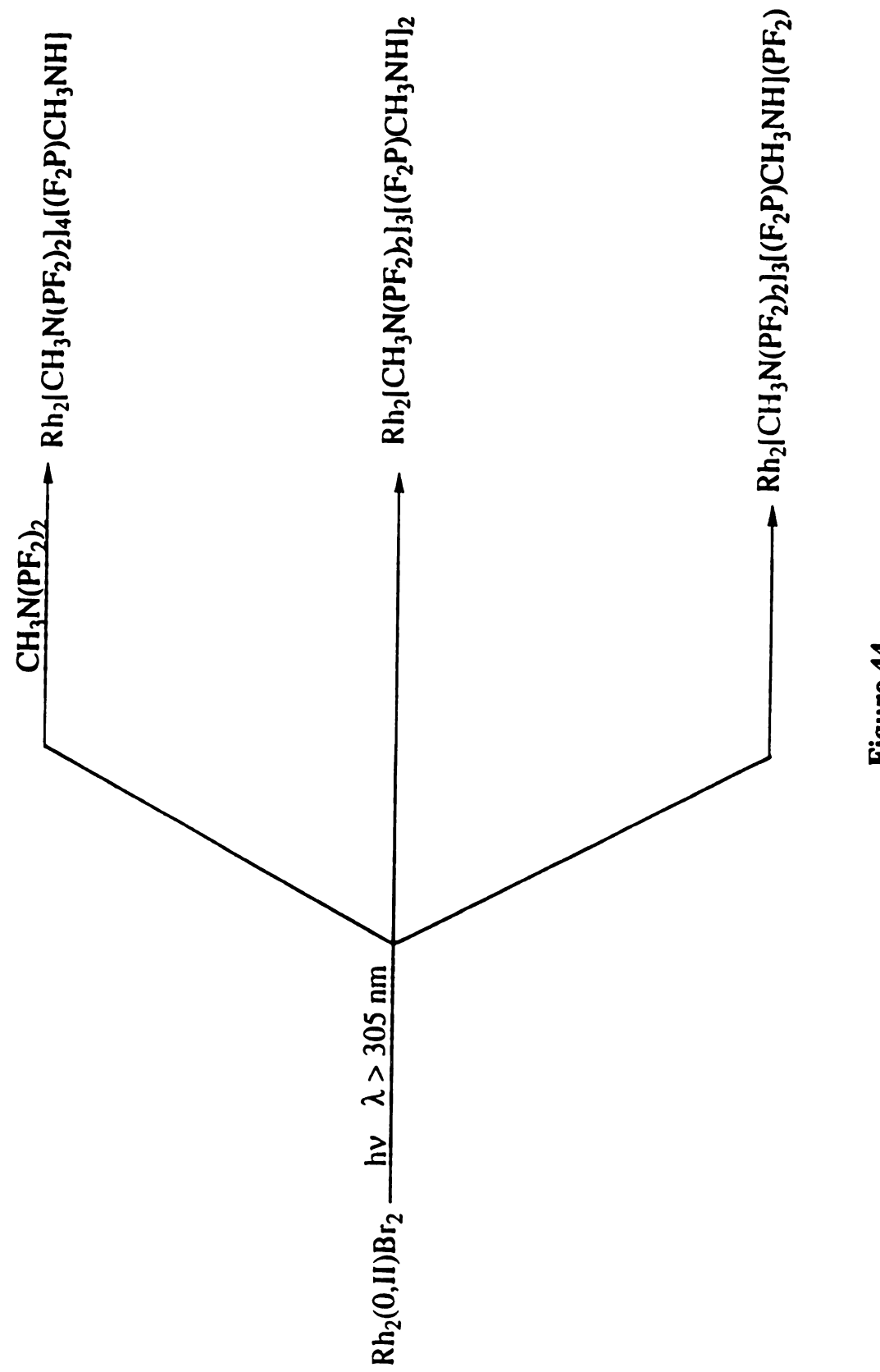


Figure 44

Both of the photoreductions discussed are likely to proceed via a radical mechanism. The formation of the blue intermediate when X = Cl is indicative of a radical species. When X = Br the FAB mass spectrum of the photoproduct shows no evidence of formation of $Rh_2(II,II)Br_4$. That information coupled with the fact that the reverse of the photochemical reaction doesn't proceed to any measurable degree makes it unlikely that Br_2 is formed during the photolysis. It should be noted that bromine is an efficient oxidant in the synthesis of $Rh_2(II,II)Br_4$. One possibility is that the Br_1 radicals formed are scavenged by the solvent.

While a crystallographic analysis of the photoproduct (photoproducts) formed in the reaction will be important in pinning down the mechanism of this photochemistry, discussion of a possible pathway can be attempted. Consistent with the distribution of photoproducts, is the possibility that as the excited $Rh_2(0,II)Br_2$ complex loses 2 Br· radicals, leaving an open coordination site. This site is stabilized by coordination of one end of a difluorophosphine ligand which is singly coordinated to another molecule, as shown in Figure 45. Cleavage of this ligand to yield fragments $(F_2P)CH_3N$ · and $(F_2P\cdot)$ and subsequent trapping by a good hydrogen atom donor solvent would afford the products seen in the mass spectrum.

With the parallels between the reductive elimination photochemistry of the dirhodium fluorophosphine dihalides and that of diplatinum pyrophosphite dihalides some important trends in the design and use of bimolecular systems capable of photochemical reductive elimination begin to emerge. Firstly the system must posses a long lived excited state from which photoelimination is possible. This is evidenced by the fact that while these two systems undergo reductive elimination photochemistry, the complex

Figure 45. Possible reaction pathway followed by Rh₂(0,II)Br₂ upon excitation. Heterolytic cleavage of two Br· radicals followed by stabilization of the open coordination site by a difluorophosphine axially coordinated to another molecule. Cleavage of the coordinating ligand into fragments which are stabilized by H· from the solvent THF.

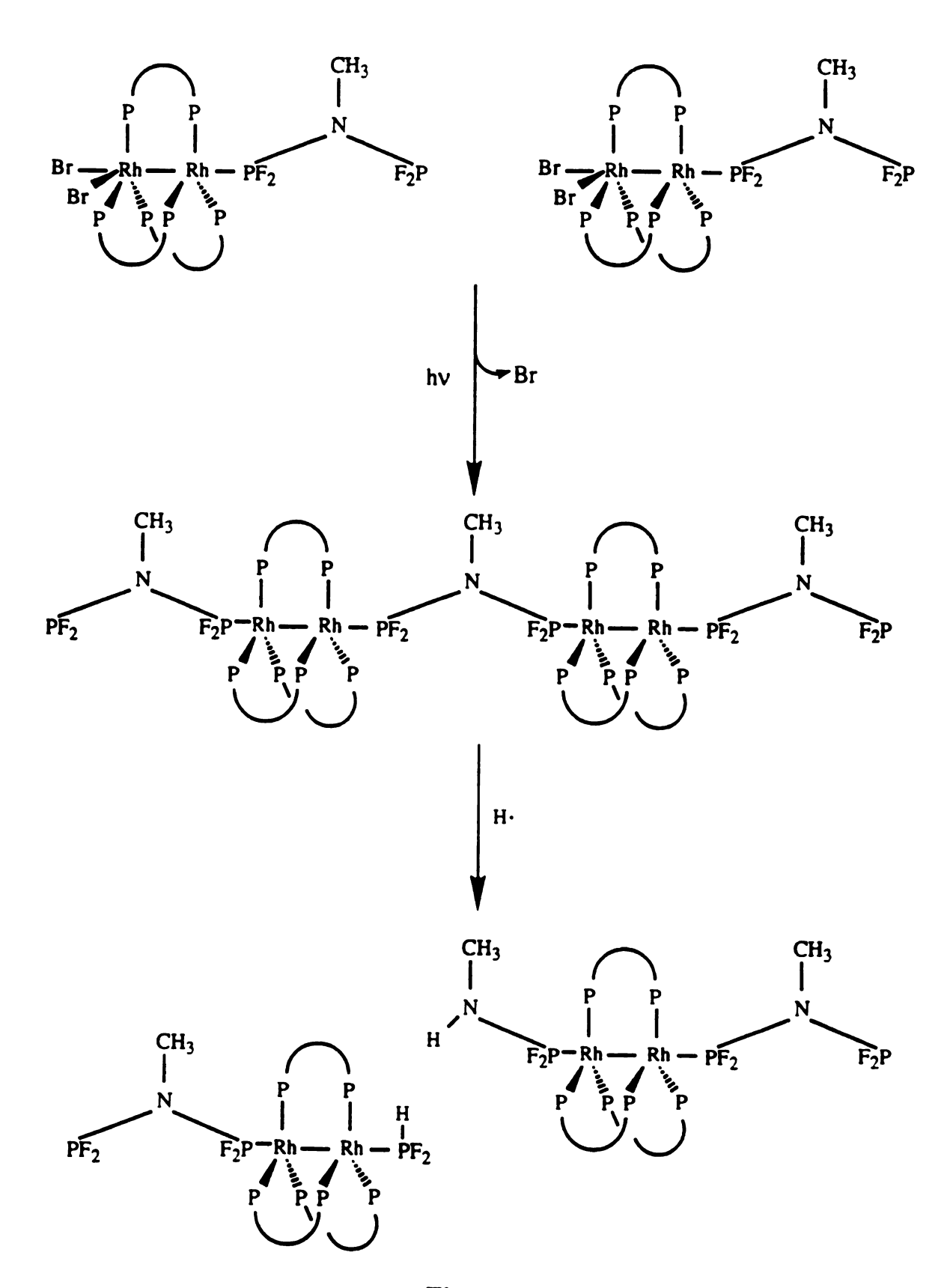


Figure 45

[Rh₂(bridge)₄X₂]²⁺, possessing an excited state with a lifetime of less than 20 ps is only marginally capable of reductive elimination photochemistry. Secondly, in both complexes, reductive elimination is greatly enhanced (in the case of Rh₂(0,II)Br₂, it is only possible) when irradiation promotes ligand – to – metal excitation. Thirdly, solvent choice is very important to the photochemistry of both of the systems. Whether the solvent acts to stabilize the photoproduct or to trap photochemically generated radicals remains however, to be elucidated.

Future studies should include photolysis in the presence of other hydrogen donor solvents to determine if, in fact, a hydrogen atom donor solvent is necessary for photoreactivity. Transient absorption is a powerful tool in the determination of lifetimes and identities of intermediates and could possibly help to elucidate the mechanisms of the reactions. In order to test the validity of the proposed intermediate possessing a fluorophosphine bridging two of rhodium dimers, similar photochemistry should be attempted employing the compounds with the axially coordinated PF₃ instead of the axial fluorophosphine.

Chapter Five

Concluding Remarks

The discovery of reductive elimination photochemistry from the twoelectron mixed-valence complex Rh₂(0,II)Br₂ represents a significant step in the construction of an efficient energy storage system. Two-electron complexes complexes appear to be a promising route to overcome the thermodynamic barriers hindering regeneration of a multielectron reagent from its' photoproduct.

The ability to surmount such a thermodynamic barrier is crucial to the realization of a catalytic photochemical scheme for energy storage as described by the equation:

$$2HX \rightarrow H_2 + X_2 \tag{3}$$

where X = Cl or Br. Both of the reactions are energetically uphill processes; the standard reduction potentials (E⁰) being -1.36 V and -1.07 V, respectively.

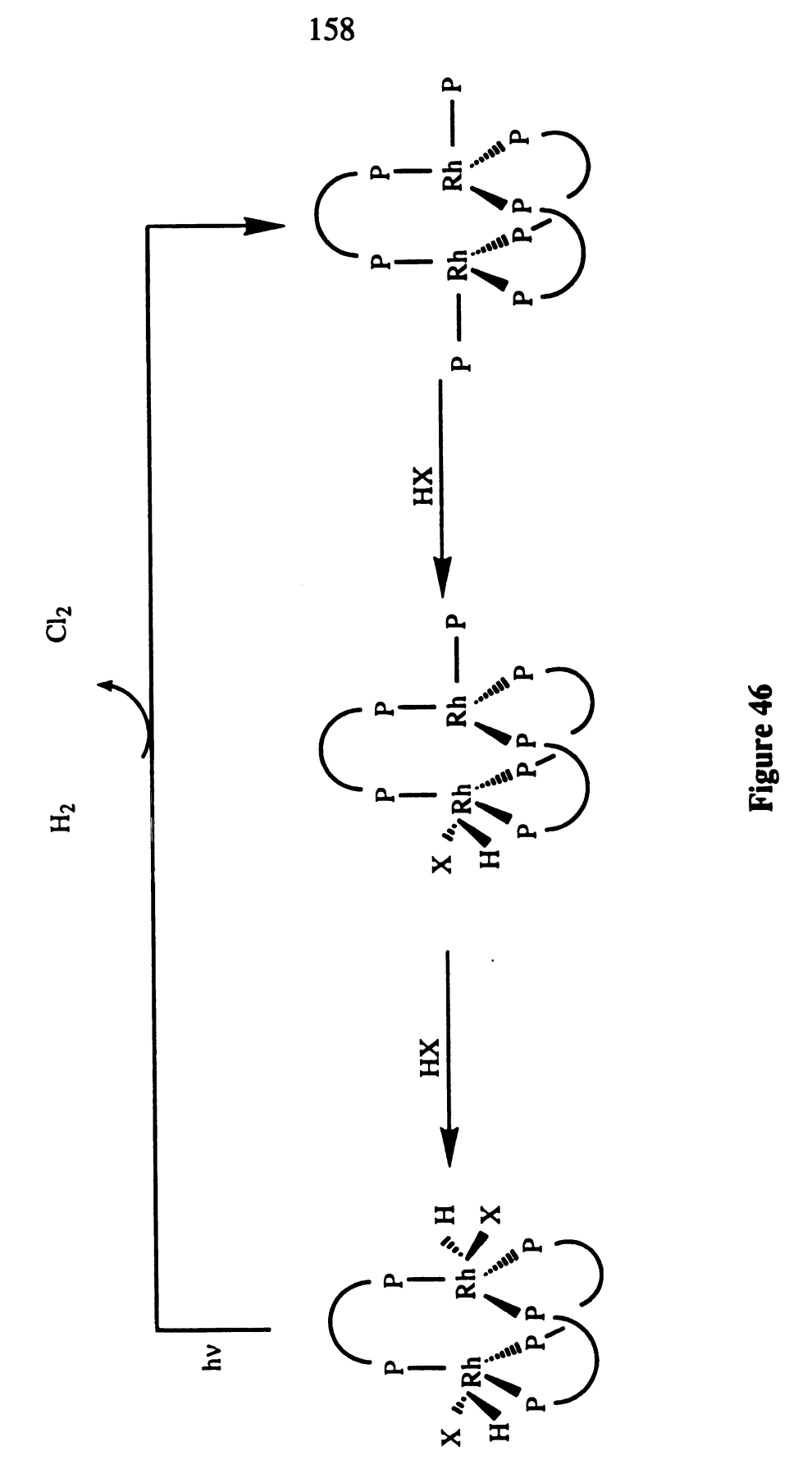
The utility of such an energy storage system lies in its' ability to store energy in a compact chemical form (such as hydrogen) making it easily transportable and storable. Such an energy source could be used to supplement our fossil fuel supply. The $d\sigma^*$ excited states of Rh₂(0,0),

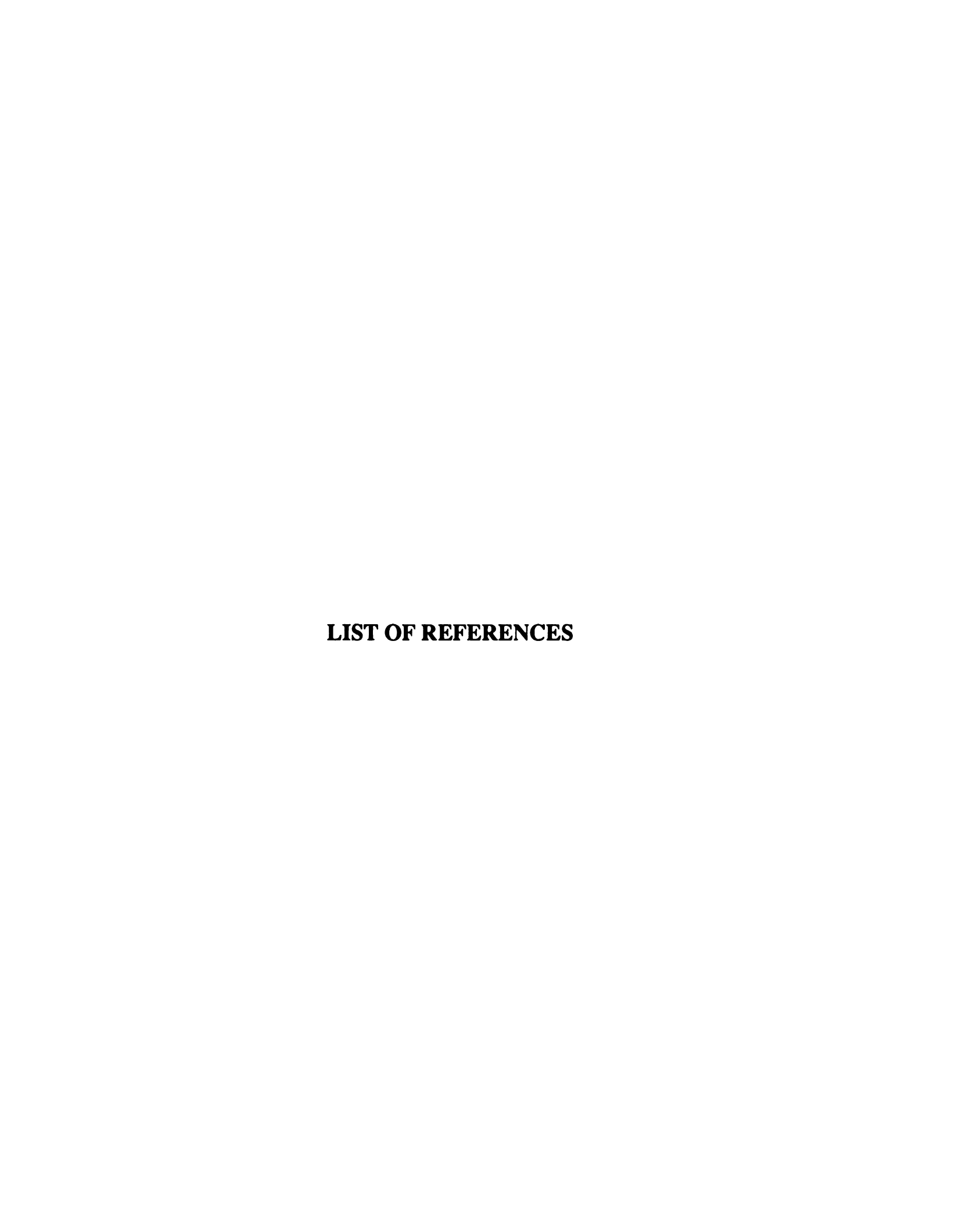
Rh₂(0,II)X₂, and Rh₂(II,II)X₄ complexes, along with their photoreductive elimination constitute basic components to the realization of HX energy storage photochemistry.

We beleive that a plausible system for HX splitting photochemistry based on the dirhodium fluorophosphines begins with addition of the binuclear Rh₂(0,0) to an HX saturated solution with thermal and / or photochemical production of hydrogen and Rh₂(0,II)X₂. The final step would be the photochemical reduction of the dirhodium fluorophosphine dihalide regenerating the initial photoreagent. If the first step produces a hydrido-halide, as shown in Figure 46, irradiation of this resultant hydrido-halide at wavelengths capable of breaking either the hydride or halide bonds while leaving the other intact might be feasible.

A number of factors will be necessary in order for this chemistry to occur. Thermal addition of HX to the $Rh_2(0,0)$ complex must yield structures similar to the $Rh_2(0,II)X_2$ and $Rh_2(II,II)X_4$ complexes in order for the excited state properties to be preserved. The excited state chemistry present; H_2 and X_2 photochemical elimination must be preferred over elimination of HX. On the basis of this scheme, it is encouraged that the hydrido-halo chemistry of the dirhodium fluorophosphine complexes be investigated in the near future. The possibilities for the future photochemistry of these complexes are looking bright.

Figure 46. Possible four electron chemistry which could be accomplished with a series of multi-electron photoreagents.





LIST OF REFERENCES

- 1. Voet, D.; Voet, J. G.; "Biochemistry" Wiley: New York, 1990; p 596.
- (a) Wasielewski, M.R. Chem. Rev. 1992, 92, 435 and references therein.
 (b) Gust, D.; Moore, T. A.; Moore, A. L.; Lee, S.-J.; Bittersmann, E.; Luttrull, D. K.; Rehms, A. A.; DeGraziano, J. M.; Ma, X. C.; Gao, F.; Belford, R. E.; Trier, T. T. Science 1990, 248, 199.
 (c) Harriman, A.; Kubo, Y.; Sessler, J. L. J. Am. Chem. Soc. 1992, 114, 388.
 (d) Wang, D. W.; Zhang, B. W.; Bai, J. W.; Cao, Y.; Xiao, X. R.; Xu, J. M. J. Phys. Chem. 1992, 96, 2886.
- (a) Kim, Y. I.; Mallouk, T. E. J. Phys. Chem. 1992, 96, 2879.(b) 3. Krueger, J. S.; Lai, C.; Li, Z.; Mayer, J. E.; Mallouk T. E. In Inclusion Phenomena and Molecular Recognition; Atwood, J. Ed.; Plenum Press: New York, 1990. (c) Kamat, P. V. Chem. Rev. 1993, 93, 267. (d) Thomas, J. K. Chem. Rev. 1993, 93, 301. (e) Yoon, K. B. Chem. Rev. 1993, 93, 321. (f) Fox, M. A.; Dulay, M. T. Chem. Rev. 1993, 93, 341.(g) Suib, S. L. Chem. Rev. 1993, 93, 803. (h) Krueger, J. S.; Mayer, J. E.; Mallouk, T. E. J. Am. Chem. Soc. 1988, 110, 8232. (i) Persaud, L.; Bard, A. J.; Campion, A.; Fox, M. A.; Mallouk, T. E.; Webber, S. E.; White, J. M. J. Am. Chem. Soc. 1987, 109, 7309. (j) Lin, L.; Al-Thabaiti, S.; Kuntz, R. R. J. Photochem. Photobiol. A: Chem. 1992, 64, 93. (k) Lin, L.; Kuntz, R.R. Langmuir, 1992, 8, 870. (1) Gratzel, M. Comments Inorg. Chem. 1991, 12, 93. (m) Mallouk, T. E. *Nature*, **1991**, 353, 699. (n) Wu, Y.; Li, Y.; Zhuang, Q. J. Photochem. Photobiol. A: Chem. 1991, 62, 261. (o) Horvath, O.; Fendler, J. H. J. Phys. Chem. 1992, 96, 9591.
- 4. Christou, G. Acc. Chem. Res. 1989, 22, 238.

- 5. (a) Lehn, J.-M. In Photochemical Conversion Storage of Solar Energy, Connolly, J. S. Ed.; Academic Press: New York, 1981, Chapter 6.(b) Young, R. C.; Meyer, T. J.; Whitten, D. G.; J. Am. Chem. Soc. 1975, 97, 4781.(c) Bock, C.R.; Meyer, T. J.; Whitten, D. G.; J. Am. Chem. Soc. 1974, 96, 4710.
- 6. Palmans, R.; Frank, A. J.; Houlding, V. H.; Miskowski, V. M. J. Mol. Catal. 1993, 80, 327.
- 7. (a.) Wrighton, M. S.; Ginley, D. S. J. Am. Chem. Soc. 1975, 97, 2065.
- 8. Steigman, A. E.; Miskowski, V. M. J. Am. Chem. SocJ. 1988, 110, 4053.
- 9. (a) Roundhill, D. M. J. Am. Chem. Soc. 1985, 107, 4354. (b) Caspar, J. V.; Gray, H. B. J. Am. Chem. Soc. 1984, 106, 3029
- (a) Gray, H. B.; Maverick, A. W. Science 1981, 214, 1201. (b) Sigal, I. S.; Mann, K. R.; Gray, H. B. J. Am. Chem. Soc. 1980, 102, 7252.(c) Mann, K. R.; DiPierro, M. J.; Gill, T. P. J. Am. Chem. Soc. 1980, 102, 3965. (d) Maverick, A. W.; Gray, H. B. Pure and Appl. Chem. 1980, 52, 2339. (e) Miskowski, V. M.; Sigal, I. S.; Mann, K. R.; Gray, H. B.; Milder, S. J.; Hammond, G. S.; Ryason, P. R. J. Am. Chem. Soc. 1979, 101, 4383. (f) Mann, K. R.; Lewis, N. S.; Miskowski, V. M.; Erwin, D. K.; Hammond, G. S.; Gray, H. B. J. Am. Chem. Soc. 1977, 99, 525. (g) Miskowski, V. M.; Smith, T. P.; Loehr, T. M.; Gray, H. B. J. Am. Chem. Soc. 1985, 107, 7925.
- 11. (a) Vedeneyev, V. I.; Gurvich, L. V.; Kondrat'yev, V. N.; Medvedev, V. A.; Frankevich, Ye. L. "Bond Energies, Ionization Potentials, and Electron Affinities" St. Martin's: New York, 1966. (b) van Koppen, P. A. M.; Bowers, M. T.; Beauchamp, J. L.; Dearden, D. V. In Bonding Energetics in Organometallic Compounds; Marks, T. J.,Ed.; American Chemical Society: Washington D. C.,1990; p 34.

- (a) Che, C.-M.; Lee, W.-M.; Cho, K.-C. J. Am. Chem. Soc. 1988, 110, 5407.
 (b) Harvey, E. L.; Stiegman, A. E.; Vlcek, A., Jr.; Gray, H. B. J. Am. Chem. Soc. 1987, 109, 5233.
- 13. King, R. B. Acc. Chem. Res. 1980, 13, 243.
- 14. Dulebohn, J. I.; Ward, D. L.; Nocera, D. G. J. Am. Chem. Soc. 1990, 112, 2969.
- 15. Dulebohn, J.I. Ph.D. Dissertation, Michigan State University.
- 16. Nixon, J.F. J. Chem. Soc. A 1968, 2689.
- 17. Bennett, M. A.; Patmore, D. J. Inorg. Chem. 1971, 10, 2387.
- 18. Rempel, G. A.; Legzdine, P.; Smith, H.; Wilkenson, G. Inorg. Syntheses, 1972, 13, 90.
- 19. Newsham, M. D. Ph.D. Dissertation, Michigan State University.
- 20. Shin Y.-g. K. Ph. D. Dissertation, Michigan State University.
- 21. Newsham, M.D.; Giannelis, E. P.; Pinnavaia, T. J.; Nocera, D. G. J. Am. Chem. Soc. 1988, 110, 3885.
- 22. TEXSAN TEXRAY Structure Analysis Package, Molecular Structure Corporation, 1985.
- 23. Abrahamson, H. B.; Frazier, C. C.; Ginley, D. S.; Gray, H. B.; Lilienthal, J.; Tyler, D. R.; Wrighton, M. S. *Inorg. Chem.* 1977, 16, 1554.
- 24. Levensen, R. A.; Gray, H. B. J. Am. Chem. Soc. 1975, 97, 6042.
- (a) Miskowski, V. M.; Smith, T. P.; Loehr, T. M.; Gray, H. B. J. Am. Chem. Soc. 1985, 107, 7925.
 (b) Che, C.-M.; Butler, L. G.; Grunthaner, P. C.; Gray, H. B. Inorg. Chem. 1985, 24, 4662.

- 26. Stiegman, A. E.; Miskowski, V. M.; Gray, H. B. J. Am. Chem. Soc. 1986, 108, 2781.
- 27. Shin, Y.-g. K.; Miskowski, V. M.; Nocera, D. G. *Inorg. Chem.* **1990**, 29, 2308.
- 28. Watson, J. T. In *Introduction To Mass Spectrometry*, 2nd Ed., Raven Press: New York, 1985.
- 29. King, R. B.; Chang, M.; Newton, M.G. J. Organomet. Chem. 1985, 296, 15.
- (a.) Jenkins, J. A.; Ennett, J. P.; Cowie, M. Organometallics 1988, 7, 1845.
 (b.) Cotton, F. A.; Eagle, C. T.; Price, A. C. Inorg. Chem. 1988, 27, 4362.
 (c.) Cotton, F. A.; Dunbar, K. R.; Verbruggen, M. G. J. Am. Chem. Soc. 1987, 109, 5498.
 (d.) Balch, A. L.; Oram, D. E.; J. Organomet. Chem. 1988, 349, 245.
 (e.) Cowie, M.; Dickson, R. S. Inorg. Chem. 1981, 20, 2682.
 (f.) Cowie, M. Inorg. Chem. 1979, 18, 286.
- 31. Miskowski, V. M.; Gray, H. B. In *Understanding Molecular Properties*; Avery, J.; Dahl, J. P.; Hansen, A. E., Eds.; Reidel: Dordrecht, 1987; p1.
- 32. Perrault, D.; Drouin, M.; Michel, A.; Harver, P. *Inorg. Chem.* 1992, 31, 2740.
- (a) Balzani, V.; Sabbatini, N.; Scandola F. Chem. Rev. 1986, 86, 319.
 (b) Turro, N. J., "Modern Molecular Photochemistry", The Benjamin Cummings Publishing Company: Menlo Park, CA., 1978; p 158.
- 34. Partigianoni, C. M.; Chang, I.-J.; Nocera, *Coord. Chem. Rev.* 1990, 97, 105.
- 35. Vlcek, A. Jr.; Gray, H. B. J. Am. Chem. Soc. 1987, 109, 286.
- 36. Tolman, C. A. Chem. Rev. 1977, 77, 313.

- 37. Dunbar, K. R. J. Am. Chem. Soc. 1988, 110, 8247.
- 38. (a) Cadogan, J. I. G.; Perkins, M. J. In The Chemistry of Alkenes; Patai, S., Ed.; Interscience Publishers: New York, 1964; p 605. (b) Cais, M. In The Chemistry of Alkenes; Patai, S., Ed.; Interscience Publishers: New York, 1964; p 1009.

Table 2 Atomic Positional and Isotropic Displacement Parameters (Å2) for (1)

Atom	x	у	Z	B/Å ²
Br(1)	0.4995(2)	0.5754(1)	0.2384(2)	2.7(1)
Br(2)	0.3205(2)	0.6729(2)	0.4319(2)	3.2(1)
P(1)	0.6366(5)	0.5686(4)	0.4639(5)	2.0(3)
P(2)	0.6346(5)	0.6027(5)	0.7041(6)	2.1(3)
P(3)	0.4196(5)	0.4968(4)	0.5033(6)	2.2(3)
P(4)	0.3594(5)	0.5747(4)	0.7028(6)	1.8(3)
P(5)	0.5358(5)	0.7458(4)	0.4031(5)	2.1(3)
P(6)	0.4960(6)	0.7921(4)	0.6328(4)	2.0(3)
P(7)	0.4835(6)	0.6905(4)	0.8709(5)	2.4(3)
P(8)	0.2962(6)	0.7714(5)	0.8504(6)	3.3(4)
F(1)	0.712(1)	0.608(1)	0.383(1)	3.2(7)
F(2)	0.649(1)	0.479(1)	0.425(1)	4.0(9)
F(3)	0.713(1)	0.655(1)	0.760(1)	3.8(8)
F(4)	0.648(1)	0.525(1)	0.786(1)	4(1)
F(5)	0.485(1)	0.4195(8)	0.526(2)	6(1)
F(6)	0.365(1)	0.456(1)	0.410(1)	5(1)
F(7)	0.353(1)	0.5251(9)	0.818(1)	2.8(7)
F(8)	0.255(1)	0.6063(9)	0.709(1)	3.0(7)
F(9)	0.638(1)	0.758(1)	0.350(1)	4.2(9)
F(10)	0.482(1)	0.7857(7)	0.301(1)	4.0(8)

MICHIGAN STATE UNIV. LIBRARIES
31293010298838